ELECTRONIC STRUCTURE AND DYNAMICS IN COLLOIDAL GRAPHENE QUANTUM DOTS

By

Cheng Sun

A DISSERTATION

Submitted to
Michigan State University
in partial fulfillment of the requirements
for the degree of

Physics - Doctor of Philosophy

2016

ABSTRACT

ELECTRONIC STRUCTURE AND DYNAMICS IN COLLOIDAL GRAPHENE QUANTUM DOTS

By

Cheng Sun

I present studies of excitons in graphene quantum dots (GQDs), a class of electronically quasi-zero-dimensional materials with a two-dimensional sp^2-hybridized carbon lattice. The weak screening associated with such a two-dimensional lattice of light atoms results in strong carrier interactions. Semiconductor quantum dots and low-dimensional carbon based materials have been developed and studied for decades and gradually applied in areas such as photovoltaics. One of the original motivations for our collaborators' synthesis of these particular GQDs is their potential as sensitizers for solar cells, and research on the electronic structure and the exciton behavior of GQDs will help to reveal the potential of this candidate material.

This thesis describes experimental investigations of biexcitons in GQDs. We use transient absorption spectroscopy to determine the biexciton binding energy. We find a value of $\sim$ 140 meV for a certain type of biexciton, which is in rough agreement with the theoretically calculated value. Compared with semiconductor quantum dots, GQDs display stronger biexciton binding, which highlights the importance of excitonic effects in explaining the optical and electronic properties of these systems. While we observe clear signatures of biexcitons, these states are short-lived. We observe biexciton Auger recombination times of $\sim$ 0.3 ps, which is comparable to the time scale of biexciton Auger recombination in single-wall carbon nanotubes with circumference comparable to the longest edge length of the GQDs studied here. Slower relaxation (a few ps and tens of ps) of excitons is believed

to be related to cooling of the lattice. The strong interaction between carriers and rapid biexciton Auger recombination suggest that GQDs could be used for carrier multiplication and thus increase the efficiency of GQD-based solar cells.

TABLE OF CONTENTS

LIST OF TABLES

LIST OF FIGURES

Chapter 1

Introduction and background

Carbon is one of the key elements in the universe. Because of the flexibility of its bonding, carbon-based systems present a variety of chemical structures with different physical properties. Among the richest carbon-based systems, graphene consists of a single planar sheet of sp^2-bonded carbon. Graphene has played an important role in helping us better understand the electronic properties of other carbon-based materials. These materials include graphite (a three dimensional allotrope of carbon consisting of graphene layers), carbon nanotubes (structures formed by rolling graphene into a cylinder), spherical fullerenes (introduction of pentagons into the graphene lattice), and graphene quantum dots (single-atom-thick sheets of graphene with all dimensions typically less than 100 nm, where electronic transport is confined in all three spatial dimensions [17]). P.R.Wallace theoretically analyzed graphene as early as 1947 [18]. Over the last 50 years, there have been many studies related to single-layer graphite [19, 20, 21], but no one could find an easy and efficient way to produce graphene until Andre Geim and Kostya Novoselov discovered in 2004 that they could exfoliate it from bulk graphene [22, 23]. This enabled the pioneering experiments for which they were awarded the Nobel Prize in Physics in 2010.

Graphene has attracted vast research interest due to its remarkable properties such as large specific surface area, high electron mobility, good mechanical strength, and high thermal conductivity. The linear dispersion of its conduction and valence bands at low-energy have also drawn much attention. Moreover, carbon is abundant and nontoxic compared to some

other solar-cell materials such as heavy-metal based nanocrystals. This makes graphene materials attractive candidates for applications in photovoltaic as, for example, transparent electrodes [24, 25, 26].

1.1 Dissertation outline

This thesis presents experiments performed on optically excited multiple-electron-hole-pair states in graphene quantum dots (GQDs). GQDs are synthesized by our collaborators Liang-shi Li's group at Indiana University [8]. All experimental result presented in this thesis is performed in our lab.

The outline is as follows:

Chapter 1: An overview of the basic concepts and background for understanding the experimental results presented in Chapters 3-5.

Chapter 2: Equipment and methods employed in the experiments and data analysis.

Chapter 3: An experimental study of biexciton binding in GQDs.

Chapter 4: Transient absorption (TA) measurements of the relaxation of biexcitons in GQDs.

Chapter 5: Conclusions and discussion of open problems.

1.2 Carbon, graphite and graphene

As already described, carbon exists in different forms. There are numerous allotropes of carbon including diamond, graphite, carbon nanotubes and graphene. The physical and electronic properties vary greatly among different forms of carbon because of the different ways in which carbon atoms bond with each other. The orbital occupation of the carbon

atom is $1s^2 2s^2 2p^2$. The $2s$ and $2p$ orbitals can easily hybridize with each other in different ways because of their similar energies. This yields the different structures shown in Figure 1.1. Among its many interesting properties, the hardness of diamond is widely known. The electrons of a single carbon atom are arranged in orbitals forming the four corners of a tetrahedron (due to sp^3 hybridization). And all the bonds have the same length with the same bond angle. These covalent bonds give diamond its strength.

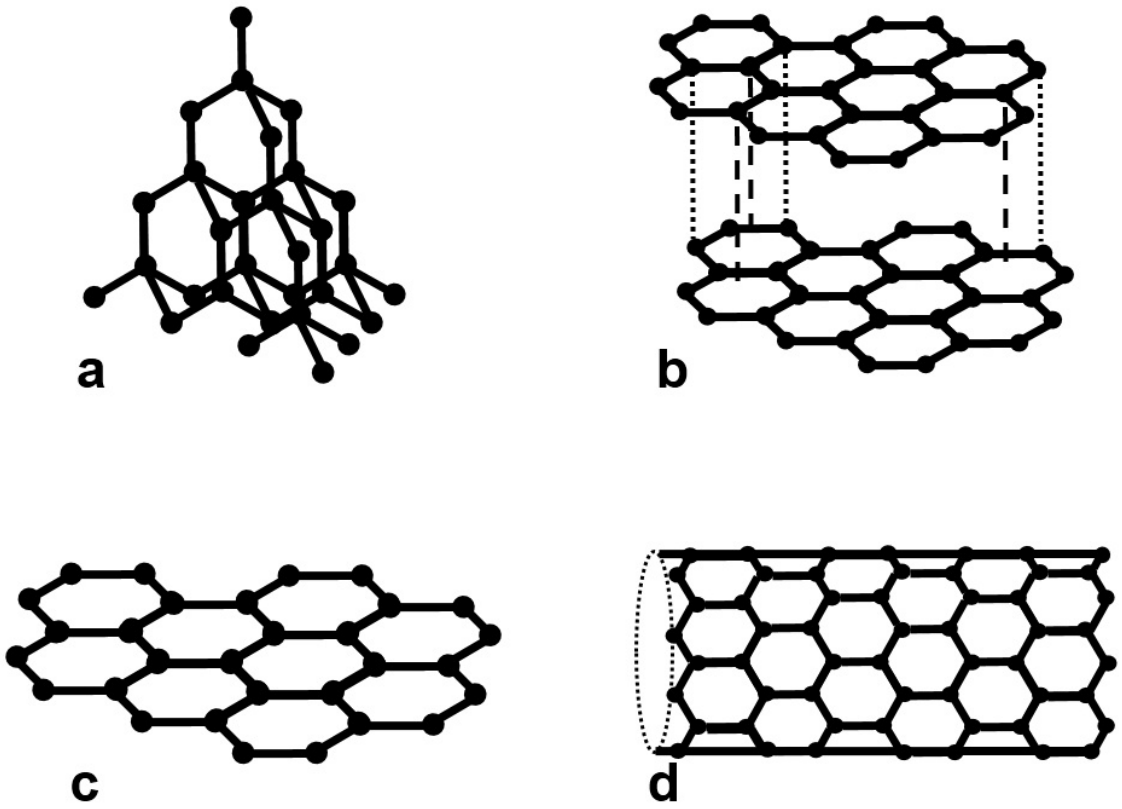

Figure 1.1: (a) Diamond lattice. (b) Graphite lattice. (c) Graphene lattice. (d) Single wall carbon nanotubes.

Unlike diamond, graphite is sp^2-hybridized and has quite different physical and electronic properties. Graphite was named by Abraham Gottlob Werner in 1789 for its use in pencils.

Graphite is structured by stacking multiple single-atom-thick planar carbon sheets, which are held together by van der Waals force. It is an electrical conductor and the most stable form of carbon under standard conditions.

Graphene is another carbon allotrope first discussed theoretically by P.R.Wallace as early as 1947 [18], but due to the difficulty of isolating a single layer of graphene from graphite, no transport measurements were conducted on graphene until 2005 by Andre Geim and Kostya Novoselov [23]. They used adhesive tape to peel the monolayers away, and this process made the production of graphene for laboratory studies much easier. Graphene can be produced through many methods including mechanical exfoliation of graphite [22], chemical reduction from graphene oxide [27], and chemical vapor deposition on metallic thin films [28, 29]. The valence and conduction bands of graphene meet at the Dirac points, leading to zero bandgap. Moreover, the dispersion of graphene is linear so that low-energy carriers can be described in terms of massless Dirac electrons and holes, which travel with a Fermi velocity of 10^6 m/s. This leads to an extremely high charge carrier mobility of 15000 $\mathrm{cm}^2\ \mathrm{V}^{-1}\mathrm{s}^{-1}$ [30].

Carbon nanotubes (CNT) and graphene nanoribbons (GNRs) also attract intention as graphene-related materials. A carbon nanotube is a hollow cylinder consisting of sp^2-hybridized carbon. The first discovery of CNTs can be dated to 1991 by Iijima [31]. CNTs can be prepared by different techniques such as arc discharge [32], laser ablation [33] and chemical vapor deposition [34]. Although current methods of preparation of CNTs always produce impurities, chemical vapor deposition has become a standard method for the CNT production because of its better control over the nanotube length, diameter, orientation and density. After that, single-wall carbon nanotubes (SWCNT) were observed in 1993 [32, 35]. A SWCNT can be visualized as a graphene sheet rolled into a seamless cylindrical tube. A seamless cylinder can only be achieved by rolling in certain directions. The vector connecting

the two carbon atoms that overlap with each other after rolling is called the chiral vector. The chiral vector determines the fundamental optical and electrical properties of SWCNTs, for example, whether the individual nanotube shell is a metal or semiconductor.

A GNR is a strip of graphene with finite width. It was first introduced by Mitsutaka Fujita's group as a theoretical model for nanoscale size effects and edge-shape dependence of GNRs [36]. GNRs keep the outstanding transport properties of graphene [37] but have width-dependent band gaps [38]. Dai's group produced GNRs with width below 10 nm by sonicating a solution of exfoliated graphite [39]. Johnson's group produced GNRs by etching few-layer graphene with thermally activated metallic nanoparticles [40]. GNRs with width below 10 nm were also etched by STM lithography rather than electron beam lithography [41]. However, it is difficult to obtain GNRs with smooth edges and controllable with high yields by these sonochemical, chemical or lithographic methods. Dai's group has introduced a chemical method by "unzipping" CNTs with narrow width distribution (10 - 20 nm) and high yield [42]. More recently, Müllen and collaborators realized GNRs with precise width and edge structures by surface-assisted organic synthesis [43]. Armchair graphene nanoribbons (AGNRs) have been synthesized with different widths such as 5-AGNRs (AGNRs have 5 atoms across their width) [44], 7-AGNRs [43] and even 13-AGNRs [45] by this bottom-up fabrication. Besides surface-assisted organic synthesis, Müllen and collaborators have demonstrated solution-phase synthesis recently of a class of GNRs with long size (>100 nm), narrow width dispersions, well-defined edges, and low optical band gaps (1.2 eV) [46, 47].

1.3 Electronic structure of the graphene lattice

Graphene is a single layer of joined hexagonal rings of carbon atoms. Figure 1.2 demonstrates that carbon atoms A and B are not equivalent. Therefore, graphene is treated as a triangular lattice with a basis of two atoms.

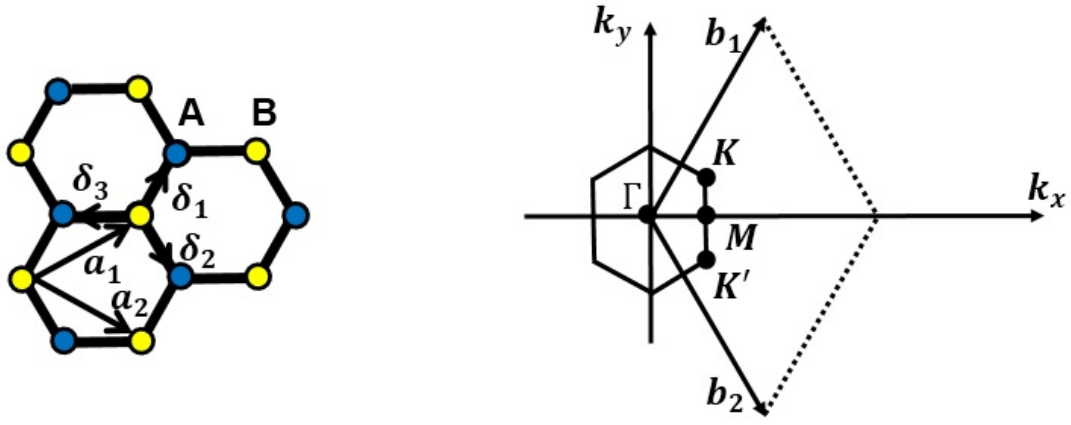

Figure 1.2: (Left) Real-space structure of graphene. The yellow and blue dots represent the two sublattices of graphene. δ_1, δ_2 and δ_3 are the nearest-neighbor vectors. (Right) Brillouin zone of the graphene lattice (reproduced from Ref. [2]).

The three nearest-neighbor vectors can be represented by

$$\delta_1 = \frac{a}{2}(1, \sqrt{3}), \delta_2 = \frac{a}{2}(1, -\sqrt{3}), \delta_3 = \frac{a}{2}(-1, 0) \tag{1.1}$$

where a (≈ 0.142 nm) is the distance between the nearest neighbors. The reciprocal-lattice vectors are given by the vectors b_1 and b_2 in Figure 1.2

$$b_1 = \frac{2\pi}{3a}(1, \sqrt{3}), b_2 = \frac{2\pi}{3a}(1, -\sqrt{3}) \tag{1.2}$$

The Dirac points are at the K and K' points of the Brillouin zone:

$$K = \frac{2\pi}{3a}(\sqrt{3}, 1), K' = \frac{2\pi}{3a}(\sqrt{3}, -1) \tag{1.3}$$

Following P. R. Wallace [18] and using a tight-binding approach, in which we only consider the nearest-neighbor overlap, a tight-binding Hamiltonian with only nearest-neighbour interactions can be written as

$$H = -t \sum_{i,\sigma} (a^+_{\sigma,i} b_{\sigma,i} + a_{\sigma,i} b^+_{\sigma,i}), \tag{1.4}$$

where $a^+_{\sigma,i}$ and $b^+_{\sigma,i}$ are the creation operators and $a_{\sigma,i}$ and $b_{\sigma,i}$ are the annihilation operators on sublattice A and B, respectively, with spin σ. t (≈ 2.8 eV) is the hopping energy between the nearest neighbors. The energy bands derived from this Hamiltonian are

$$E_{\pm}(k) = \pm t \sqrt{1 + 4\cos^2(\frac{\sqrt{3}}{2} k_y a) + 4\cos(\frac{\sqrt{3}}{2} k_y a)\cos(\frac{3k_x a}{2})} \tag{1.5}$$

where the plus and minus sign refer respectively to the electron and hole branches.

Figure 1.3 shows the band structure of graphene based on the tight-binding approach. Undoped graphene is semimetallic, since the conduction and valence bands touch at the Dirac points. The linear dispersion of graphene at low energies leads to a description in terms of Dirac fermion. This is in dramatic contrast to most crystalline materials, which have parabolic dispersion near the band extrema.

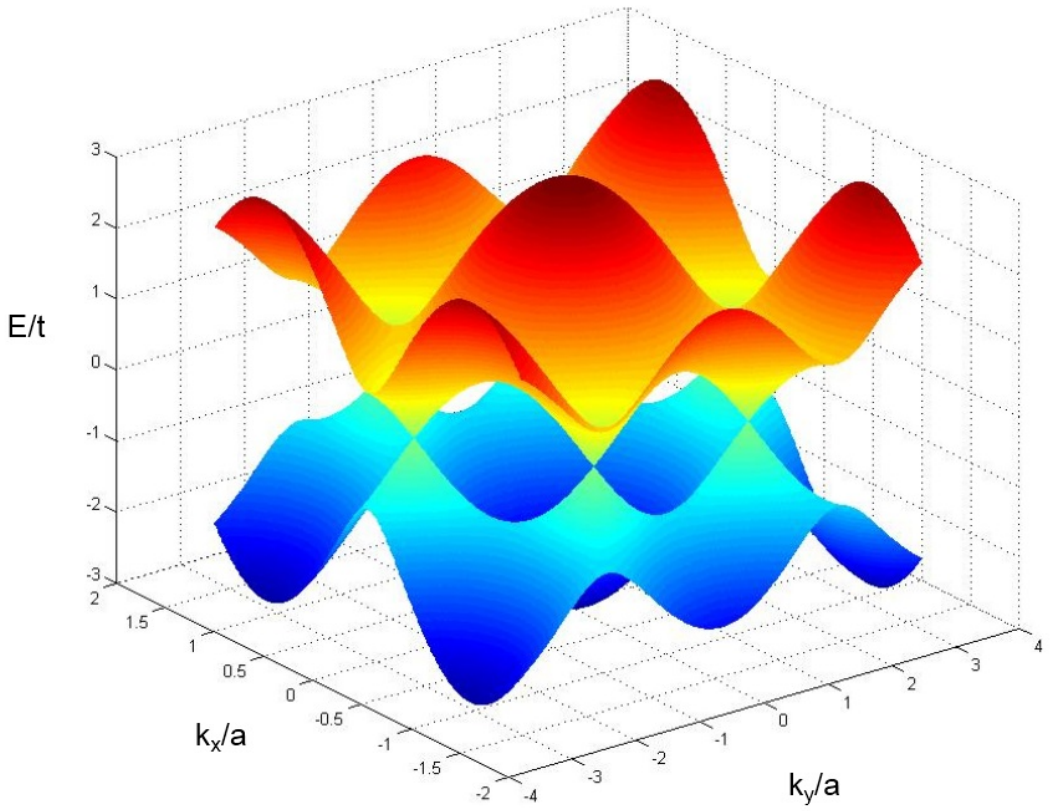

Figure 1.3: Calculated band structure in graphene based on the tight-binding approximation.

1.4 Graphene quantum dots (GQD)

The term quantum dot refers to the confinement of electrons in all three spatial dimensions. The size of a quantum dot can be as small as 10 to 50 atoms, so that they display properties of both atoms/molecules and bulk materials. Usually, graphene quantum dot refers to a single-atom-thick sheet of graphene with dimensions typically less than 100 nm [17]. Quantum confinement can open a size-dependent gap in graphene [8, 10, 17].

To date, many efforts have been made to synthesize GQDs. These efforts can be classified into two groups: top-down and bottom-up methods. In top-down, GQDs are derived from larger carbon materials and include, but are not limited to, electron beam lithography [17], acidic exfoliation [48, 49], and electrochemical oxidation [50]. In contrast, bottom-up methods start from smaller organic precursors [51].

The Top-down methods for the preparation of GQDs take advantage of abundant raw materials, large-scale production, and simplicity. However, this method does have some disadvantages, such as low yield, uncontrollable edge type, and broad distribution of GQD sizes [52, 53]. In contrast, the bottom-up methods offer greater opportunities to control the GQDs with well-defined molecular size, shape, and edges [51].

There are different ways to characterize GQDs. One of them is NMR spectroscopy, which is often used in characterizing molecules. The size of the graphene core and dynamic aggregation in solution on the NMR time scale makes it difficult to characterize GQDs using conventional liquid-phase NMR spectroscopy. Our collaborators were not able to detect any aromatic proton resonance peaks with this method [51]. Precise characterization of GQDs remains a challenge. Another technique that has been used to determine the mass of proteins and polymers is MALDI-TOF (matrix-assisted laser desorption ionization time-

of-flight) mass spectrometry [54]. People use MALDI-TOF to characterize the synthesized GQDs [51]. However, MALDI-TOF cannot provide information on the fraction of different species produced by the synthesis. Precise characterization of GQDs remains a challenge.

The fact that GQDs has been synthesized well recently makes it possible to study GQDs experimentally. The result of quantum confinement is a size-dependent band gap, which results in size-dependent optical and spectroscopic properties [55]. There has been a lot of work done on structures similar to GQDs, e.g., graphene oxide (GO). The energy gap between the highest occupied molecular orbital (HOMO) and the lowest unoccupied molecular orbital (LUMO) of GO has been calculated by Eda et al. by DFT calculation as illustrated in the left panel of Figure 1.4 [3]. GO has a mixture of sp^2- and sp^3-hybridized carbon while GQD consists only of sp^2-hybridized carbon. According to Robertson et al.'s work, the optical and electronic properties of materials with such structures are determined by the π states of sp^2-hybridized carbon [56]. The DFT calculation shown in the left panel of Figure 1.4 illustrate that as the number of fused aromatic rings gets smaller, the energy gap of GOs rises faster.

The band gap of graphene quantum dots with different sizes has also been studied by tight-binding calculations [4]. As illustrated in the right panel of Figure 1.4, the calculated energy gap for a hexagonal GQD with armchair edges is proportional to $1/\sqrt{N}$ or $1/L$ from hundred to million atom nanostructures, where N is the number of hexagonal units along an edge and L represents the size of the quantum dot.

Besides size, the edge structure also plays an important role in the properties of quantum dots, which can also be seen in from Figure 1.4: the size-dependence of the bandgap of GQDs with zigzag edges and armchair edges are quite different. The bandgap of the zigzag GQDs decays to zero much faster than that of armchair GQDs as the size of the GQD increases.

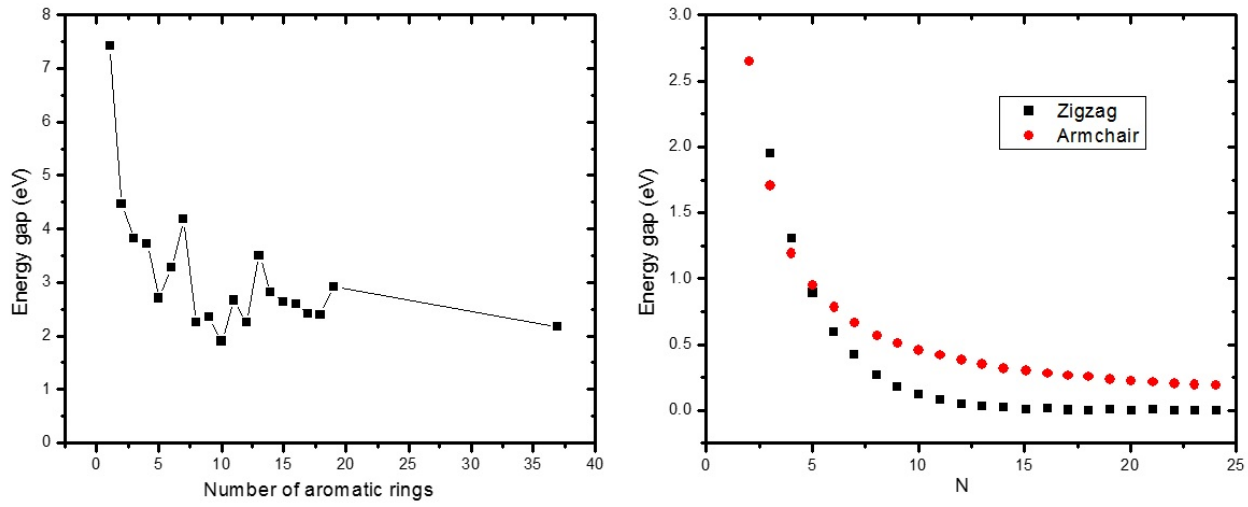

Figure 1.4: (Left)Band gap of π-$\pi*$ transitions on chemically derived GO calculated by DFT as a function of the number of aromatic rings. Reproduced from Ref. [3]. (Right) Size-dependence of the band gap of GQDs with zigzag and armchair edges (N is the number of hexagonal units along an edge). Reproduced from Ref. [4].

As illustrated in Figure 1.2, the graphene lattice has two sublattices denoted as A and B. In the middle of a graphene sheet, 3 carbon atoms from sublattice A and 3 carbon atoms from sublattice B form a fully benzenoid ring. Because of the symmetric structure, there are no localized double bonds in the ring. On the edges of the graphene segment, though, there might be nonbonding states depending on the edge type. Two limiting motifs for the edge structure of graphene are zigzag and armchair, as illustrated in Figure 1.5. Armchair edges consist of pairs of A and B atoms, while zigzag edges are terminated by either A or B sublattices. With armchair edges, all the π-bonds can be satisfied simultaneously with edge states consisting of standing waves [5]. With zigzag edges, the symmetry of the pseudospin is broken at the zigzag edge. Thus, armchair edges maintain pseudospin symmetry and are nonmagnetic, while zigzag edges support localized, spin-polarized edge states. The edge-state spin plays a significant part in the magnetism of a graphene segment [57, 58]. As shown

in Figure 1.6, hexagonal GQDs with zigzag edges and armchair edges have different energy states and band structures. Moreover, a triangular GQD with zigzag edge structure shows a shell of degenerate levels at the Fermi level resulting in zero-energy states [59]. Carriers can be optically excited from the valence band to the zero-energy states or from the zero-energy states to the conduction band. With the development of bottom-up synthesis [43], people can now precisely control graphene nanoribbons and graphene quantum dots, which also proceed the experimental study of these material.

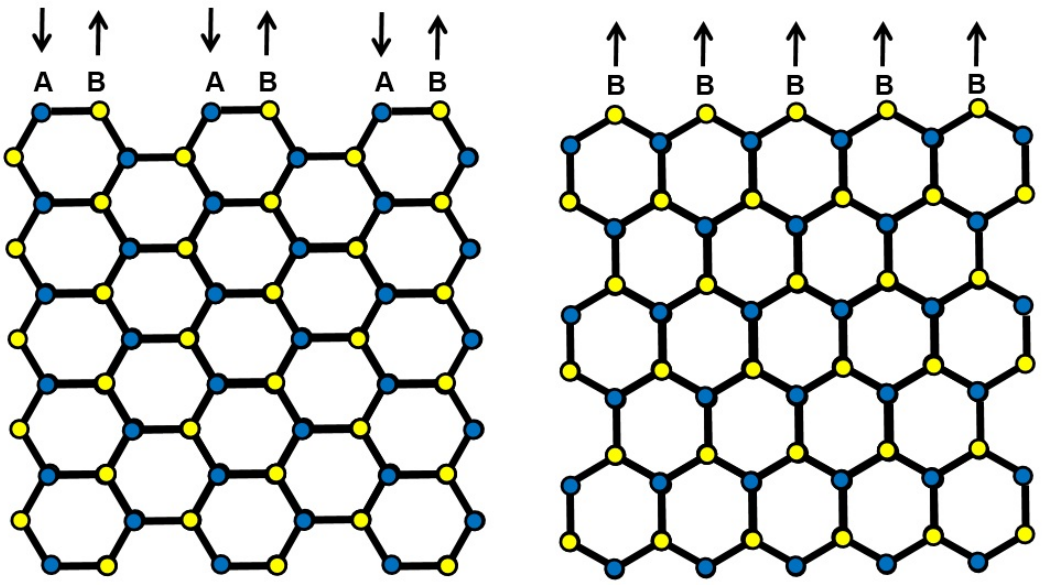

Figure 1.5: Illustrations of the sublattice symmetry of armchair (left) and zigzag edges (right). The up- and down-arrows represent spins. Reproduced from Ref. [5].

Poor solubility and one-atom thickness can result in aggregation of GQDs. It can happen as specific head-to-tail molecular arrangements (J-type aggregation [60]) for zigzag edge GQDs or as a piling up as for discs. Aggregation can limit the potential applications of GQDs. Chen et al. observed J-type aggregation by TEM [60], and the high concentration

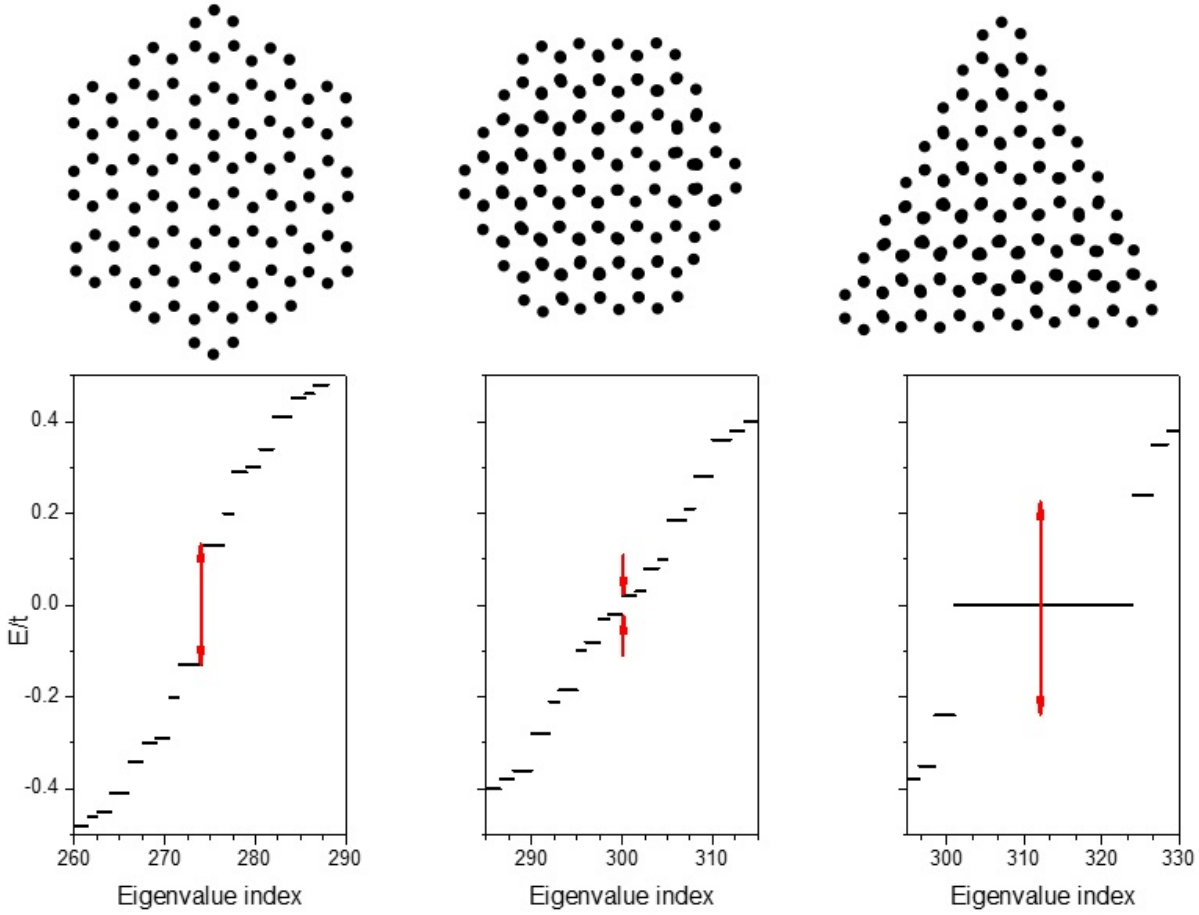

Figure 1.6: Tight-binding spectra of (a) armchair hexagonal, (b) zigzag hexagonal, and (c) zigzag triangular GQDs. Reproduced from Ref. [6].

of GQDs resulted in a shift of the emission peak to lower energy. To prevent aggregation, people have attached ligands to the edges of GQDs. Kastler et al. performed a detailed experimental comparison of the effects of different attached ligands and different solvents on the electronic and optical properties of three hexa-peri-hexabenzocoronenes (HBC) [61]. Yan et al. attached multiple 1,3,5-trialkyl-substituted phenyl moieties to the edge of GQDs. These ligands acted like a cage so that aggregation among GQDs was suppressed. This structure also increased GQD solubility in organic solvents like toluene [51].

GQDs also show great promise in solar cell and photovoltaic applications because of

their size-tunable optical response. The injection time of electrons and holes in perovskite solar cells based on $CH_3NH_3PbI_3$ was measured to be 0.4 to 0.6 ns, while the hot carrier cooling time was only about 0.4 ps [62]. This indicates that a large amount of transferred energy is wasted because of the fast cooling process. To increase the power conversion efficiency, Zhu et al. inserted an ultrathin GQD layer in a perovskite solar cell [63]; faster electron/hole extraction (90 ps) was observed in TA measurements than the 280 ps extraction time observed in solar cells without the GQD layer. The GQD layer increased the power conversion efficiency from 8.81 % to over 10 %. In another work, Gao et al. proved that GQDs can form a heterojunction with crystalline silicon for highly efficient solar cell applications [7]. There was a large junction gap between n-type Si and GQDs allowed carriers to be efficiently separated. As a result, the crystalline silicon solar cell with GQDs showed a better external quantum efficiency and power conversion efficiency than did a solar cell without GQD layers as illustrated in Figure 1.7. Moreover, such crystalline silicon/GQD solar cells showed good stability as they maintained high efficiency after half a year of storage.

1.5 C132 and C168 GQDs

The GQDs used in our experiments consist of 132 or 168 sp^2-hybridized carbon atoms in the core and are respectively labelled as C132 and C168. As shown in Figure 1.8, C168 has a triangular form and C132 has a trapezoidal form missing a corner compared with C168. These GQDs are synthesized by a solution-chemistry approach developed by our collaborators in the Department of Chemistry at Indiana and based on oxidative condensation reactions developed by Klaus Müllen's group [64]. The solution-phase synthesis of C168 is illustrated in Figure 1.9, where "R" represents 2,4,6-triakyl phenyl groups, which covalently

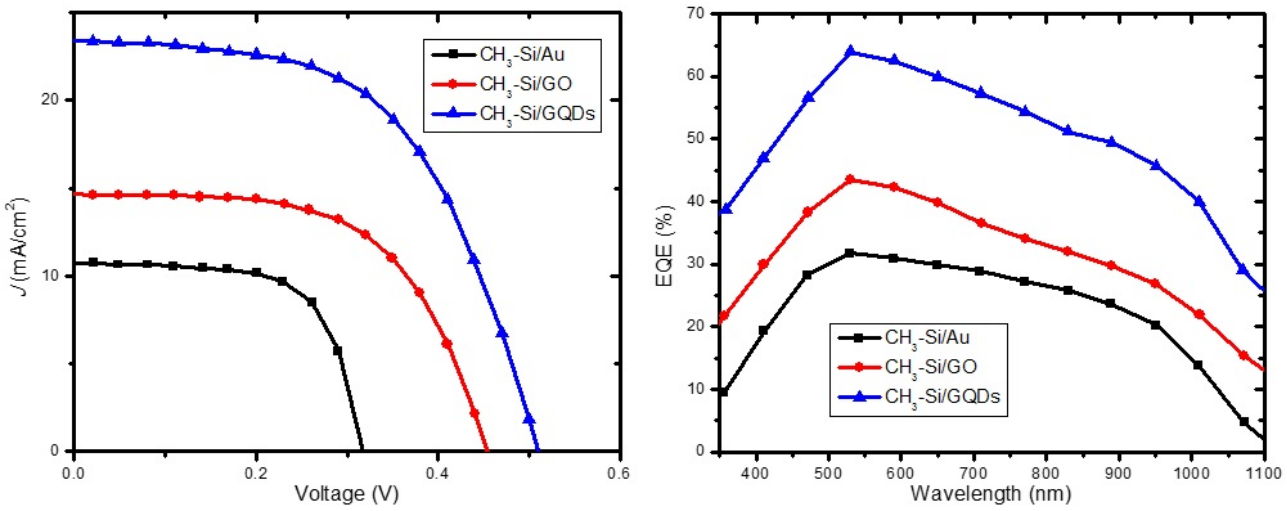

Figure 1.7: Improved power conversion efficiency (left) and external quantum efficiency (right) of solar cell with/without GQD layers. Reproduced from Ref. [7].

attach to the edges of the GQD. These phenyl groups twist to an out-of-plane configuration due to steric constraints thereby caging the GQDs in alkyl groups and reducing the aggregation between GQDs, as well as increasing their solubility.

The longest edge of the GQDs we have studied is about 2.4 nm. The linear dispersion of graphene can be described by $E = \hbar v_f \sqrt{k_x^2 + k_y^2}$, where $v_f = c/300$ and c is the speed of light in vacuum. Rozkhov and Nori have deduced analytic solutions of the Schrodinger equation for an electron in a triangular armchair graphene dot [10]. Their solution yields a confinement energy in C168 of 1.6 eV. The UV/vis (Varian Cary 50 Bio UV-Visible Spectrophotometer) ground-state absorption spectrum of the GQDs dissolved in toluene is illustrated in Figure 1.8. From the measurement, the lowest-energy feature in the absorption spectrum of C168 is at about 1.7 eV.

C132 and C168 were first synthesized by Yan et al. with the goal of developing a sensitizer

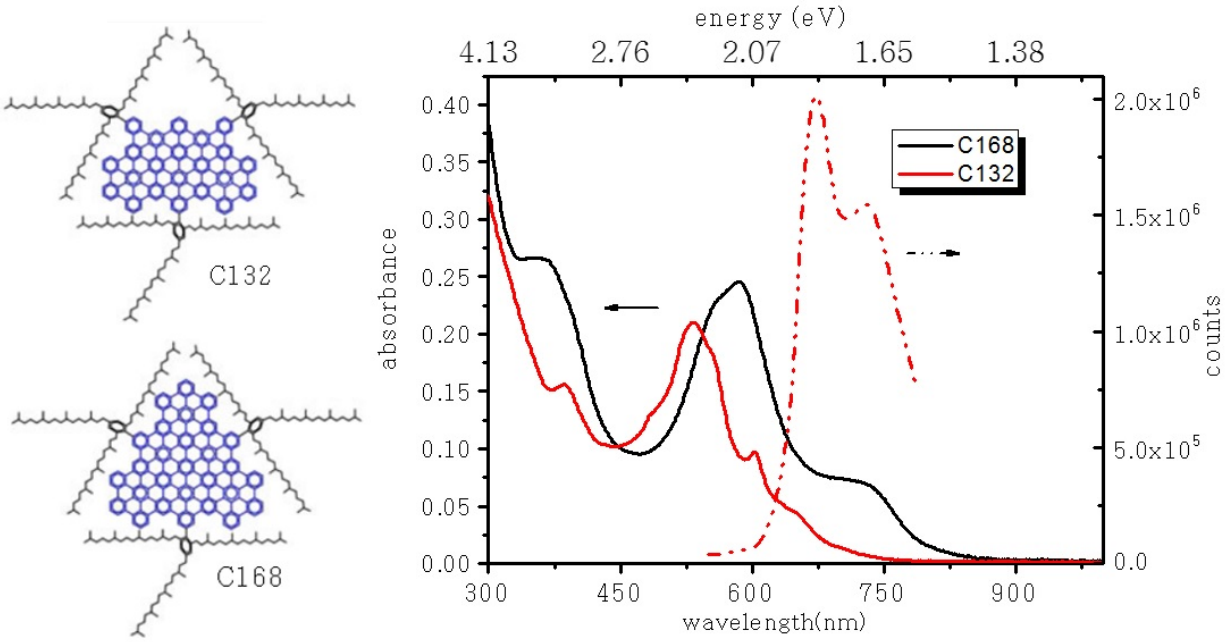

Figure 1.8: (Left) Structure of C132 and C168 GQDs [8]. The blue area is the two-dimensional graphene sheet, and the black structures are ligands to promote solubility and prevent aggregation. (Right) Solid lines: Ground-state absorption spectra of C132 and C168 GQDs. Dashed line: photoluminescence spectrum of C132 excited at 3.1 eV

in organic photovoltaics [51]. William Shockley and Hans Queisser [9] calculated the maximum theoretical efficiency of a solar cell using a single p-n junction. Their result is shown in Figure 1.10. Since the band gap of C168 is 1.7 eV, such GQDs might have potential as sensitizers for high-efficiency solar energy conversion.

One of the areas of interest in these GQDs is carrier interactions, e.g, exciton and biexciton behaviors. Biexcitons are bound states of two excitons. When a biexciton decays radiatively, it typically produces a free exciton and a photon. In transient absorption measurements, an exciton can be formed with the pump photon. After this, a probe photon is absorbed by the system in a single-to-biexciton transition. Therefore, understanding the

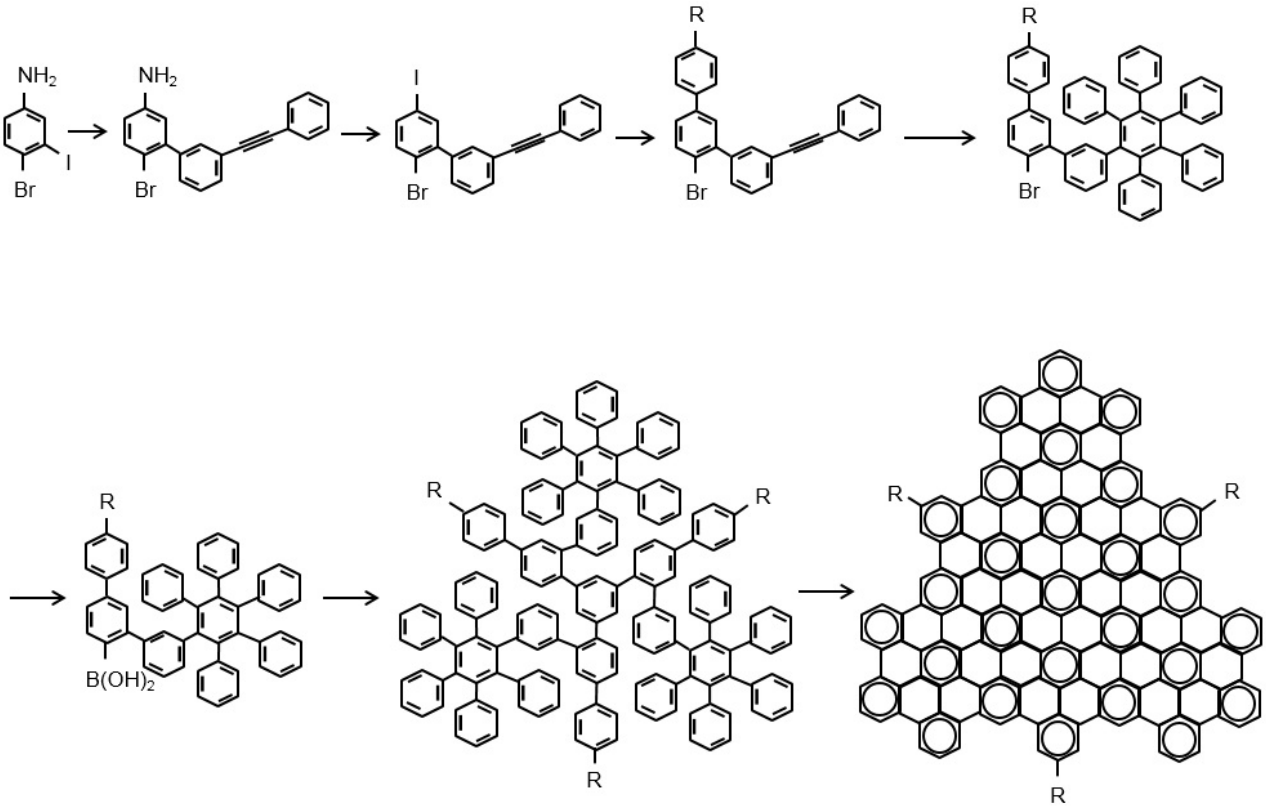

Figure 1.9: Synthesis of C168 GQD. Reproduced from Ref. [8].

formation and decay of biexcitons will help us interpret the dynamics of single excitons and spectroscopic measurements. Biexciton binding will be discussed in Chapter 3, and biexciton Auger recombination (non-radiative recombination of an electron-hole pair in which the energy and momentum is transferred to another carrier) will be discussed in Chapter 4.

A few theoretical and experimental reports on these particular GQDs (C132 and C168) precede our work. Stefan Schumacher used density functional and configuration-interaction-based electronic structure methods to calculate the low-energy electronic structure of C168 [65]. His results indicate that the lowest electronic excitations in the singlet manifold of C168 are optically dark, which helps us better understand the transitions from our experimental absorption spectrum when we interpret our data. Pawel Hawrylak's group calculated the

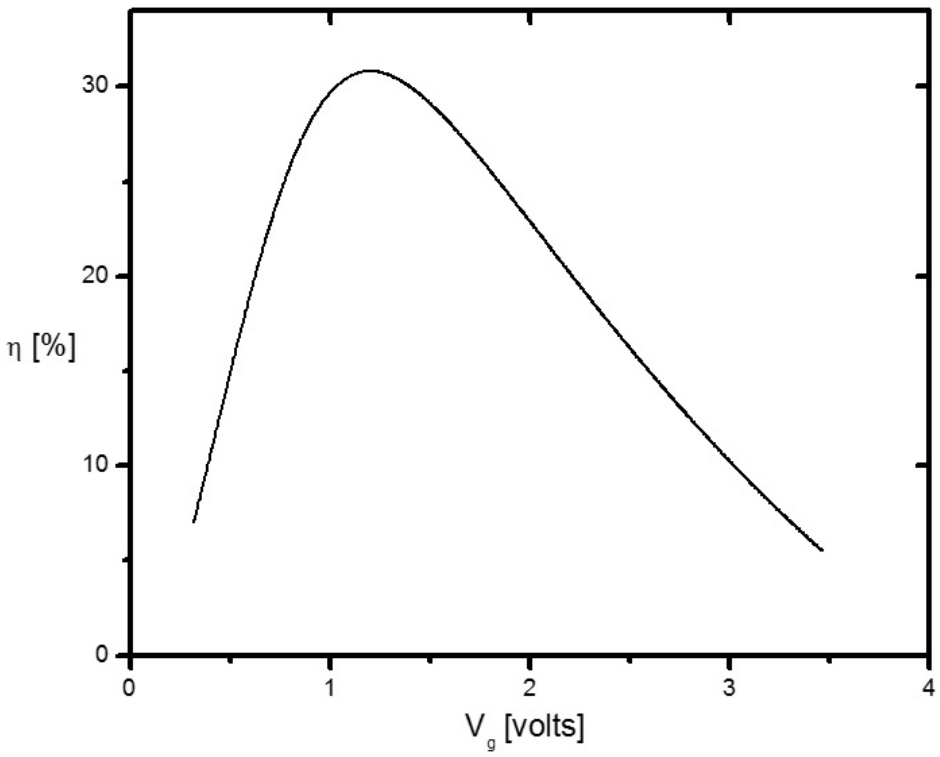

Figure 1.10: Detailed-balance limit of the efficiency of a single p-n junction solar cell calculated as a function of band gap by William Shockley and Hans Queisser [9]. The upper horizontal axis shows the band gap in eV.

electronic structure of these materials based on a tight-binding model combined with Hartree-Fock and configuration-interaction methods [15]. They found out the lowest energy state is dark and the bright excitons of lowest energy is two-fold degenerate, which is much helpful in our data interpretation. The group of Liang-shi Li performed initial studies of what was understood as a long-lived triplet state in C168 [66] and measurements of slow (100 - 300 ps) dynamics in transient absorption that they interpreted in terms of a phonon bottleneck of the GQDs [67], which also motivate further exploration of the relaxation mechanisms in these GQDs.

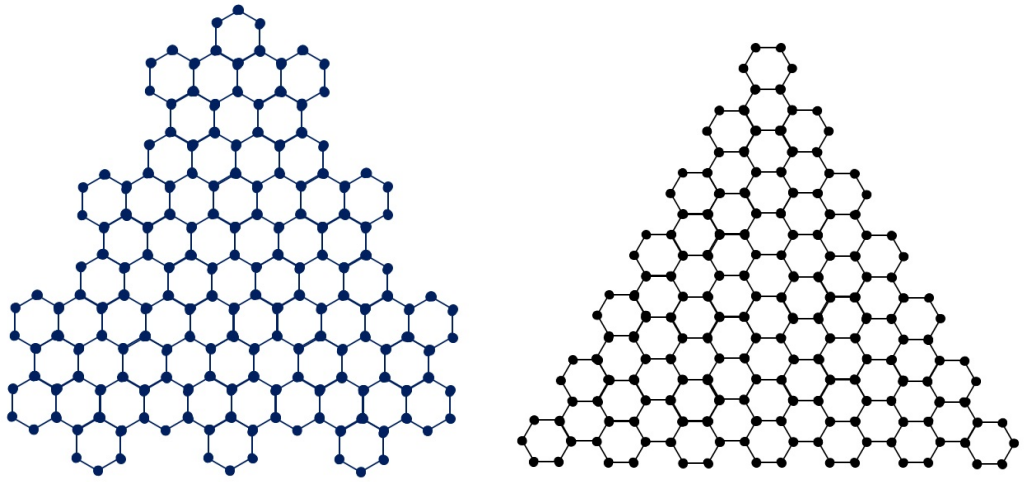

Figure 1.11: (Left) C168 GQD synthesized by Yan and Li [8]. (Right) C168$_{ac}$: GQD with armchair edges [10].

Tight-binding calculations are a good place to start to learn about the electronic structure of GQDs. Rozhkov and Nori [10] performed such calculations on triangular GQDs with armchair edges. Although our GQDs have mixed edge types of armchair and zigzag, the symmetry of an armchair GQD with 168 carbon atoms (C168$_{ac}$) is exactly the same as that of C168 as shown in Figure 1.11. Therefore, we expect that the calculated electronic structure of C168$_{ac}$ should be a good first estimate of the electronic structure of C168.

We can understand the degeneracy of the single-particle states of C168 by considering the allowed wave vectors in C168$_{ac}$. The low-energy electronic structure in C168$_{ac}$ can be determined by quantizing the allowed wave vectors, as shown in Figure 1.12. The symmetry of the triangular graphene lattice reveals that, all available states in the Brillouin zone can be obtained from the states in one sixth of the Brillouin zone by $\pm 2\pi/3$ rotations around the origin or reflections about the lines $k_y = 0$ and $k_y = \pm\sqrt{3}k_x$. The allowed wave vectors consist of linear superpositions of the two eigenvectors $\vec{K_1}$ and $\vec{K_2}$:

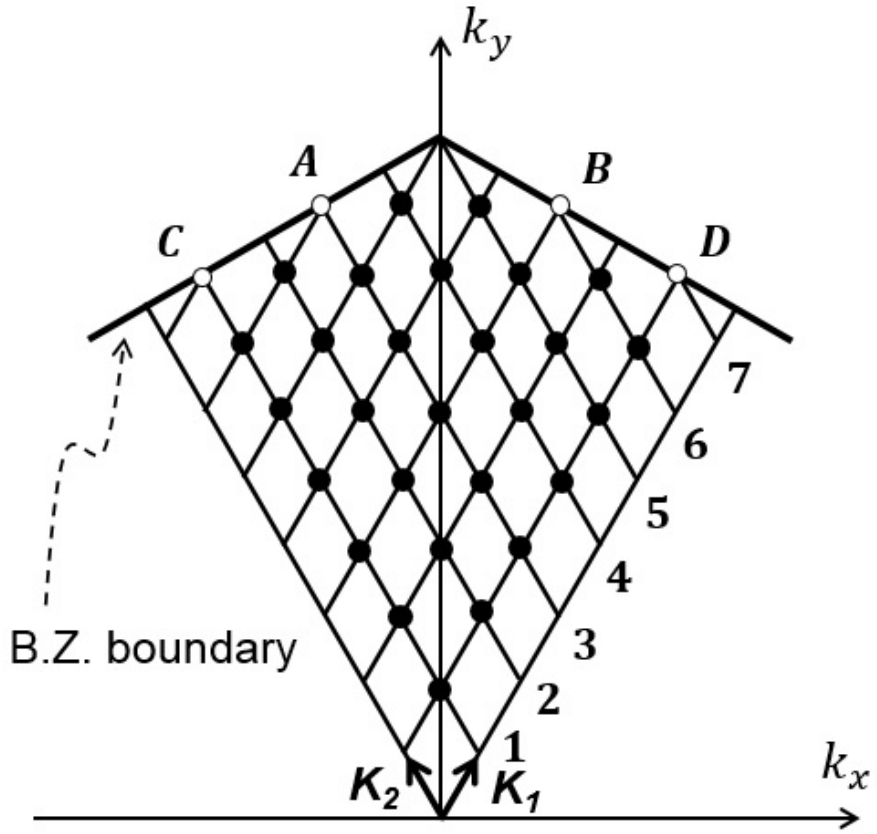

Figure 1.12: The allowed values of $\vec{k}^{n,m}$ of a triangular armchair GQD of 60 C atoms. The allowed $\vec{k}^{n,m}$ occupy one sixth of the graphene Brillouin zone. Every filled circle represents one orbital state (i.e, two states including spin), while each open circle represents a half state [10].

$$\vec{k}^{n,m} = n\vec{K}_1 + m\vec{K}_2. \tag{1.6}$$

For a tight-binding calculation involving only nearest-neighbor hopping, the corresponding eigenenergies are

$$\varepsilon_{n,m\pm} = \pm t \left\{ 3 + 2\cos\Big(\frac{2\pi n}{3N}\Big) + 2\cos\Big(\frac{2\pi m}{3N}\Big) + 2\cos\Big(\frac{2\pi(n+m)}{3N}\Big) \right\}^{1/2} \tag{1.7}$$

where N=8 for C168$_{ac}$ and t is the nearest-neighbour hopping energy. We use t=2.7 eV to estimate the energies of available states in Table 1.1, in which the columns labelled "n" and "m" are the coefficients of the two eigenvectors and the column labelled "Symmetry" lists the Mulliken symbols indicating the symmetry of the irreducible representations to which each state belongs (here, there are only one-dimensional, "A", and two-dimensional, "E", representations).

Table 1.1: Theoretical electron and hole states in C168$_{ac}$

n	m	Eigenenergy/eV	Symmetry	Degeneracy
8	7	0.726	E	2
9	6	1.157	A	1
7	7	1.335	A	1
8	6	1.438	E	2
9	5	1.702	E	2
7	6	2.050	E	2

As there is not a perfect way to characterize the GQDs, we also need to be aware of that the optical response that we measure in our experiments might arise from impurities. Riesen et al. performed theoretical calculations and optical spectroscopy of C132 [11]. The intensity of the two main photoluminescence (PL) peaks of C132 (at ∼670 nm and ∼750 nm) is strongly dependent on the excitation wavelength as shown in Figure 1.13. That the

excitation-wavelength dependence is different for the two peaks is strong evidence for the presence of different chemical species in the sample. Under the assumption that the PL peak at ∼670 nm may be caused by impurities, they also performed photobleaching experiments to explore the origin of the two PL features. By comparing the measured fluorescence of C132 in heptane before and after bleaching in dichloromethane, they concluded that the 670 nm emission bleaches at a different rate than the ∼750 nm emission, which confirms that the ∼670 nm PL peak is generated by an impurity.

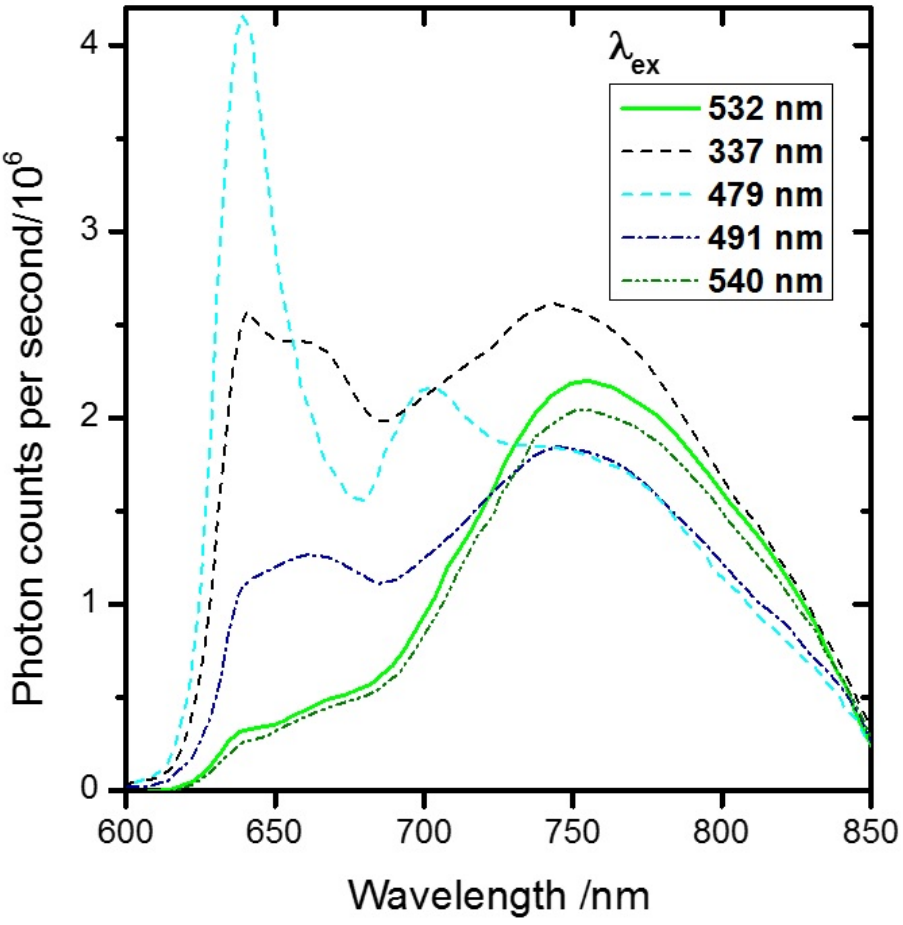

Figure 1.13: Fluorescence spectra for various excitation wavelengths λ_{ex} of C132 in toluene. (reproduced from Ref. [11])

1.6 Exciton confinement

Excitons, bound state of an electron and a hole, were first proposed as quasiparticles by Yakov Frenkel in 1931 [68]. An exciton is a hydrogen-like quasiparticle with neutral charge. Because of the small effective masses of band-edge carriers and the large index of refraction of most semiconductors, an exciton is much more weakly bound and correspondingly larger than the electron and proton of a hydrogen atom. An exciton can be generated by photon absorption in a semiconductor. In most bulk semiconductors, the energy difference between bound and unbound electron and hole (the binding energy) is usually small so that the thermal energy at room temperature exceeds typical exciton binding energies of bulk crystals. Therefore, at room temperature, excitonic effects in bulk materials often can be neglected.

Many of the differences between bulk and reduced-dimensional systems are due to the dimensionality-dependence of the density of states (DOS). In a two-dimensional system, an electron is constrained to move in a plane, and in a one-dimensional system like carbon nanotubes, an electron can move only along the axis of the tube. Figure 1.14 (reproduced from Ref. [12]) shows the ideal density of states $N(E)$ for systems of different dimensionality. The density of states scales with energy as $N(E) \propto E^{1/2}$ in three dimensions, and it changes to $N(E) \propto E^0$ in two dimensions, which results in a step-like shape as shown in Figure 1.14.

In two-dimensional systems, the energy of the transitions between quantized energy levels can be estimated by tight-binding calculations [69] as follows:

$$E_n = E_g - \frac{E_b}{(n+\frac{1}{2})^2}, n = 0, 1, 2... \tag{1.8}$$

where E_g is the bandgap energy of the bulk and E_b is the binding energy of the bulk.

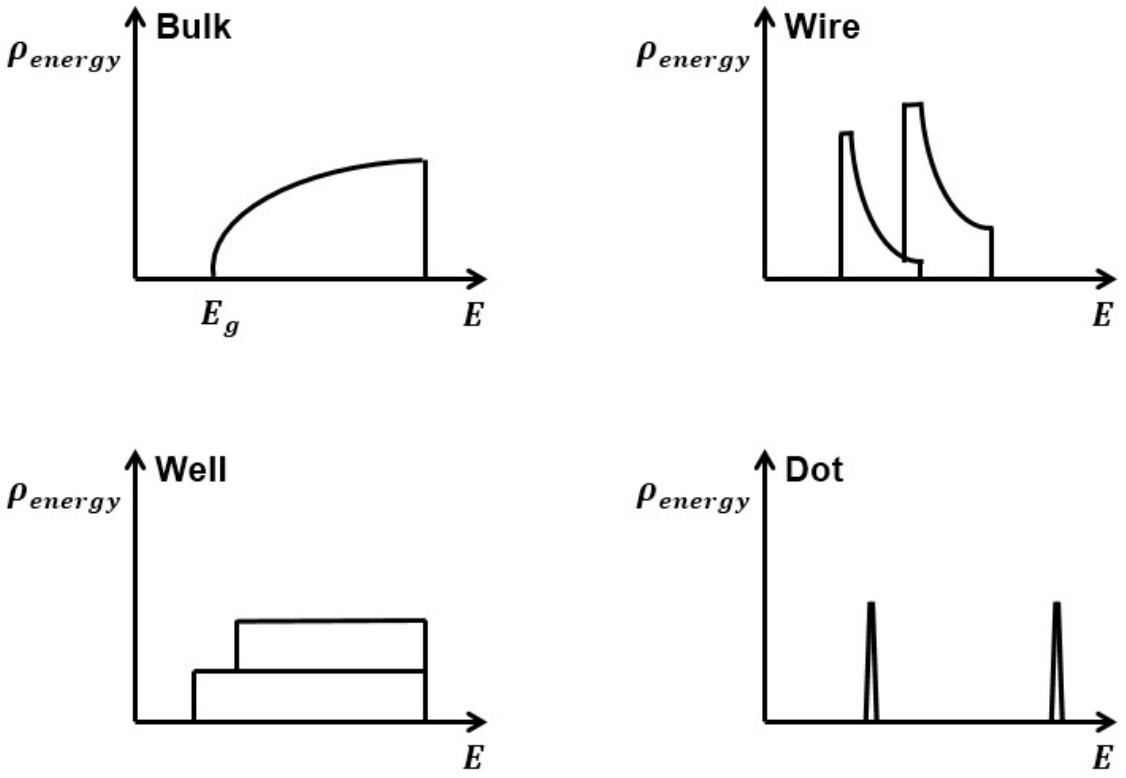

Figure 1.14: Summary of the density of states for a bulk crystal (3D), a quantum well (2D), a quantum wire (1D), and a quantum dot (0D) (reproduced from Ref. [12]).

Besides the effects from the density of states, the Coulomb force is inversely proportional to the dielectric constant ε. In reduced-dimensional systems, many of the electric field lines between electrons and holes are outside of the system. The effective dielectric constant is then determined largely by the environment [70, 71], not the system itself, resulting in weaker dielectric screening and a smaller dielectric constant. Therefore, the binding energy may be more pronounced in a reduced-dimensional system, which has been verified in experiments on SWCNTs. For example, semiconducting SWCNTs of 0.8 nm diameter have an effective exciton radius of 1.2 nm and binding energy of about 400 meV [72].

Many reduced-dimensional systems (e.g., SWCNT and semiconductor quantum dots)

have been well studied over the past few years [73, 74, 75, 76]. The sp^2-hybridized carbon in graphene has two inequivalent energy bands near K and K' of the Brillouin zone (Figure 1.2). The one-dimensional nature of SWCNTs enhances the excitonic effects. Both theoretical calculation and experimental measurements show that the binding energy in SWCNTs is large and can be similar to the band gap [72, 77, 78, 79, 80].

1.7 Biexciton binding and Auger recombination

1.7.1 Introduction to biexciton binding

When there are multiple excitons in a system, an exciton can bind with another exciton to form a biexciton (XX). The binding energy of a biexciton is the energy difference between biexcition energy and the sum of the energies of the otherwise free single excitons that bind to form the biexciton $\Delta E_{\mathrm{XX}} = 2E_{\mathrm{X}} - E_{\mathrm{XX}}$. Figure 1.15 shows the exciton and biexciton dispersion in the case of positive biexcition binding energy, which applies to our system. ΔE_{XX} can be ~ 0 for weakly bound biexcitons [73, 81] or negative for biexciton repulsion [82].

If a biexciton is weakly bound, a lower driving force is required to unbind the biexciton. Much research has been focused on increasing the number of carriers to get more efficient nanocrystal solar cells [13, 83, 84]. In photovoltaic research, people are interested in biexciton studies that might lead to potential applications if there is an efficient way to generate, separate, and transport carriers in these materials.

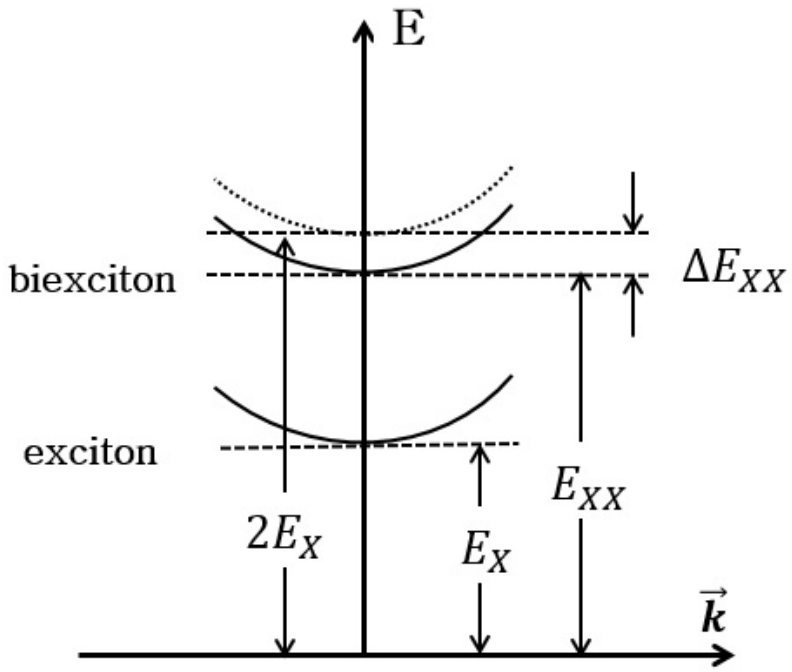

Figure 1.15: Illustration of exciton and biexcition dispersion for positive biexciton binding energy

1.7.2 Introduction to Auger recombination

Auger recombination is a non-radiative process in which one electron-hole pair recombine by transferring their energy and momentum to another electron or hole. Auger recombination usually happens rapidly (a few ps [75, 85]) in nanometer scale particles as the carrier interactions are enhanced and momentum conservation constraints relaxed [86]. The inverse process can also occur. A semiconductor can absorb a high-energy photon, creating a high-energy exciton from which multiple excitons can be created by transferring energy and momentum among carriers. This process is called multiple exciton generation (MEG) or carrier multiplication (CM). A schematic energy level diagram showing Auger recombination

and carrier multiplication is illustrated in Figure 1.16 [13, 87, 88].

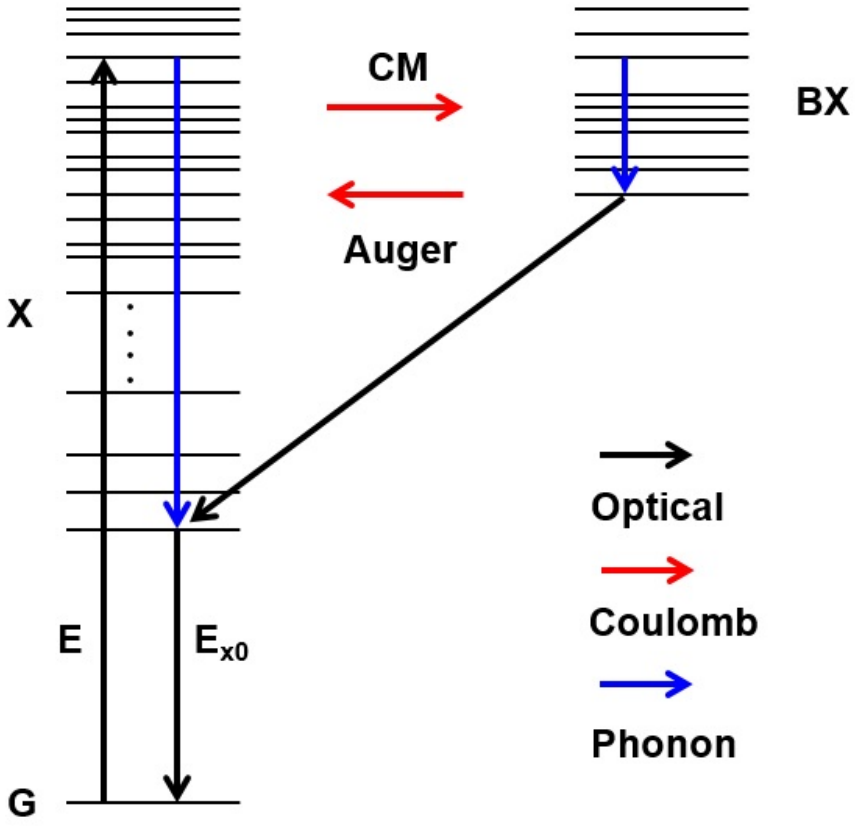

Figure 1.16: Energy-level diagram illustrating carrier multiplication and Auger recombination (reproduced from Ref. [13]).

Chapter 2

Equipment and methods for the study of GQDs

We use different time-resolved spectroscopy methods to investigate excitons in GQDs. Transient absorption (TA) is the primary technique in the study of GQDs discussed in this dissertation. The set up of the TA experiment is explained in this chapter as are some the details of the TA experiment, such as how to determine key parameters. Besides the TA measurement, we also used upconversion of photoluminescence (uPL) to explore exciton dynamics in the GQDs. The result of these measurements will be presented in later chapters where the experimental data is analyzed.

2.1 Comparison of measurement techniques

Time-resolved absorption and emission are often used for exploring the dynamics of chemical and biological systems in the picosecond and femtosecond time domains [89]. In a transient absorption measurement, an initial pulse, the "pump" excites the sample. Another time delayed pulse, the "probe", measures the absorption of the sample. The pump excites some of the electrons, and state-filling reduces the probability of obsorbing a probe photon. In our experiment, transient absorption is a convenient technique which provides us with detailed information about different transitions.

As for time-resolved emission methods, there are many different techniques, such as single-photon counting (TCSPC), upconversion, streak camera, and Kerr gating, which are suitable for different situations. TSCPC is a great method with 20-30 ps instrumental resolution when the signal is coupled with a stable, high repetition rate laser [90]. When coupled to a spectrograph with two-dimensional detection, streak cameras provide multichannel detection with 2-10 ps resolution [91, 92, 93]. We are often focused on dynamics in the few hundred fs range which requires better time resolution than TCSPC and streak camera can provide. Both upconversion and Kerr gating can provide sub-picosecond resolution. We performed both Kerr gating and upconversion. However, the Kerr gating method has a large background signal from long-lived emission making it hard to get decent signal-noise ratio in the experiment. We eventually chose upconversion to perform time-resolved emission measurements in our study.

2.2 Transient absorption measurement

Transient absorption spectroscopy can be used to study many processes like photoinduced chemical reactions, the behaviour of electrons that are freed from a molecule or crystalline material, and the transfer of excitation energy between molecules [94]. The change in absorbance of a sample at a particular wavelength or range of wavelengths is measured as a function of time after the system is excited by the pump. In a typical experiment, both the light for initial excitation (pump) and the light for measuring the absorbance (probe) are generated by a pulsed laser.

Our TA measurements are performed by exciting the samples with either high-energy photons (3.1 eV photons generated by doubling the output of an amplified 1 kHz Ti:sapphire

laser (Spectra-Physics Spitfire PRO-XP) producing $\sim$ 100 fs pulses) or lower-energy photons that are generated by doubling the output signal pulses of a custom built, beta barium borate (BBO)-based optical parametric amplifier (OPA) producing tunable signal from 0.78 to 1.05 eV. The probe pulses consist of a supercontinuum generated by focusing $\sim$ 1 μJ of the 800 nm fundamental in a 1-mm-long c-cut sapphire crystal. The combination of a half-wave plate and thin film polarizer (TFP) before the sapphire crystal allows fine tuning of the beam power focused in the sapphire crystal for optimizing the stability of the white light continuum (WL). The continuum is partially compressed with a pair of Brewster-angle fused-silica prisms. The angle between the colinearly polarized pump and probe is $\sim 7.5^\circ$. Broadband detection is performed with a charge-coupled-device (CCD) spectrometer (Ocean Optics USB2000+, 600 lines/mm grating, 50 μm entrance slit, 2 nm resolution) synchronized to an optical chopper (New Focus 3501) that modulates the pump pulses on and off with a 12 ms period. For single-wavelength dynamic traces and measurements where the spectrometer is insensitive, detection is performed with an amplified Si or InGaAs photodiode at the output of a spectrometer (Acton SP300i, typical resolution $\sim$ 5 nm) and gated by a boxcar integrator (Stanford Research Systems SR250). The frequency of the optical shopper is set to half the repetition rate of the laser so that every other pump pulse excites our sample.

2.2.1 OPA-derived pump

In transient absorption experiments, we need to be able to vary the pump photon energy. For this we built an optical parametric amplifier. Here we choose type-II phase matching (signal and idler orthogonally polarized) in our OPA so that we can select signal (the short wavelength) or idler (the long wavelength) simply with a polarizer. In our OPA, we use a supercontinuum as the seed for parametric amplification in the first pass through the BBO

crystal. After that, the amplified signal from the first pass is reflected back through the same BBO crystal at a slightly different angle and amplified by another 800 nm beam. In most cases, we need tunable visible light, so we pass the infrared beam through another BBO crystal to generate the second harmonic of the signal or idler or mix it with the residual 800 nm beam from the second pass to produce visible sum-frequency. This visible output is then sent through a compressor, which consists of two triangular Brewster-angle prisms and a reflecting mirror, to temporally compress the visible light.

2.2.1.1 Optimization of the OPA

To maximize the power from the OPA we take the following steps [95]. Beginning with the first pass, we adjust the 800 nm wave plate before the thin film polarizer and tweak the translation stage that holds the lens which focuses on the sapphire crystal to generate an intense, stable WL seed. The indicator of a good seed is a uniform central white spot surrounded by a red ring. Adjusting the compressor of the 800 nm laser is also needed to stabilize the WL. After getting a stable and intense WL, we adjust the last two turning mirrors which the WL has not passed yet and DM1 which reflects the 800 nm pump of the first pass to make the 800 nm beam go through the same path as the WL. With some adjustment of the translation stage for the first-pass 800 nm beam, the 800 nm beam (the pump) and the WL (the seed) temporally overlap. When spatially and temporally overlapped, the pump and the seed generate infrared light. Through a cascaded second-order process, the amplified infrared light doubles or mixes with the pump in the BBO crystal, and produces visible light with a distinct, crystal-angle-dependent color. We also adjust the position and the angle of the concave mirror behind the sapphire crystal to optimize the spatio-temporal overlap of

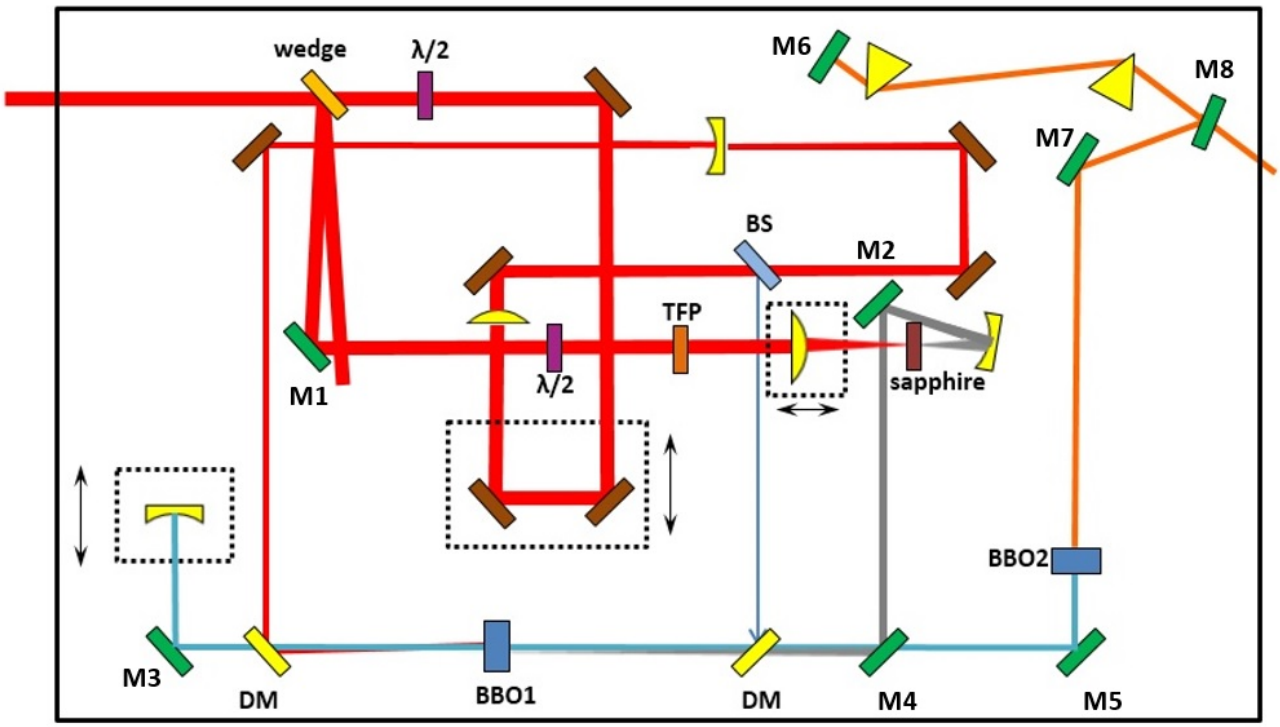

Figure 2.1: Setup of the optical parametric amplifier. The power of the incoming 800 nm beam before the OPA entrance is $\sim$ 0.5 to 1 W. $\lambda/2$ represents the half wave plate. BS represents a 20/80 beam splitter with 80 % of the power sent to the second pass. TFP represents a thin film polarizer. DM represents dichroic mirrors. The boxes with dashed lines represent translation stages in the OPA setup. All the beams that do not pass the TFP have linear polarization parallel to the table surface and the beam after the TFP has linear polarization vertical to the table surface. Typically we can get a few hundred mW out of the OPA with the power depending on output wavelength.

the seed and the pump. After the first pass has been optimized, we adjust the angle of the concave mirror on the translation stage and two turning mirrors so that the second-pass 800 nm beam follows the same path as the reflected infrared beam from the first pass. After that, we tweak the translation stage that holds the concave mirror that reflects and collimates the IR from the first pass to create the same optical path length for the first and second passes.

The process above yields a high-power signal with vertical polarization and an idler with horizontal polarization. There is also weak visible light from secondary, non-phase matched, second-order processes (from infrared light doubling or mixing with 800 nm). We eliminate the visible light by using an appropriate long pass filter and sending the infrared light through another appropriately oriented BBO crystal (BBO2 marked in Figure 2.1) to double the frequency or mix with 800 nm light in a sum-frequency process to and get light from 470 nm to 730 nm. In this BBO crystal, the vertically polarized signal generates horizontally polarized visible light.

In the experiment, when the surface of the BBO crystal is perpendicular to the incident beam, the power of the infrared light is maximum. This is convenient for initially establishing spatio-temporal overlap of the seed and first-pass pump.

The visible light is compressed by a pair of Brewster-angle prisms. The prism angles are optimized by rotating a prism about an axis normal to the optical plane so that the lateral displacement of the transmitted light is minimized. We then tweak the vertical knob of the reflecting mirror (M6 in Figure 2.1) to get the reflection slightly higher than incident beam so that it bypasses the turning mirror (M8 in Figure 2.1) which sends the beam into the compressor. This WL then serves as the probe in our TA experiment.

2.2.2 Data collection and Labview VIs

As stated at the beginning of Section 2.1, we use the CCD spectrometer to perform broadband photon detection and we use an amplified Si or InGaAs photodiode at the output of a spectrometer to perform single-wavelength photon detection where the CCD spectrometer is insensitive. The experimental details are introduced in the following.

2.2.2.1 Broadband measurement by CCD

We use an Ocean Optics USB2000+ CCD array spectrometer that can detect photons with wavelength from 340 nm to 1032 nm. As discussed at the beginning of Section 2.1, we need to determine the difference in probe transmission of a sample between when it is excited and when it is unexcited to get the change of the absorption coefficient. As we use an optical chopper to turn the pump on and off, such measurement requires precise synchronization between the CCD and the chopper.

The ideal scenario is one in which we can collect our entire probe spectrum on a shot-by-shot basis while simultaneously chopping alternate pump pulses on and off. This would minimize the impact of pulse-to-pulse fluctuations and also allow us to selectively throw out pulses in which the probe energy shows abnormally large fluctuations (e.g., due to pulses dropping out of the continuum generation or probe scattering by small particles when a sample solution is stirred). Because the laser in our lab has a repetition rate of 1 kHz, we would need to be able to perform a full cycle of triggered acquisition and readout in 1 ms. As described below, this is not possible with the USB2000+, and we must carefully synchronize slower chopping of the pump with slower CCD integration rates.

The limits on the CCD timing are shown in Figure 2.2 [96]. The minimum trigger cycle is 2.909 ms with a minimum integration time of 1 ms in hardware edge trigger mode. In other words, for our measurement, the time that the spectrometer is not integrating signal is about 1.909 ms per cycle.

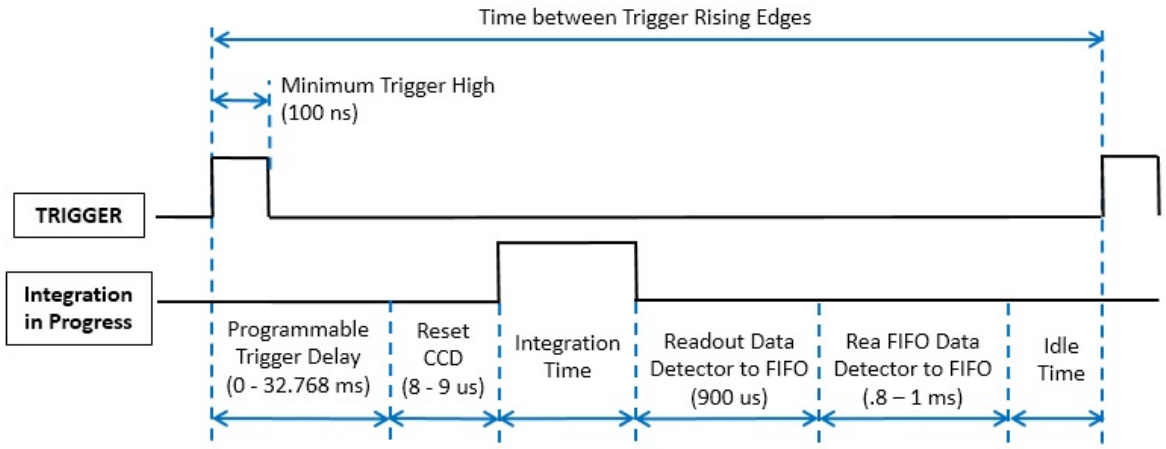

Additional Delay	**0 us**
Initialize CCD Binning	**9 us**
Integration time	**1000 us**
Read Detector	**900 us**
Minimum Idle States	**1000 us**
Min Trigger Cycle	**2909 us**
Min Trigger Cycle	**2909 us**
Max Trigger Rate	**344 Hz**

Figure 2.2: USB2000+ hardware edge trigger mode time table

If the measurement is performed with a period of 3 ms, the device can collect only 1 pulse and will drop 2 pulses in each cycle. When tested with the Labview program described below, the system cannot stably acquire data so rapidly. This suggests that the device cannot reach the minimum specified trigger cycle of 2.909 ms. Even though this is the best way to reduce the impact of fluctuations on single pulses, one-third efficiency of data collection is a high price to pay. In order to balance between data fluctuations and collection efficiency, we

choose the collection period to be 6 ms, which means that we can get 4 pulses but only lose 2 pulses within each measurement. In practice, we choose the integration time to be 3.8 ms. This choice of the integration time will be discussed later. However, when choosing the exact integration time, we should also consider the signal level from a single pulse relative to the saturation intensity of the detector. If the signal level is so high that saturation occurs in a single pulse, then using the minimum integration time the system can handle is preferred.

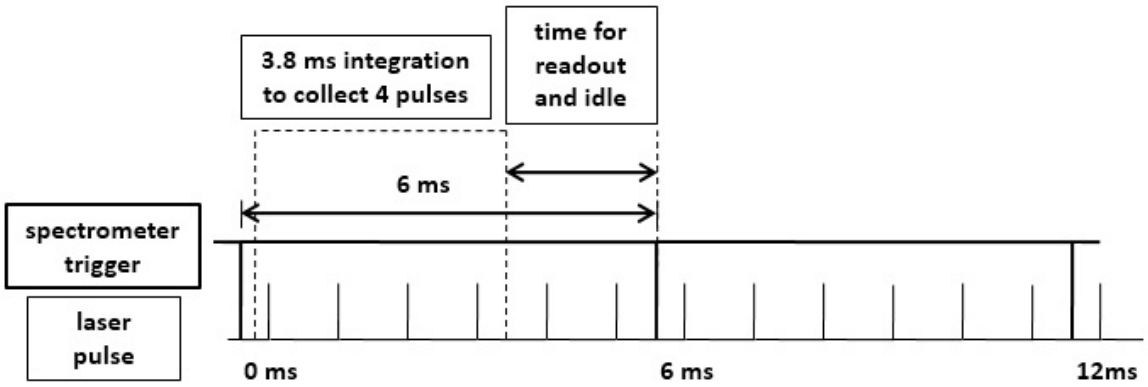

Figure 2.3: Timing of spectrometer trigger

Figure 2.4 shows the basic layout of all the connections between the measurement devices. A pulse delay generator (Stanford Research Systems, Model DG535) is triggered by the laser SYNCH pulse (a TTL output sequence from the laser synchronized with the laser output) and is set to produce an output with a period of T = 6 ms. The optical chopper controller receives the pulse generator output and chops the beam at half the pulse generator output frequency. Thus, the pump is chopped with a period of 12 ms. Finally, the USB2000+ spectrometer is synchronized by the output of the pulse generator and produces spectra every 6 ms.

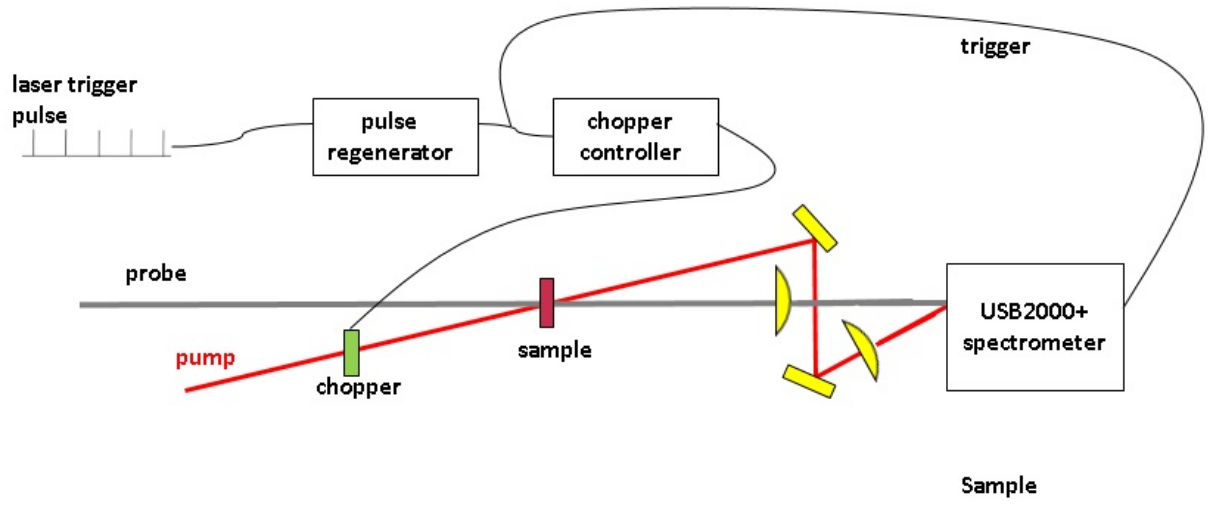

Figure 2.4: Layout of optical paths and electrical connections

Table 2.1: 22-pin accessory connector pinout diagram when facing the 22-pin Accessory Connector on the front of the vertical wall of the USB2000+

20	18	16	14	12	10	8	6	4	2	A2
19	17	15	13	11	9	7	5	3	1	A1

To collect data from the USB2000+, we use a Labview program to set the parameters (number of scans, delays, etc.), read data, and write data to files. The program is based on a Certified Labview Plug and Play (project-style) Instrument Driver [97]. A new driver (NI-VISA) is required for using this Labview program. This driver is incompatible with the SpectraSuite software from Ocean Optics, and drivers need to be reinstalled when switching between the Labview program and SpectraSuite. In the Labview program, the VISA source name for the connection will indicate a USB connection.

We adjust the delay in the pulse generator so the phase between the laser trigger pulse and USB2000+ trigger sequence yields stable data acquisition. The phase between the USB2000+ trigger sequence and the chopper sequence can be adjusted by adjusting the phase control of the optical chopper. By monitoring the intensity of scattered pump light collected by the spectrometer, we can tell whether the pulse is fully blocked or clipped by

Table 2.2: Definitions and descriptions of pin 6 and 7, which are used to connect with the USB2000+ trigger source [1]

Pin	Function	Input/Output	Description
6	Ground	Input/Output	Ground
7	External Trigger In	Input	TTL input trigger signal

Figure 2.5: Location of USB2000+ Accessory connector

the chopper blade. If the spot size of the beam is not too big compared to the blade width of the chopper, then during the 12 ms period of the chopper sequence, we can make the first 6 ms correspond to the chopper ON state (not blocking the pump beam) and the next 6 ms to the chopper OFF state (blocking the pump beam), as illustrated in Figure 2.6.

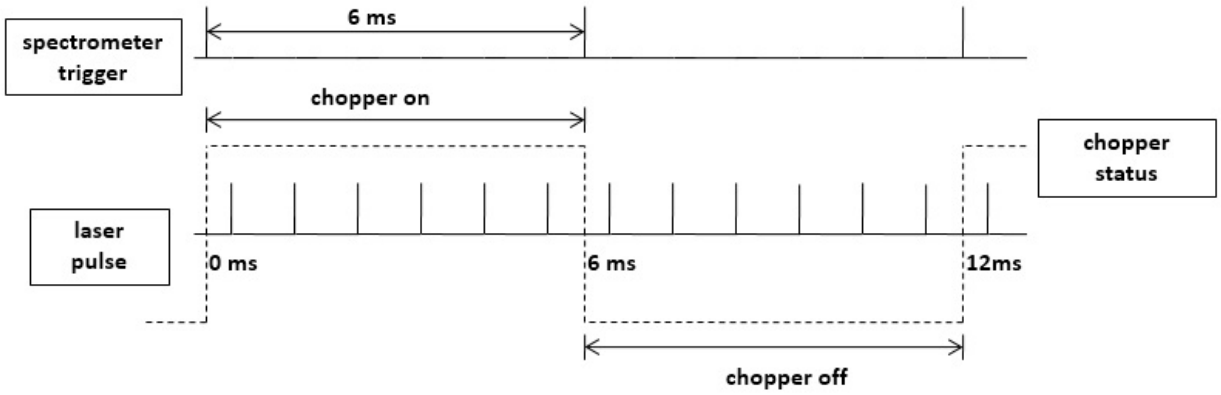

Figure 2.6: Timing diagram for chopper and spectrometer trigger

In general, if we wish to integrate N pulses per acquisition period and we lose two pulses

due to readout and idle time, not too big means that the pump beam should have a diameter, d, described as $d \leq \frac{3w}{N+2}$, where w is the chopper slot width and the factor of 3 is calculated from our 6 ms chopper on time and 1 ms pulse separation. In the present case, N=4 so the beam diameter must be less than 1/2 of the blade width. If this criterion is not met, pulses at the beginning and/or the end of the ON and OFF integration times may be clipped by the edge of the chopper and might not be entirely ON or OFF. One must confirm that none of the N pump pulses of interest should be clipped by the chopper. One way to confirm this is to monitor the scattered pump spectrum and reduce the integration time in increments of one laser period. If the intensity of the resulting spectrum decreases linearly, this means that the chopper is not clipping the pump pulses of interest. If clipping is observed, the phase of the chopper must be adjusted.

Suppose that we want to perform a TA measurement with each pump ON/OFF cycle consisting of spectra from 4 pulses each with pump ON or OFF. Time counting in the Labview program is used to confirm that the time we actually used matches the expectations. Based on the device specifications, we may capture 4 pulses out of 6 by using an integration time from 3.1+δ ms to 5.0-δ ms as long as the phase differences between the spectrometer trigger sequence and the laser trigger pulse is appropriately set. We set the trigger sequence slightly earlier (0.15 ms) than the laser trigger pulse sequence, and set the integration time to be 3.8 ms. According to the clock in the Labview program, it takes 6 ms for each acquisition, as expected.

In reality, when the Labview TA program is running, one cannot rely completely on the presumed timing described above. For unknown reasons, the detector may miss one laser pulse due to the communication between the detector and the computer, so the determination of the pump ON and pump OFF signal will occasionally fluctuate in the Labview program

(typical probability of $\sim 0.3\%$). To account for this, we use a reference light source (an inexpensive 3 eV diode laser) to go through the chopper at the same location as the pump. This ensures that our reference beam has the same ON/OFF status as the pump. We scatter part of this this reference light into the CCD to serve as a monitor of the ON/OFF status of the pump. The intensity of the reference beam should just have two different levels, maximum when unblocked and zero when blocked; the CCD should not yield any intermediate signal levels. We measure the intensity of these two levels of the reference beam before every measurement and set a threshold for sorting each spectrum in LabView according to whether the pump is ON or OFF.

2.2.2.2 Single-wavelength measurement by photodiodes

For single-wavelength dynamics traces and measurements where the spectrometer is insensitive, detection is performed with an amplified Si (Thorlab DET36A) or InGaAs photodiode (Thorlab DET10D) at the output of a spectrometer (Acton SP300i, typical resolution ~ 5 nm) and gated by a boxcar integrator.

We apply different detector devices to cover as large a detection range as possible. Our CCD spectrometer can detect signal from 340 nm to 1032 nm with 2 nm resolution. The amplified InGaAs photodiode can detect signal from 1200 nm to 2600 nm. And the amplified Si detector has a detection range from 350 nm to 1100 nm. The data acquisition is performed by a data acquisition card (National Instruments PCIe-6321) which collects the voltage signal from the boxcar (which reads the photodiode's signal) and laser SYNCH. The collected information is then transferred to the computer to be further processed and analyzed. The frequency of the optical chopper for the pump is half of the laser repetition rate and our Labview program is designed to record the signal from every laser pulse. The intensities of

the sorted signals are $I_{\text{on}} = I_0 \cdot e^{-(\alpha_0+\Delta\alpha)l}$ and $I_{\text{off}} = I_0 \cdot e^{-\alpha_0 \cdot l}$, where α is the absorption coefficient, $\Delta\alpha$ is the change of the absorption coefficient, and l is the path length of the beam of light through the material sample. From these two quantities, we obtain the change $\Delta\alpha$ from $-\Delta\alpha \cdot l = \ln(\frac{I_{\text{on}}}{I_{\text{off}}})$.

For TA measurements, we have developed different Labview VIs to integrate parameter setup, data acquisition and data processing. A flow chart of the Labview data acquisition and processing VI is shown in Figure 2.7. To make the Labview VIs more efficient, we process data acquisition and data processing in parallel. For dynamics measurements, we acquire data from the measurement device (CCD or photodiode) at one delay position, store the data and process the data from last delay position which is stored previously at the same time. For the measurement of a TA spectrum at a certain delay when using a single-channel detector, the idea is similar to the dynamic measurement. we collect and store data at one wavelength and the data are processed at the same time as we collect data at the next wavelength.

2.2.3 TA setup optimization

The configuration of our TA measurement is shown in Figure 2.8.

2.2.3.1 TA setup

We use a 250 mm mechanical stage to adjust the temporal delay of the probe relative to the fixed pump. One reason that we delay the probe is that the spot size of the pump is larger than that of the probe. If there is a small change of probe position or size because of the variable delay, our pump and probe are still spatially well overlapped. Also, we choose to delay the weak 800 nm beam in the probe path before we generate the WL, because the 800

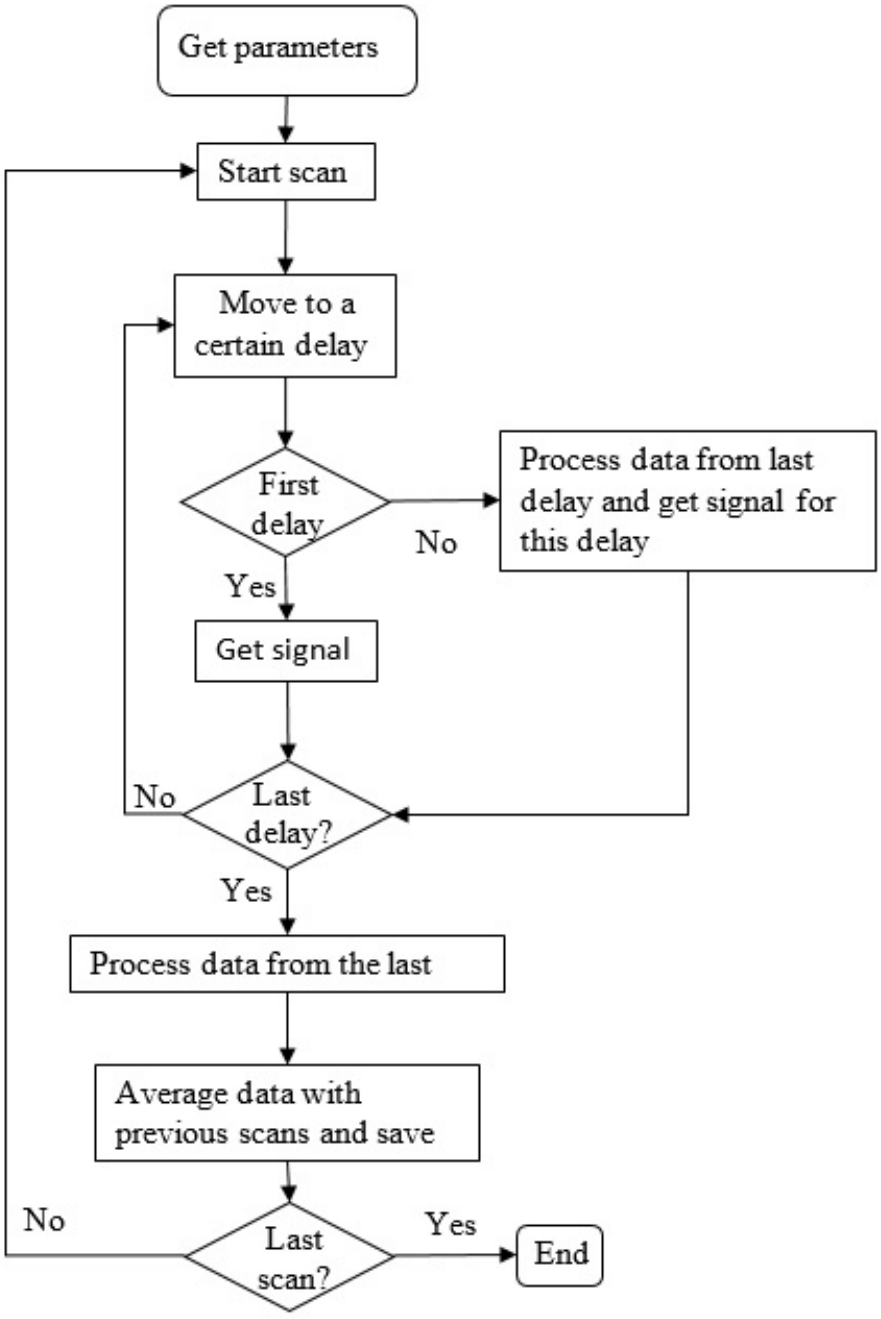

Figure 2.7: Flow chart of Labview VI (dynamic measurement)

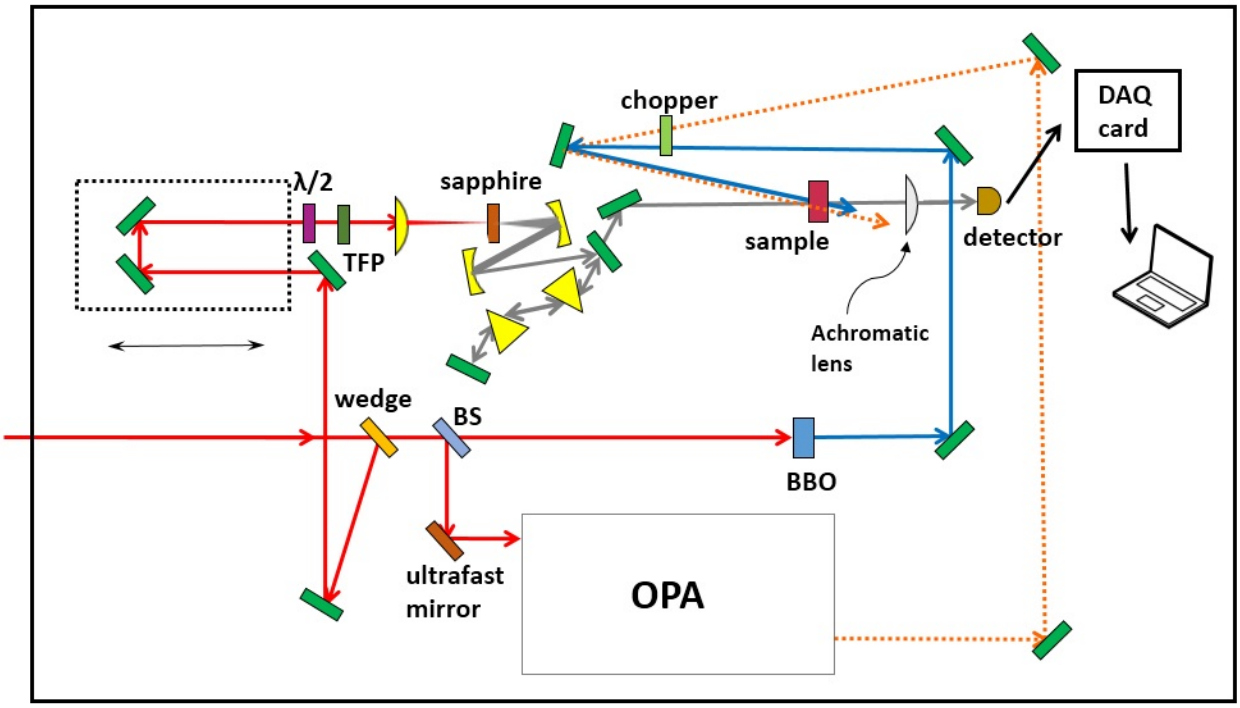

Figure 2.8: Configuration of TA measurement

nm beam from the amplifier is the best collimated beam in our setup. This then minimizes delay-dependent intensity changes associated with imperfect collimation.

Off-axis parabolic mirrors rather than lenses are used in TA setup to focus the WL into the sample and then recollimate the light after the sample. Off-axis parabolic mirrors help us to minimize the dispersion introduced in the WL probe, minimize chromaticity in focusing, and also eliminate spherical aberration. This is especially useful when we use a CCD detector to measure the transient absorption over a broad spectral range.

When chopping at half the laser repetition rate, adjustment of the chopper phase is straightforward. If we place a white business card behind the chopper and look at the blades from the back side while they are illuminated by the light scattered from the card, the blades will appear stationary. The phase is then adjusted so that the stationary window between blades is centered on the transmitted beam. Alternatively, we can set the chopper frequency

to the repetition frequency of the laser. The phase is adjusted to the center of the range where the pump is completely transmitted. When we go back to half the laser repetition frequency, the chopper will be perfectly phased for chopping alternate pulses.

Sometimes, we observe a slight difference in the pump on and off signals at negative delays, i.e., before the pump arrives. One possibility is that the reflection created by the walls of the cuvette reflects the probe beam which generates an extra weak probe with slightly longer delay. Another possible source of such a difference is photoluminescence, which appears as a constant contribution to the difference of pump-on and pump-off signals. This can be accounted for by taking the difference between positive- and negative-delay signals.

2.2.3.2 Alignment procedure of our TA setup

Since the probe and pump beams may slightly shift day-to-day, we need to align the system periodically, which includes optimizing the stability of the WL continuum, overlapping the pump and the probe at the sample position and some other procedures.

The power of the Ti:sapphire regenerative amplifier drifts over time. This can cause instabilities in the WL intensity and spectral shape but can be compensated by small changes in intensity or spatial mode of the 800 nm pulse at the sapphire crystal. These changes can be done by adjusting the focusing or delay-stage exit iris. Typical pulse-to-pulse WL fluctuations are 0.4% to 0.6% (standard deviation).

A pinhole positioned at the focus of the WL probe is used to optimize the overlap of the pump and probe and ensure that the delay stage is well aligned. We send the WL signal through the pinhole and make sure that there is negligible change in the ratio of the power through the pinhole to the power without pinhole at any delay position. When using a

1-mm-pathlength cuvette, the sample stage is moved about 0.3 mm closer to the WL source to compensate the cuvette thickness. To find the optimized overlap position for our sample, we fix the WL delay stage for maximum TA signal and then adjust the sample position to further maximize the signal.

It is crucial to well align the probe beam into the delay stage so that the light hitting a small spectrometer slit does not move during the experiment. If the alignment of the delay stage is perfect, we should get the same fraction of power transmitted by the pinhole at any delay position.

In order to determine the pump and probe spot sizes and determine the excitation fluences, we record the fraction of WL and pump power transmitted by the pinhole. We estimate spot sizes by assuming that they are circular Gaussian spatial modes for which the intensity passing through a circle of radius r is $I(r) = I_0 \exp(-\frac{2r^2}{d^2})$. The spot size can be described as:

$$d = D \times \left\{ \ln\left(1 - \frac{P_{\mathrm{PH}}}{P_{\mathrm{no\ PH}}}\right) \right\}^{-\frac{1}{2}} \tag{2.1}$$

where D is the diameter of the pinhole and P_{PH} and $P_{\mathrm{no\ PH}}$ are the power measured with and without the pinhole.

Usually, the spot size of the probe (WL) in our experiment is comparable to the 100 μm diameter of the pinhole we use. The diameter of the pump is from 0.6 to 2 mm depending on the available pump power and desired intensities for a particular measurement. We adjust the WL focusing as tightly as possible and make the spot size of our pump large enough so that in the absence of absorption there would be a roughly constant fluence over the probe path.

Given the spot size and intensity of the pump and the cross section of our sample, we

can estimate the average number of photons that are absorbed per pulse by each quantum dot:

$$< N_{\text{abs}} >= \frac{4P_{\text{no PH}}}{\pi d^2 \cdot R \cdot E_\lambda}\sigma \tag{2.2}$$

In this equation, R is the repetition rate of the laser, E_λ is the energy of a pump photon, and σ is the cross section of the sample at the pump wavelength. For the GQDs in our experiments, the reported cross sections at 400 nm for C132 and C168 are respectively 2.0×10^{-16} cm^{-2} and 3.78×10^{-16} cm^{-2} [8].

When the pump is generated by the OPA, to obtain a more stable WL and maximum power from the OPA, tweaking the compression of the amplifier may be also needed. The most stable WL and maximum power OPA may require different compressions, which means that we need to find balance between the two by adjusting the compression.

There are a few subtle details that need to be kept in mind to ensure the accuracy of the measurements. For example, the pump should not be too strong at the sample position. This is because a high intensity pump can cause a refractive index change in the sample solution that results in a delay-dependent shift of the probe position or spatial mode. If the shift is sufficiently large, it may produce changes in spectrometer-slit transmission unconnected to the quantum dot response may occur leading to inaccurate assessments of pump-induced changes in probe transmission by the sample. We use an achromatic lens to focus the probe into the detector to get the size as small as possible across the visible spectrum, so we can reduce the effect from beam shifts if there are any. The resolution of the TA experiment is determined not only by the pulse duration but also factors like crossing angle between the pump and probe. When the pump and the probe are colinear (zero crossing angle), the temporal cross-correlation between the overlap of these two beams is minimum. In reality,

there is an angle ($\sim 7.5^\circ$) between the pump and the probe beams in our TA experiment, but it only reduces our resolution to 150 fs, which is acceptable in our experiment.

2.3 Upconversion of photoluminescence

In a TA experiment, the change in absorption reflects presence of electrons and/or holes in the states involved in a given transition, so $\Delta\alpha$ depends on the sum of electrons and holes. In contrast, emission occurs only when an electron-hole pair recombines, so the photoluminescence signal scales as the product of the number of electrons and holes in the states between which emission takes place. By combining the results from these two experiments, we get a clearer view of the electronic structure and the relaxation pathways of our sample under different conditions.

The technique we use for temporally resolving the emission is upconversion of photoluminescence (uPL), which was described in detail by Jagdeep Shah [98]. Upconversion is a nonlinear process in which one PL photon and one gate photon annihilate and generate light at the sum frequency of the two annihilated photos. In contrast to TA, which has many different contributions, the upconversion measurement does not include any induced absorption contributions, and the method is background-free, thus allowing for more straightforward identification of the relevant states.

As shown in Figure 2.9, the 800 nm beam from the laser passes a wedge to generate a weak reflection. The beam that goes through the wedge is split by a 50/50 beam splitter (BS). After the beam splitter, one of the two beams goes through a 250 mm mechanical delay stage controlled by computer and then a neutral density (ND) filter wheel for adjusting the power. Eventually this beam is sent to the BBO crystal (type II, theta=27.2 degree, 8×8×0.6

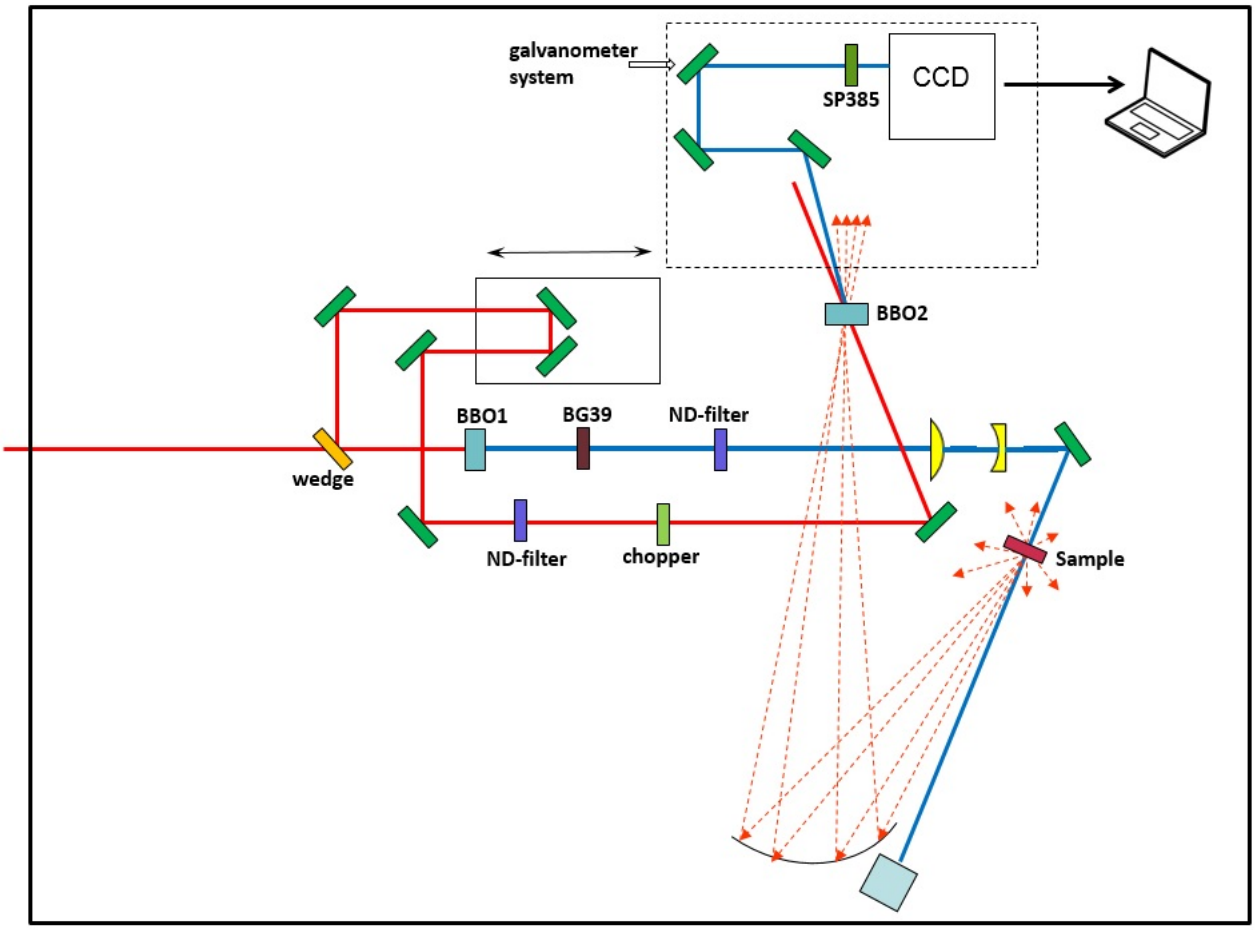

Figure 2.9: Setup of uPL measurement

mm) used for upconversion. The other beam is sent through a BBO crystal to produce 400 nm light by second harmonic generation. The 400 nm beam serves as the excitation beam in our experiment. A BG39 filter eliminates the residual 800 nm beam from the doubled light. The 400 nm pump intensity is adjusted with a ND filter. A Galilean telescope is used to set the proper spot size of the excitation beam on the sample. The optical chopper in the 400 nm beam path is synchronized with the laser pulses and set to half the repetition

rate of the laser. After excitation, the sample luminescences in all directions. We use a large ($2''$ in diameter) concave mirror with four-inch focal length to collect the luminescence and redirect it to meet the 800 nm gate in the BBO upconversion crystal, which is tuned for phase matching of the upconversion process. The distance from the sample to the concave mirror is about 6 inches and that from the concave mirror to the BBO crystal is about 12 inches. In the end, several turning mirrors send the uPL signal to a spectrometer (SpectraPro 2300i, Princeton Instruments) on which a thermoelectrically cooled CCD array (Princeton Instruments model 1024HER) is mounted. The last mirror in front of the CCD is mounted on a galvanometer that is synchronized with the optical chopper, so as to reflect the pump-on (signal) and pump-off (background) signals to different heights at the entrance slit (and so on the CCD) for background subtraction. Because the GQDs emit at 670 nm, the upconverted light is close to the second-harmonic at 800 nm. Therefore, one of the main sources of background noise is the second-harmonic generation (SHG) from the gate 800 nm pulse in the upconversion crystal. Further background is due to cascaded parametric generation and upconversion produced by the gate. These are critical issues particularly in studying the graphene quantum dots because of their weak emission, which makes galvanometric detection essential. A shortpass filter (Newport SP 385) just in the front of the spectrometer allows us to reduce the background, especially that from SHG of the gate. Enclosure of the detection allows us to further reduce the background.

The mixing process is efficient only if phase-matching. We adjust the angle of the crystal to get phase matching for different photoluminescence wavelengths.

Since the luminescence from C132 graphene quantum dots is in the range of about 650 nm to 820 nm, the upconverted light is in the range of about 358 nm to 404 nm and weak and so cannot be seen by eye. In order to align the optics after the upconversion crystal,

we remove the BG39 filter from the pump path and replace the sample with something scatter the light. This provides an 800 nm beam that follows the exact same path as our luminescence signal does. Even though the crystal angle may be slightly different from the angle at which the luminescence is upconverted, there is little difference in the beam direction. The 800 nm pulse is upconverted to 400 nm at the appropriate angle for phase matching, and this can be seen by eye. By utilizing this upconverted 400 nm beam, we can align the last 3 turning mirrors before the spectrometer and then return to the configuration for upconverting luminescence from the sample. When adjusting the angle of the BBO crystal back to the angle for upconversion of sample photoluminescence, we may slightly translate the position of the crystal as well to ensure that these two beams are still spatially overlapped well in the BBO crystal.

2.4 Samples studied in this thesis

C132 and C168 are synthesized by Liang-shi Li's group [8]. We received dry GQDs and dissolved the GQDs in anhydrous toluene. For the experiments I present in this dissertation, all GQD solutions were prepared in a glove box with a nitrogen atmosphere. Both C132 and C168 GQDs were dissolved in 99.7% water-free toluene, and the solutions were sealed in air-tight fused silica cuvettes with path lengths of 1 mm or 10 mm. We use the ground-state absorption and photoluminescence spectra to regularly monitor the sample. Ground-state absorption spectra are measured by a UV-visible spectrophotometer (Varian Cary 50 Bio UV-Visible Spectrophotometer) and the photoluminescence spectrum is measured by a phosphorescence/fluorescence spectrofluorometer (PTI QuantaMaster 300).

Chapter 3

Biexciton Binding

3.1 Introduction

3.1.1 Biexciton binding in quantum confined systems

The Coulomb interaction is inversely proportional to the distance between two charges and to the dielectric constant. With reduced spatial separation of electron and hole, the binding energy of an exciton can increase quickly [99]. Similarly, a reduction in the effective dielectric constant in lower-dimensional materials can also enhance the binding energy. Theoretical studies have shown that quantum confinement significantly increases the biexciton binding energy of bulk semiconductors [100, 101, 102, 103]. In bulk GaAs, the binding energy of an exciton is ∼4.9 meV, while the exciton binding energy in GaAs-$Al_xGa_{1-x}As$ quantum wells can be three times as high as that in bulk (∼ 13 meV with GaAs well thickness 42 Å)[104]. Similarly, the biexciton binding energy rises from 0.5 meV in bulk GaAs [105] to 2.2 meV in GaAs-$Al_xGa_{1-x}As$ quantum wells with GaAs well thickness 100 Å [103]. In semiconductor quantum dots, confinement in three dimensions increases the binding of the biexciton even more [106, 107]. Compared to other semiconducting systems, carbon-based quantum dots are made of relatively light atoms. This results in even further reduced screening and a smaller dielectric constant. The binding energy of a single exciton in single-walled carbon nanotubes (SWCNTs) is measured to be as large as 0.4 eV [72, 80]. The binding of biexcitons

in SWCNTs is found to be correspondingly strong. In (9, 7) SWCNTs (diameter=1.1 nm [108]) in gelatin, the biexciton is bound by 105 meV, which is ∼40% of the single-exciton binding energy of 250 meV [109].

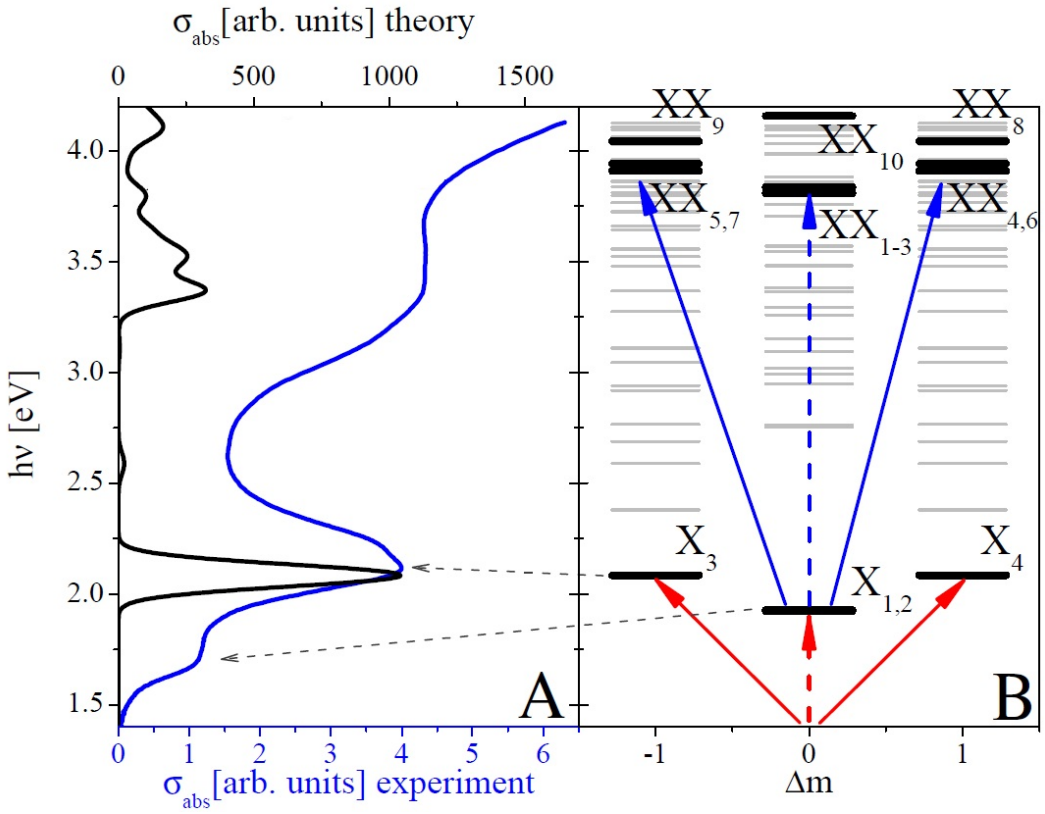

Figure 3.1: (A) Experimental (blue) and theoretical (black) ground state absorption of C168. (B) Calculated band-edge singlet exciton (X) and biexciton (XX) states (black lines) derived from the degenerate HOMO and LUMO states. Grey lines show excited exciton states accessible from $X_{1,2}$. Dipole-allowed electronic transitions, which correspond to a change in Δm of ± 1, from the ground state and from the lowest singlet exciton states are shown respectively by solid red and blue arrows. Dashed arrows indicate optically dark electronic transitions. [14]

We described the theoretical calculation of the energies of different electronic transitions in GQDs in Chapter 1 using a single-particle picture. To better understand the electronic structure of such GQDs, Isil Ozfidan and Pawel Hawrylak [15] performed more detailed

calculations. Because of the three-fold rotational symmetry of C168, the electronic states can be labelled by the quantum numbers m =0, ±1 with optically bright transitions occurring only between states where Δm= ±1, as demonstrated by both tight-binding and ab-initio calculations in Figure 3.1(B).

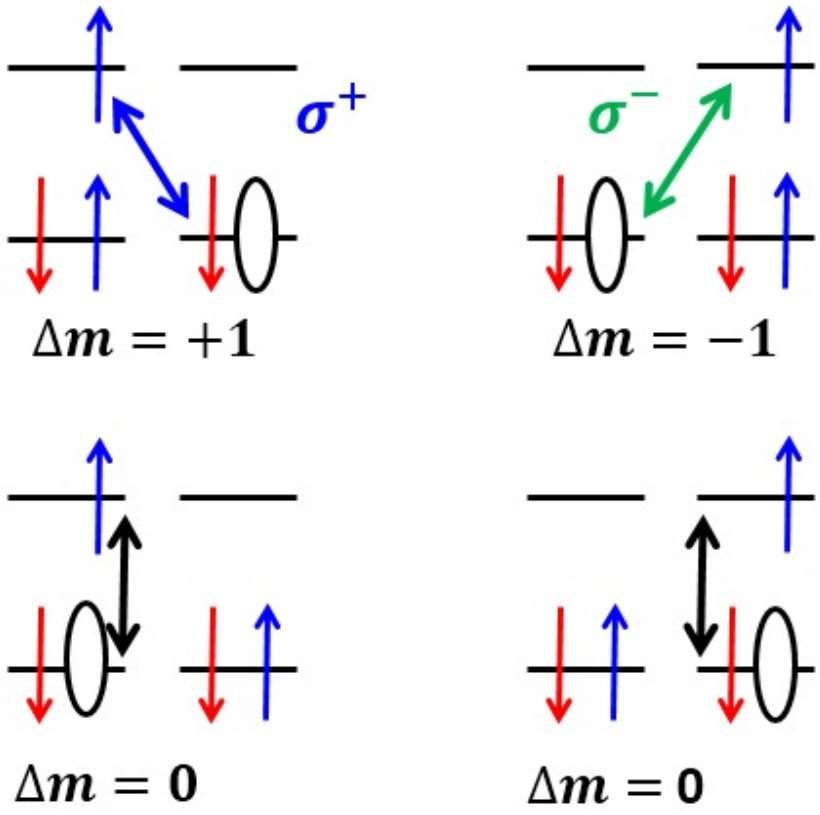

Figure 3.2: Single-pair excitation with total angular momentum Δm=±1 (optically bright exciton) and Δm=0 (optically dark exciton) (reproduced from Ref. [15]).

Because of the two-fold degeneracy of the HOMO and LUMO states, there are four different band-edge singlet excitons as shown in Figure 3.2. The calculated absorption spectrum is represented in Figure 3.1(A) by the solid black line, and the experimental absorption spectrum is represented by the solid blue line in the same figure for comparison. The energy

states from the theoretical calculation are marked in Figure 3.1(B) by solid black lines and grey lines. The lowest-energy states (X_1 and X_2), which we denote collectively as LX, are two-fold degenerate around 1.7 eV. Based on the calculation, the LX states are optically dark in the absence of coupling to phonons [15, 65]. When coupled with phonons [11], LX states can yield the absorption shoulder at 1.7 eV shown in Figure 3.1. The main peak at 2.1 eV in the experimental absorption spectrum is associated with the two-fold degenerate band-edge bright singlet excitons (marked as X_3 and X_4 in the figure).

Ozfidan performed configuration interaction (CI) calculations of the low-energy single- and biexciton electronic states of C168. The electronic tight-binding Hamiltonian of the GQD describing interacting electrons in p_z carbon orbitals is expressed as follows:

$$\hat{H} = \sum_{i,l=1}^{N} \sum_{\sigma} \tau_{il} c_{i\sigma}^{+} c_{l\sigma} + \frac{1}{2} \sum_{i,j,k,l} \sum_{\sigma,\sigma'} \langle ij|V|kl\rangle c_{i,\sigma}^{+} c_{j,\sigma'}^{+} c_{k,\sigma'} c_{l,\sigma} \tag{3.1}$$

where $c_{i,\sigma}^{+}$ represents the creation operator for an electron of spin σ in the i^{th} orbital. In the expression, the first term is the one-electron tight-binding Hamiltonian, and the second term, $\langle ij|V|kl\rangle$, describes the screened electron-electron interactions, $V(\vec{r} - \vec{r'}) = 2/(\kappa|r - r'|)$ [15]. With this expression, the HF calculation is performed by rotating the $c_{i,\sigma}^{+}$ site operators into HF operators $b_{j,\sigma}^{+}$, where j are HF states. The ground and excited states of the GQD are then expanded in multi-pair excitations out of the HF ground state $|0\rangle$, $|v\rangle = k_0|0\rangle + \sum_{i,j,\sigma} k_{ij}^{v(1)} b_{i\sigma}^{+} b_{j\sigma}|0\rangle + \sum_{i,j,k,l} \sum_{\sigma 1 \sigma 2} k_{ijkl}^{v(2)} b_{i\sigma 1}^{+} b_{j\sigma 2}^{+} b_{k\sigma 1} b_{l\sigma 2}|0\rangle + ...$ The CI Hamiltonian matrix is built in the space of multi-pair excitations and diagonalized numerically. There are many available states with high energy in GQDs. We focus on the states with the lowest energies , which are the ones contributing to the low-energy excitons and

biexcitons that we probe, by including only states below a cutoff energy. To account for Auger coupling in CI calculations, HF states within an energy window of $3E_g$ are kept in the calculation. A cutoff of $E_{\mathrm{XX}} < 3E_g$ for XX energies is used to reduce the CI-Hilbert space. The tunneling matrix elements in Equation 3.1 are chosen as $\tau = 4.2$ eV for nearest neighbors and $\tau' = -0.1$ eV for next-nearest neighbours to give bright singlet excitons at 2.128 eV, close to the strong absorption peak measured at 2.1 eV. Meanwhile, the dielectric constant, which determines the bright-singlet-dark-triplet splitting, was chosen as $\kappa = 5$, similar to the expected value for extended graphene in toluene [71], to reflect screening by sigma electrons and surrounding fluid. Similar to the characterization of single-exciton states, biexciton states are characterized by total Δm$= 0, \pm 1$.

Extrapolated band-edge singlet exciton (X) and biexciton (XX) states derived from the degenerate HOMO and LUMO states are illustrated in Figure 3.3. The transition from $\mathrm{X}_{1,2}$ to XX_{1-3} is orbitally forbidden but becomes allowed due to electron-phonon coupling. States XX_{4-7} can be formed by absorption of $\sigma+$ or $\sigma-$ photons from the orbitally dark $\mathrm{X}_{1,2}$ states. $\mathrm{XX}_{8,9}$ states can be formed from the ground state by absorption of ($\sigma+$,$\sigma+$) or ($\sigma-$,$\sigma-$) photons and X_{10} can be formed by absorption of ($\sigma+$, $\sigma-$) photons. The XX_{8-10} states quickly cool to the lowest (dark) states, so that they are only accessible before this cooling.

3.1.2 Experimental techniques for measuring biexciton binding

Photoluminescence and transient absorption measurements are typical methods used in the study of excitons and biexcitons in quantum confined systems. In a photoluminescence measurement the amplitude of the photoluminescence is proportional to the average product

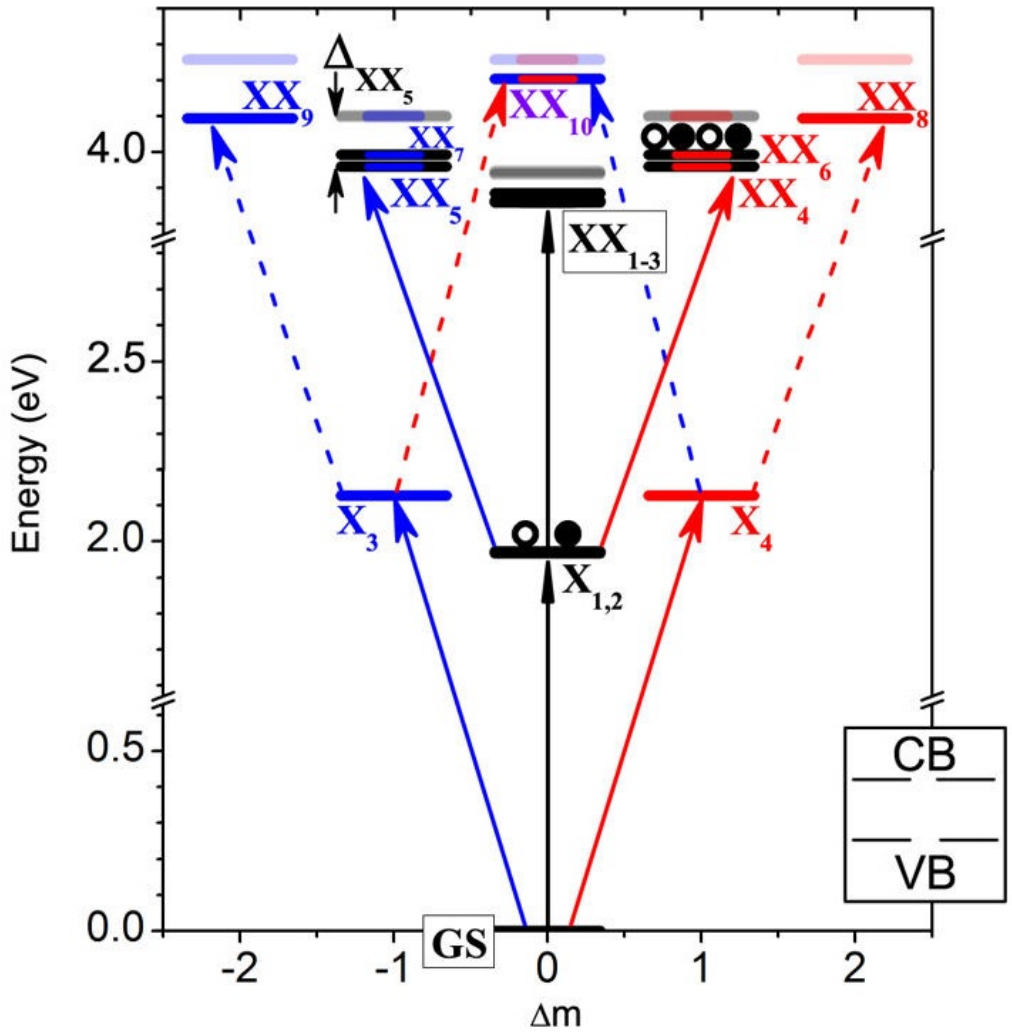

Figure 3.3: Predicted exciton (X) and biexciton states (XX) in GQDs. Dipole-allowed electronic transitions, corresponding to $\Delta m = \pm 1$, are labeled with arrows. Red(blue) arrow represents $\Delta m = +1(-1)$ corresponding to $\sigma+(\sigma-)$ photon polarization [14].

of the number of electrons and holes per GQD. Hence, a photoluminescence signal can be detected only when carriers populate both the valence and conduction bands. In principle, we may obtain a higher signal-to-noise ratio (SNR) than that in TA, and with fewer states involved in the generation of photoluminescence, it might be a more straightforward method than TA to characterize the exciton transitions.

We set up an upconversion of photoluminescence (uPL) measurement as described in Chapter 2. GQDs are pumped at 3.1 eV, and photoluminescence is detected at different photon energies, as shown in Figure 3.4.

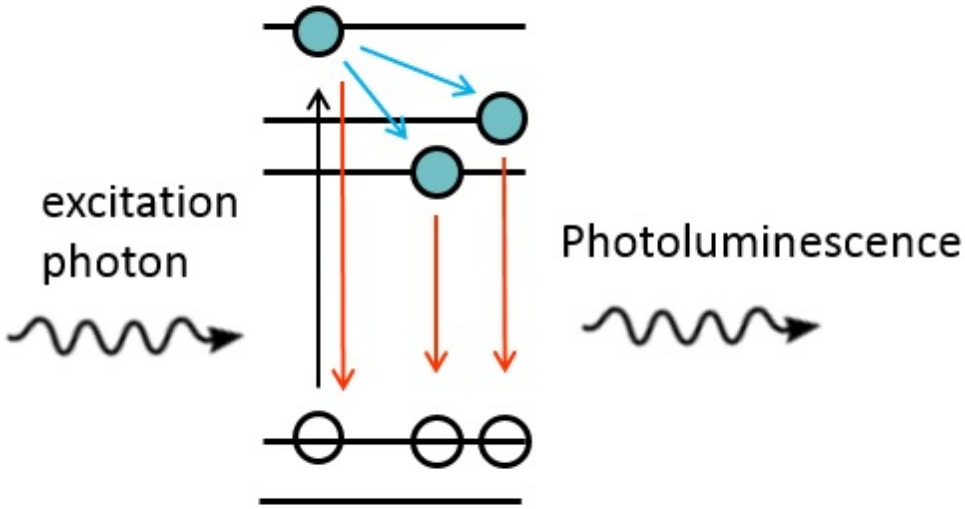

Figure 3.4: Excitation, cooling, and optical transitions involved in photoluminescence in GQDs

uPL measurement data from C132 are shown in Figure 3.5 with a pump fluence of 4.2 mJ cm^{-2} per pulse. The dynamics data are normalized by the long-delay signals $PL(t =$

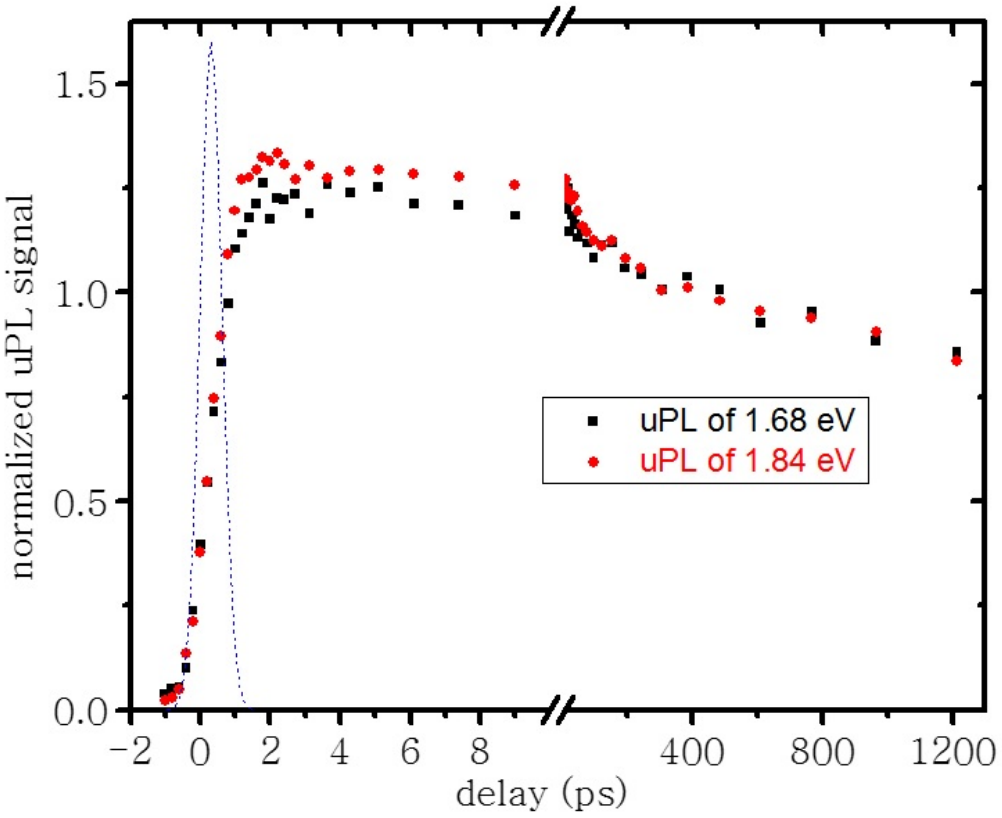

Figure 3.5: Normalized dynamic data of C132 pumped at 3.1 eV and probed at 1.68 eV and 1.84 eV

$100 - 1000$ ps) of each trace. The small difference between the probe signals at 1.68 eV and 1.84 eV only exists for the first few ps, while the instrument response time is ∼2 ps shown in Figure 3.5. As discussed in Chapter 1, we were not able to completely separate these two peaks (670 nm and 750 nm) from each other in our measurement with the needed temporal resolution, and it is possible that the emission we measure in our uPL is from impurities [11].

Considering both C132 and C168 have low photoluminescence quantum yields (less than 2% and 0.2% respectively), impurity emission may be the dominant feature in such case. In TA measurements, we can choose the probe energy to focus on GQD transitions with greater oscillator strength so that the impurities have less impact on the data.

3.2 Experiment and results

3.2.1 Experimental setup

The experimental femtosecond TA setup was described in Chapter 2. C168 in toluene was excited at 3.1 eV and probed with ∼130 fs temporal resolution using either a broadband continuum (for photon energies $\hbar\omega_{\text{probe}} \geq$1.1 eV) or the output of a BBO-based OPA (for 0.5 eV $\leq \hbar\omega_{\text{probe}} \leq$ 1.05 eV). The former was measured with a CCD spectrometer with 2 nm spectral resolution, while the latter was measured with a monochromator and InGaAs photodiode with 5 nm spectral resolution.

3.2.2 Experimental results and discussion

Figure 3.6 shows a typical delay-dependent transient absorption spectrum obtained with a CCD detector when exciting C168 at 3.1 eV with a pump fluence of 0.79 mJ cm^{-2} per pulse. There is little to no change in the shape of the absorption spectrum after the first ∼10 ps. After that time, the main change in the spectrum is a decrease in amplitude, which we attribute to the residual cooling of the lattice. For probing the BX electronic structure, we focus on long delays, when the system has unquestionably cooled to the lowest-energy singlet exciton states.

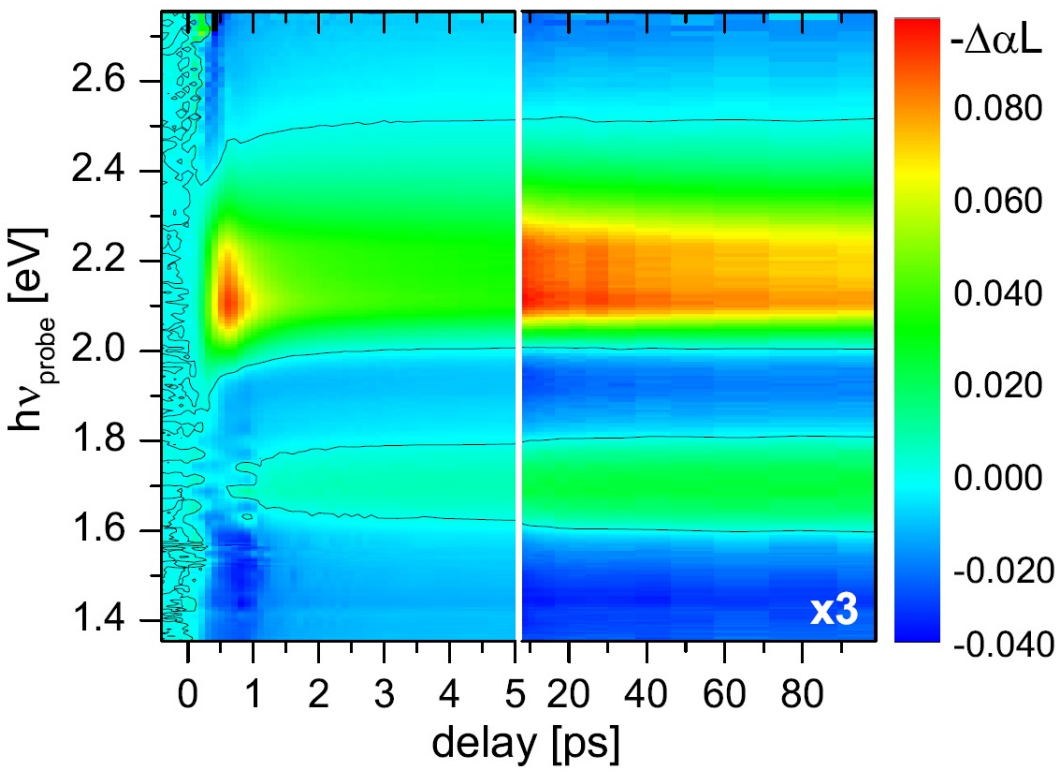

Figure 3.6: $-\Delta\alpha L$ as a function of wavelength and delay for C168 excited at 3.1 eV at an intensity corresponding to $< N_{\text{abs}} > \sim 1.2$. The scale corresponds to the data at delays t$\leq$5.0 ps. The data in the right panel (t $>$ 8 ps) are multiplied by 3. The black curves indicate the $\Delta\alpha L = 0$ contours [14].

For interpreting the experimental data at long delays, we focus on the band-edge biexcitons. High-energy excitons will relax to lower-energy excitons so that only $X_{1,2}$ is left at long delays. The calculated singlet excitons and biexcitons in Figure 3.1(B) can be classified by examining whether the single-exciton states from which they are primarily derived include two (XX_{1-3}), one (XX_{4-7}), or zero (XX_{8-10}) LX excitons. Following the Δm= $\pm$1 selection rule, the allowed transitions (solid blue arrows) are indicated in Figure 3.1(B). The biexciton binding energy is the difference between the biexciton energy, E_{XX_i}, and the sum of the energies of single-excitons (X_j and X_k) that primarily form the biexciton: $\Delta_{XX_i} = (E_{X_j} + E_{X_k}) - E_{XX_i}$. When there is a positive binding energy (as in our sample), biexciton binding causes the the energy of transitions from a single-exciton state to biexciton

state to be lower than that from the ground state to the exciton state corresponding to the second exciton added to form the biexciton. The theoretical calculation described above yields $\Delta_{XX_{1-3}}$=56-82 meV, $\Delta_{XX_{4,5}}$=142 meV and $\Delta_{XX_{6,7}}$=104 meV.

Data for t = 100 ps in Figure 3.6 are shown by blue circles in Figure 3.7. Bleaches of the ground-state transitions (∼1.7 and 2.1 eV) are accompanied by induced absorption immediately to the red (∼1.45 and 1.95 eV). Such patterns are characteristic signatures in TA of biexciton binding [106]. Measurements under the same conditions but at lower probe energies (0.5 eV to 1.1 eV) are used to probe intraband transitions, which are also illustrated in Figure 3.7.

The population of $X_{1,2}$ opens new transitions $X_{1,2} \rightarrow XX_{X_{1,2}+X_n}$, which requires less energy than the $0 \rightarrow X_n$ transition because of the biexciton binding. However, induced absorption (IA) below 1 eV provides clear evidence of intraband transitions. This raises the possibility that such transitions may contribute to our TA signal in the visible region (1.3 to 2.5 eV)as well.

In the biexciton binding measurements, we used high intensity so that essentially all the probed GQDs are excited. For those GQDs that are excited, there are three different contributions to the TA spectrum. Each transition is bleached differently because of their different degeneracies and occupations. This effect is illustrated in Figure 3.9a. When an electron occupies an excited state, the transition probability decreases due to state filling. Because of the two-fold orbitally degenerate HOMO and LUMO, the $0 \rightarrow X_i$ transition can occur from either of two available states in the valence band. Accounting for the different two spins associated with each orbital state, we have 4 possible transitions as shown on the left of Figure 3.8. After excitation, one state of conduction band has been occupied which leaves only 2 possible transitions as shown on the right side of Figure 3.8. As a

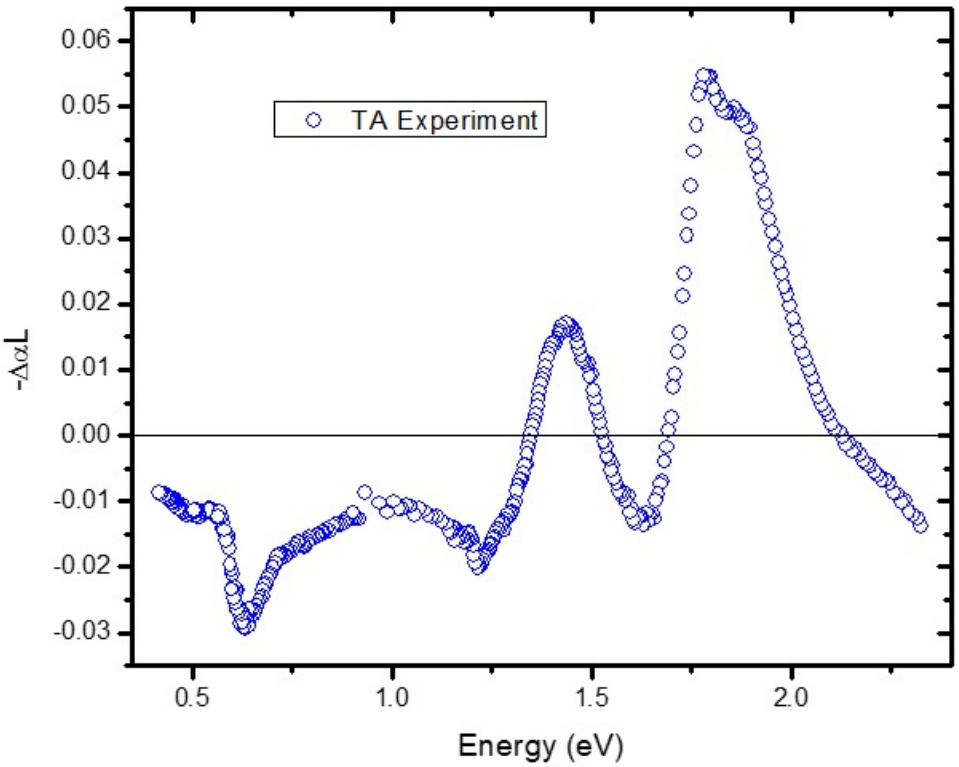

Figure 3.7: $-\Delta\alpha L$ at delay t = 100 ps for C168 at $< N_{\text{abs}} > = 1.2$ and $\hbar\omega_{\text{pump}} = 3.1$ eV with TA spectrum of intraband transitions.

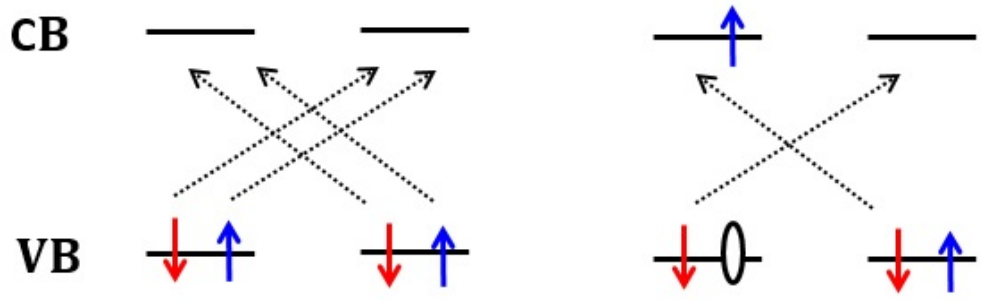

Figure 3.8: Possible transitions of giving rise to X_3 and X_4 (left) and $X_{1,2} \rightarrow X_{1,2} + X_{3,4}$ i.e., $X_{1,2} \rightarrow XX_{4-7}$ (right) showing the effects of state filling on the transitions to the lowest bright singlet excitons

result, the probability of the $X_{1,2} \rightarrow X_{1,2}+X_i$ transition is 1/2 that of the $0 \rightarrow X_i$ transition in the single-particle picture (the ratio may be different when including correlations). The spectrum is shifted as illustrated in Figure 3.9b because of biexciton binding. We start our model from a fit of 5 Gaussian peaks to the ground-state absorption spectrum as illustrated in Figure 3.9a in red. The green curve in Figure 3.9c shows the modeled spectrum with all three contributions to the TA spectrum considered. The difference between the ground-and excited-state absorption spectra yields the TA spectrum. The fitting of the experimental data is illustrated in Figure 3.9d by the solid blue curve. There is a slight mismatch at the peak, but all the characteristics of the TA spectrum are fitted well.

To clarify our interpretation of the experimental TA spectrum, Isil Ozfidan calculated the spectrum $\alpha_{LX} - \alpha_0$, which is shown by the black curve (50 mV gaussian broadening added) in Figure 3.10. Induced absorption at $\sim$1.95 eV is primarily caused by $X_{1,2} \rightarrow XX_{4-7}$. Because of the orbitally forbidden nature of the transition $X_{1,2} \rightarrow XX_{1-3}$, there is no similar feature

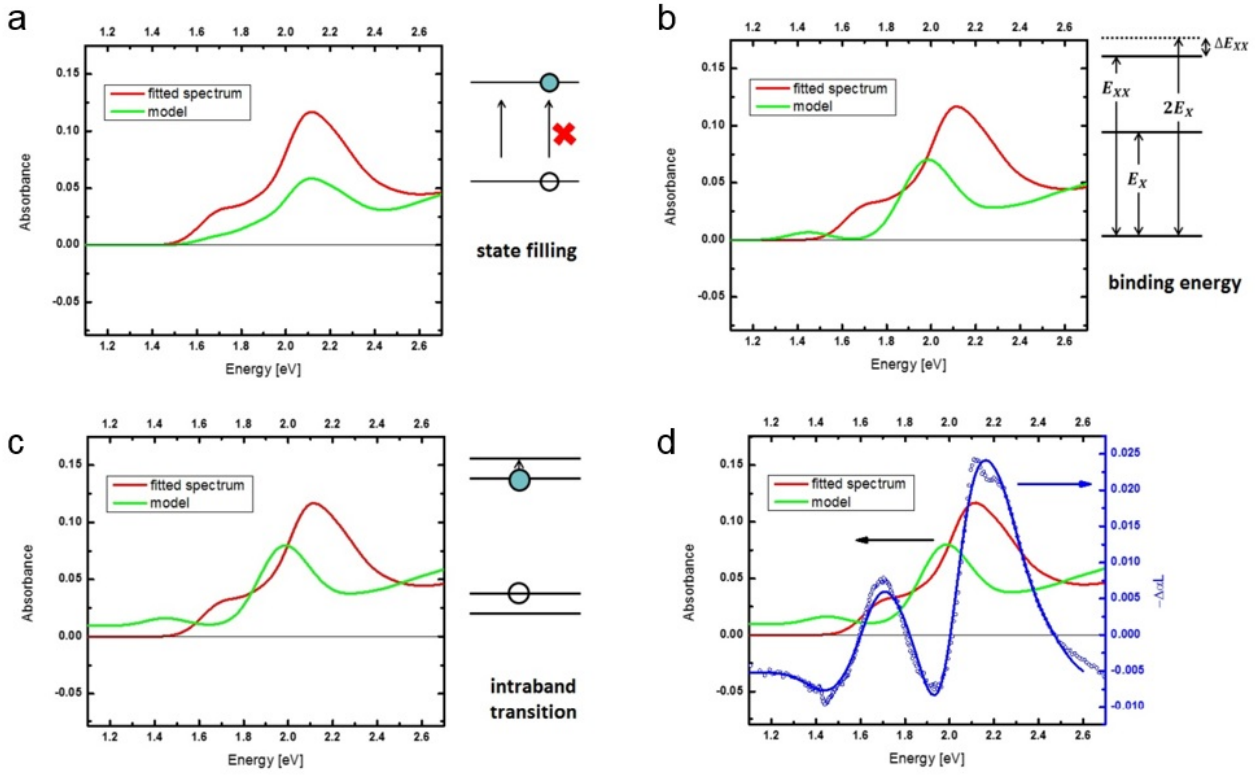

Figure 3.9: Step by step analysis of different contributions on -$\Delta\alpha L$ in TA measurement, right side of each spectrum illustrate the different contribution to the absorption spectrum

in the calculated spectrum near the 1.7 eV peak. Calculated induced absorption at 0.65 eV, 1.0 eV and 1.35 eV roughly match the features seen in the experiment at 0.6 eV, 0.75 eV and 1.45 eV and further suggest that caution should be exercised in interpreting the 1.45 eV feature in the experimental spectrum as a signature of bound biexcitons X_{1-3}.

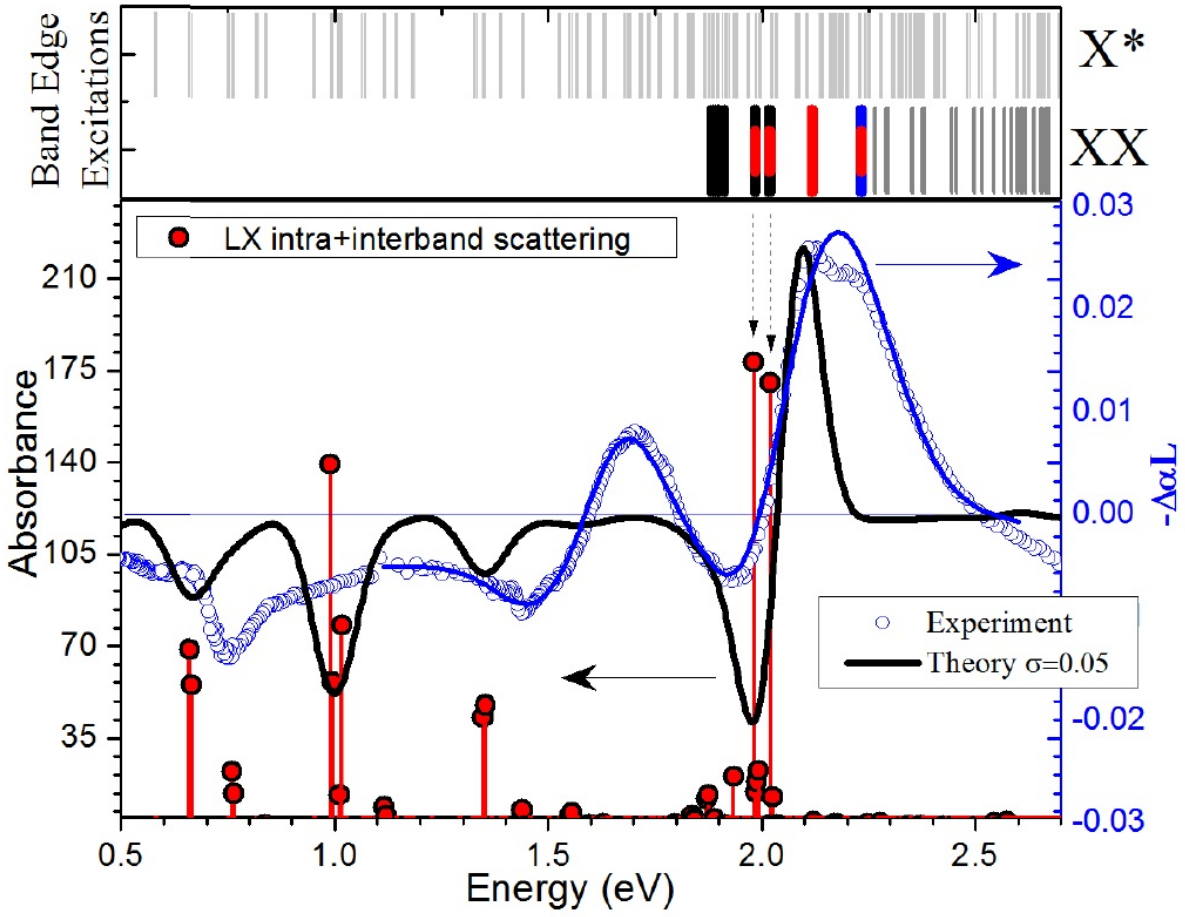

Figure 3.10: Experimental and theoretical absorption spectra from the lowest singlet exciton state. Blue circles indicate measured $-\Delta\alpha L$(t=100ps) of C168. The red bars indicate calculated transitions from the states $X_{1,2}$ accounting for intra+interband transitions. The black line is the theoretically calculated, Gaussian broadened $-\Delta\alpha = -(\alpha_{1,2} - \alpha_0)$ assuming equally populated $X_{1,2}$ states. Top panel shows singlet excitons (light grey), band-edge excitons (color corresponding to Figure 3.3) and higher XXs (dark grey) accessible from $X_{1,2}$ [14].

To quantitatively determine the biexciton binding energies of XX_{4-7}, a fitting routine was written with Mathematica. We model the TA spectrum as follows. The energies of the ground-state optical transitions are determined by the positions of the peaks of $-[(d^2\alpha_0)/(d(h\nu)^2)]$ [110] as illustrated by the blue line in Figure 3.11 Such a derivative

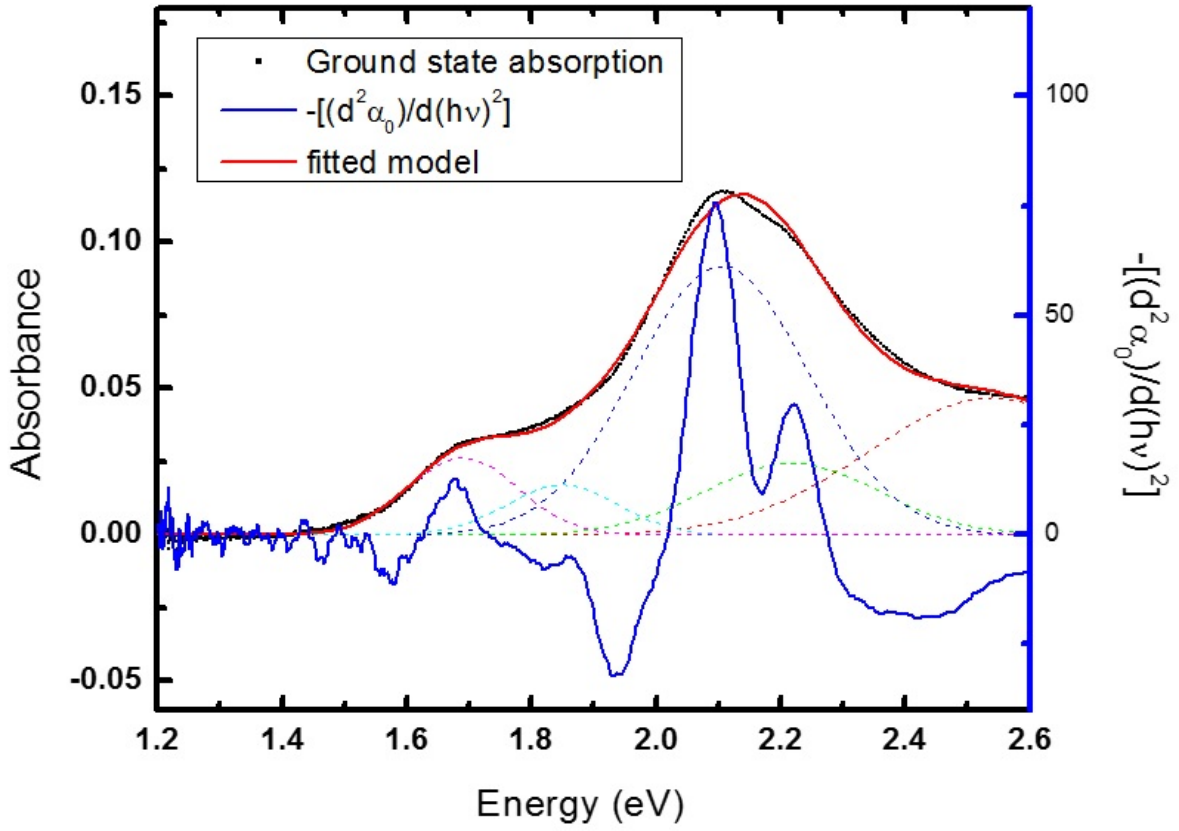

Figure 3.11: Ground state absorption is plotted in black dots and the fitted model is presented in red line. The peaks of $-[(d^2\alpha_0)/(d(h\nu)^2)]$ indicates available transitions, which are shown by dashed line in the figure.

yields two features in the low energy shoulder, one at 1.68 eV and a smaller one at 1.86 eV, corresponding to $X_{1,2}$, which is optically brightened by coupling to phonons [11]; two in the

peak around 2.1 eV, one at 2.09 eV and another of about half the amplitude at 2.22 eV, corresponding to $X_{3,4}$; and another around 2.6 eV, corresponding to excitons that are not derived from a transition between the HOMO and LUMO states.

The spectral widths of the X→XX and 0→X transitions are set as equal since the main source of additional broadening of $X_{1,2}$ →XX_{4-7} relative to 0→$X_{3,4}$ is expected to be biexciton Auger recombination, where $\tau_{XX} = 0.3$ ps [111]. The amplitude of the bleach (β_{X_i}) of each transition 0→X_i and the binding of the two pairs of optically bright ($\Delta m = \pm 1$) XX are set as fitting parameters. To minimize the number of free parameters, we use a common value of the biexciton binding (Δ_{1-3}) for XX_{1-3} and (Δ_{4-7}) for XX_{4-7} so that the fit yields an average binding energy for each set of states. The fitting function can be written as:

$$-\Delta\alpha(\omega)L = \delta\alpha L + \sum_{i=1}^{4} \beta_{X_i}[g_{X_i}(\omega) - R_i g_{X_i}(\omega + \Delta_i)] \tag{3.2}$$

where $\delta\alpha L$ represents a spectrally flat induced absorption taken as -0.05, $g_{X_i}(\omega)$ are gaussians taken from the fit to the ground-state absorption spectrum, β_{X_i} represents the bleach of each transition and R_i is the ratio of the oscillator strength of the $X_{1,2}$ →$X_{1,2}$+X_i transition to the 0→X_i transition. We assume that $\beta_{X_1} = \beta_{X_2}$ and $\beta_{X_3} = \beta_{X_4}$. A best fit of the TA spectrum in the spectral ranging from 1.5 to 2.4 eV is shown by the solid blue curve in Figure 3.10 with $\Delta_{XX_{1-3}} = 280\pm30$ meV and $\Delta_{XX_{4-7}} = 140\pm10$ meV. We constrain R_3 to 0.59 maximum in the fitting because Isil's calculations yield 0.43 and 0.59 for the transitions to the two sets of biexcitons in this range. The fit yields $R_1 = 0.22 \pm 0.01$ and $R_3 = 0.59 \pm 0.01$. The value of R_3 is consistent with the value of 1/2 expected from state-filling in a single-particle picture as discussed above.

To confirm the origin of the spectral features in the experimental TA spectrum shown in Figure 3.10, our collaborator calculate the TA spectrum $-(\alpha_{\mathrm{LX}}(\omega) - \alpha_0(\omega))$ shown by the blue curve. The transition GS$\rightarrow$ $\mathrm{X}_{3,4}$ gives rise to the peak in the TA spectrum at 2.1 eV. The TA spectrum also involves optical transitions from the photoexcited state to excited exciton, X^*, and biexciton, XX, states shown by grey and black lines in the top panel of Figure 3.10 and yielding $-\alpha_{\mathrm{LX}}(\omega)$. In particular, the dip at 1.95 eV is due to $\mathrm{X}_1 \rightarrow \mathrm{XX}_{6-7}$ and $\mathrm{X}_2 \rightarrow \mathrm{XX}_{4-5}$ transitions that involve addition of a bright $\mathrm{X}_{3,4}$ exciton to the photoexcited LX. This supports the interpretation of the experimental feature at this energy as due to a single-to-biexciton transition. The lower panel of Figure 3.10 shows negative TA contributions at energies $E < 1.5$ eV, well below the XX transitions, due to intraband excitations of photoexcited electrons and holes from LX to excited exciton states X^*. While the calculated and measured energy ranges of the X^* contribution are in qualitative agreement, the broadening of the experimental spectra prevents detailed comparison of energies of excited exciton states X^*. The positive contribution to the experimental TA spectrum in Figure 3.10 at 1.7 eV corresponds to absorption to dark exciton states that are prohibited in the calculated spectra, which do not account for electron-phonon coupling.

Compared to C168, C132 misses a corner of the triangular shape so it is less symmetric. Our collaborators did not calculated the biexciton electronic structure of C132. Experimentally, we apply the same TA measurements mentioned above to C132. The TA spectrum of C132 from 0.4 eV to 2.3 eV is shown in Figure 3.12. On the high energy end of the TA spectrum, the oscillation pattern indicates the presence of biexcitons between 1.7 and 2.0 eV. We tried to fit the experimental TA spectrum of C132 similarly as we did with C168, and got a biexciton biding energy of 0.20 meV at the main peak. With more peaks (transitions) involved, the ground state spectrum and TA spectrum of C132 have more structure than

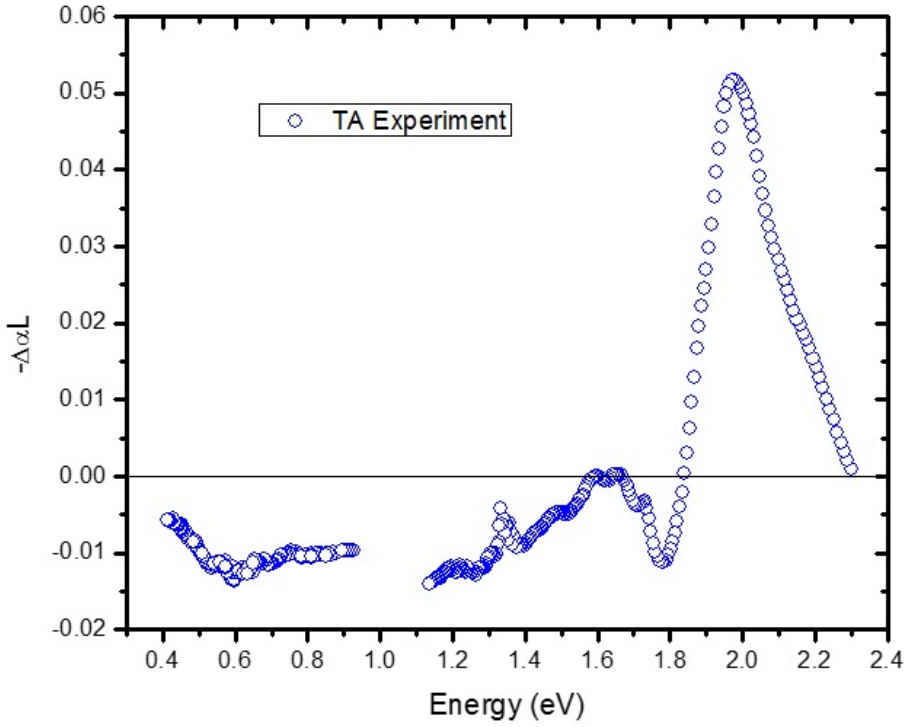

Figure 3.12: $-\Delta\alpha L$ at delay t = 100 ps for C132 at $< N_{\text{abs}} > = 1.2$ and $\hbar\omega_{\text{pump}} = 3.1$ eV with TA spectrum of intraband transitions

those of C168, which makes the interpretation of experimental data more tenuous than in the case of C168.

3.3 Conclusion

These experiments and theories demonstrate the interaction of excitons in graphene quantum dots. The degeneracy of HOMO and LUMO states leads to a pair of bright singlet excitons and orbitally dark singlet excitons and a corresponding band of strongly correlated biexciton states. For C168, the exciton-exciton interaction lowers the energy of the XX_{4-7} biexcitons, with values exceeding the binding energy of the lowest-energy XX (105 meV) measured in (9,7) single-wall carbon nanotubes [109]. The strong interaction between carriers and rapid biexciton Auger recombination [111] suggest that GQDs could be efficient materials for carrier multiplication. This allow generation of multiple carriers occurring before excess carrier energy is lost, which could be useful in photovoltaic. Such multiple-carrier generation could makes it possible for the efficiency of a solar cell to exceed the Shockley-Queisser limit. The strong binding of higher biexciton states demonstrated in our study highlights the central role of many-body effects in reduced-dimensional materials. As stated above, the less symmetric C132 has not yet been well studied theoretically. Further study on C132 may help us better understand how structure and symmetry affect the exciton and biexciton binding in these quantum confined systems.

Chapter 4

Biexciton Auger recombination

In this Chapter, TA measurements of Auger recombination are discussed in detail. The study of this nonradioactive recombination helps us better understand the biexciton behavior in GQDs and may provide more information when GQDs are used as materials in photovoltaics.

4.1 Carrier relaxation in quantum confined system

When carriers in quantum dots or other quantum confined system are excited by high-energy photons, they relax by various mechanisms. One of the mechanisms is phonon emission. Such relaxation in, for example, PbSe and CdSe quantum dots, is usually fast (subpicosecond) [112, 113, 114]. When the highest energy phonon has lower energy than the difference between quantized energy levels, phonon emission is possible only by simultaneous emission of multiple phonons. The slowing of cooling when simultaneous emission of multiple phonons is required is known as the phonon bottleneck [115, 116]. After optical excitation, carriers are in a nonthermal distribution that then thermalizes in 10 - 150 fs [16]. This is followed by intraband carrier-phonon scattering between 150 fs and 1 ps. After 1 ps, electrons and holes recombine until the equilibrium distribution is restored as illustrated in Figure 4.1. People have done experimental studies on ultrafast relaxation dynamics in graphene [16, 117, 118, 119, 120]. Among them, Winnerl et al. excited epitaxial graphene

with different excitation energies [120]. An Optical-phonon bottleneck is observed in the excitation range from 30 - 245 meV. Carrier relaxation becomes slower when the excitation energy is below the optical-phonon energy.

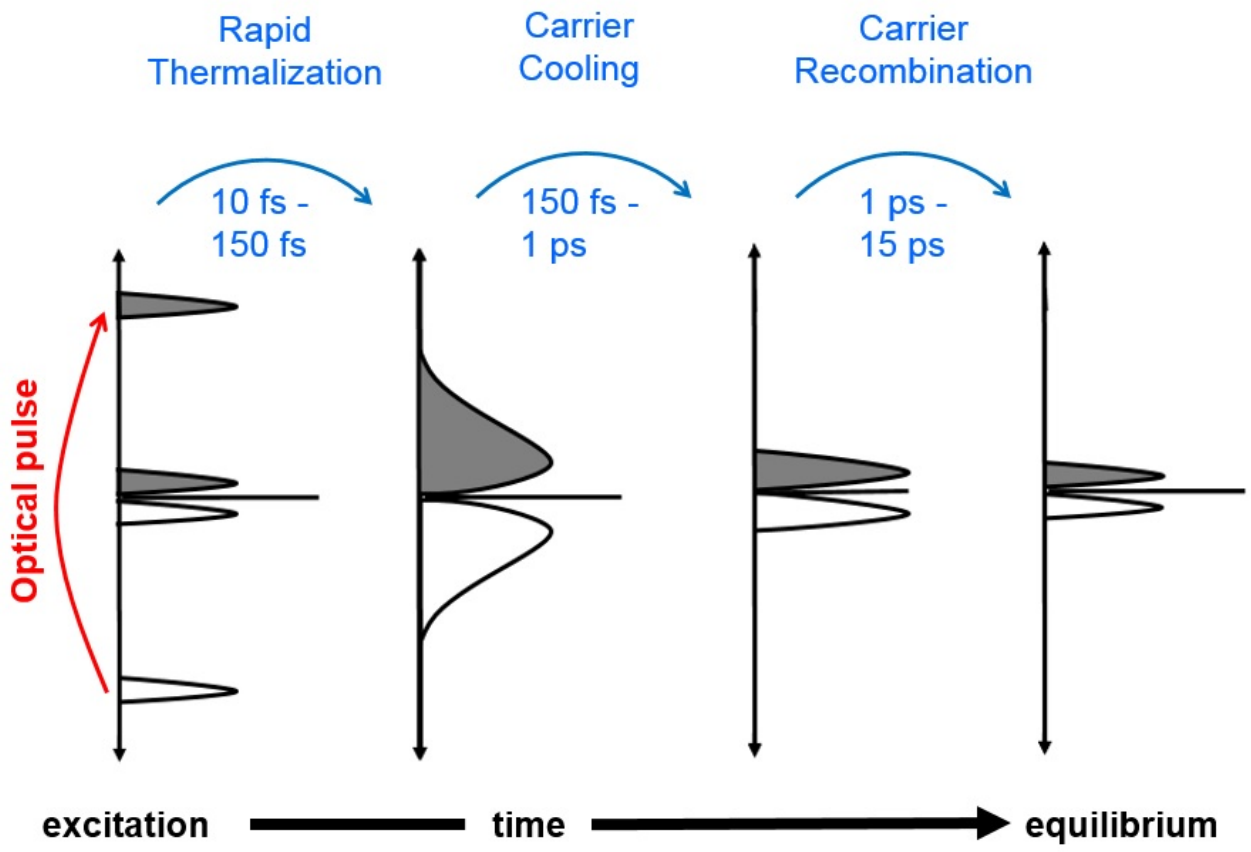

Figure 4.1: A schematic of the processes by which optically excited electron and hole distributions approach equilibrium in epitaxial graphene. Distribution at the time of excitation near the Dirac point shows an intrinsic thermal population of electrons and holes. (Reproduced from Ref. [16]).

Besides phonon-assisted process, electron and holes can recombine and give their energy to a third carrier, which is Auger recombination (AR) (illustrated as carrier cooling in Figure 4.1). Auger recombination can be significantly different in quantum confined systems

than in bulk. Relaxation of crystal momentum conservation in nanoscale lattices [86, 121] can lead to rapid AR of multi-excitons [75, 122]. In bulk semiconductors, the rate of AR is significantly different between direct-gap and indirect-gap materials. In direct-gap materials, AR is a three-carrier process while in indirect-gap materials, AR is a four-particle process involving three carriers and emission (or absorption) of a momentum conserving phonon [123]. The truncation of the periodic lattice in nanocrystal leads to relaxation of translational momentum conservation [86]. In CdSe nanocrystal quantum dots, the BX AR lifetime decreases from $\sim$ 1 ns to less than 10 ps as the nanocrystal radius decreases from 5 to $\sim$ 1 nm [75]. In single-walled carbon nanotubes (SWCNTs) with diameters of $\sim$ 1 nm and lengths of $\sim$ 400-500 nm, the exciton-exciton annihilation time is only of the order of 1 ps [85, 109, 124]. Because our GQDs have similar size as the circumference of common SWCNTs but are only one atom thick, the BX AR lifetime in GQDs about 2 nm in spatial extent might then be expected to be much shorter than 0.1 ps.

4.2 Experiment and data analysis

4.2.1 Experimental setup

uPL measurements were performed as describe earlier. As illustrated in Figure 3.5, after the first few ps, there is barely any difference between these two traces. In addition, two relatively slow decays can be observed ($\sim$10 ps and $\sim$280 ps) during this process as well. We attribute the cooling of hot carriers within less than 2 ps to carrier-phonon scattering. This 2 ps window might only be an upper limit because it's approaching the limit of our instrument response time (around 1 ps).

We applied the TA measurements described in Chapter 2 to explore the dynamics of

GQDs. The TA instrument response is $\sim$ 130 fs. Residual dispersion across the probe spectrum was determined by acquiring TA spectra in a BBO crystal placed at the sample position. To account for the solvent response, identical measurements were performed on a cuvette filled with the solvent alone. The result was subtracted from the data for the GQD solution. Measurements on samples in which the solution was stirred to remove GQDs from the excitation volume between laser pulses showed no difference in dynamics from static solutions, indicating that photochemical processes such as the generation of long-lived charge-separated states did not distort the results. We focused on pump excitation with the lowest photon energies since the low-fluence dynamics of the main absorption peak are flattest when exciting low-energy carriers, making interpretation and analysis more straightforward.

4.2.2 Data analysis

The pump-induced sample response is reported as $-\Delta\alpha L$, where $-\Delta\alpha$ is the change in absorption coefficient and L is the sample length. As described in Chapter 2, we used the CCD to measure TA in the visible region of the spectrum. Raw data from the CCD has a wavelength step of 0.3 nm while the resolution of the spectrometer is 2 nm. In this case, we wrote a Labview program to average data in 2 nm bins. The data from excitation of C132 at $\hbar\omega_{\text{pump}} = 1.94$ eV are plotted in Figure 4.2(a) and 4.2(b) for pump fluences in the multiple- and single-photon absorption regimes respectively. For further analysis,, we focus on the large bleach around the main peak in the ground-state absorption spectrum where the signal-to-noise ratio is the highest. Bleaching at energies above $\hbar\omega_{\text{pump}}$ is a consequence of ground-state depletion. Figure 4.3 shows the evolution of $-\Delta\alpha L$ up to 100 ps in C132 at $\hbar\omega_{\text{pump}} = 2.34$ eV at different excitation fluences. Each trace is normalized by the signal at the longest delay shown in Figure 4.4 to weight low-and high-fluence data equally. To

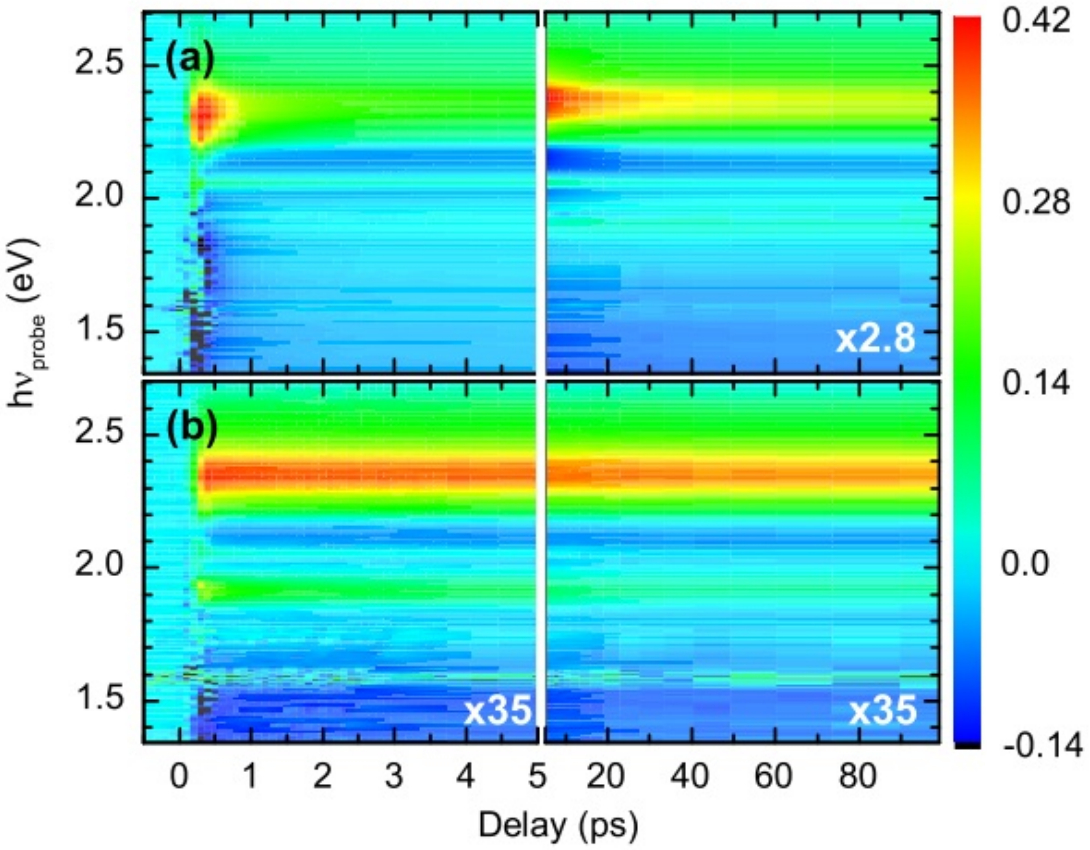

Figure 4.2: $-\Delta\alpha L$ as a function of probe energy and delay for C132 pumped at 1.94 eV and fluences of (a) 1.3×10^{16} and (b) 1.4×10^{14} photons cm^{-2}per pulse. The color scale corresponds to the data for t $\leq$ 5.0 ps in (a). The data in the other three quadrants are multiplied by the factors shown to match the scales.

highlight the relaxation dynamics, we subtracted the normalized signal at the longest delay and present these in Figure 4.3. The dynamics of the lowest-fluence traces (dark yellow and magenta legends in Figure 4.4) are identical in shape within the uncertainty of the measurements. This is expected in the linear excitation regime. When absorption of more than one photon per GQD per pulse can be neglected, the dynamics only reflect single-exciton dynamics. At low fluences, the signal decays by a total of 20% with an initial decay of several percents on a time scale of the order of 0.1 ps followed by sub-10% decays on time scales of a few ps and tens of ps. We attribute these dynamics to cooling within the

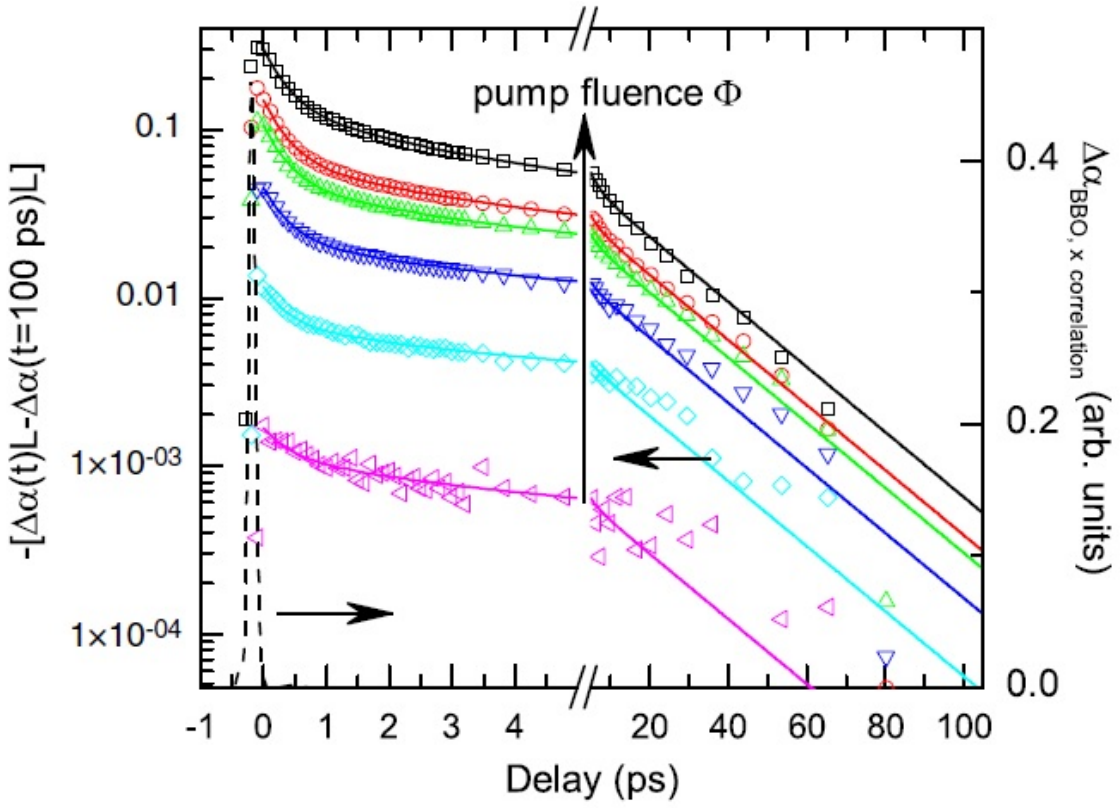

Figure 4.3: $-\Delta\alpha(\Phi, t)L$ versus probe delay for C132 pumped at 1.94 eV and probed at 2.34 eV. Solid curves are the fits described in the text. The dashed curve represents the instrument response function.

low-energy vibronic manifold and solvation dynamics.

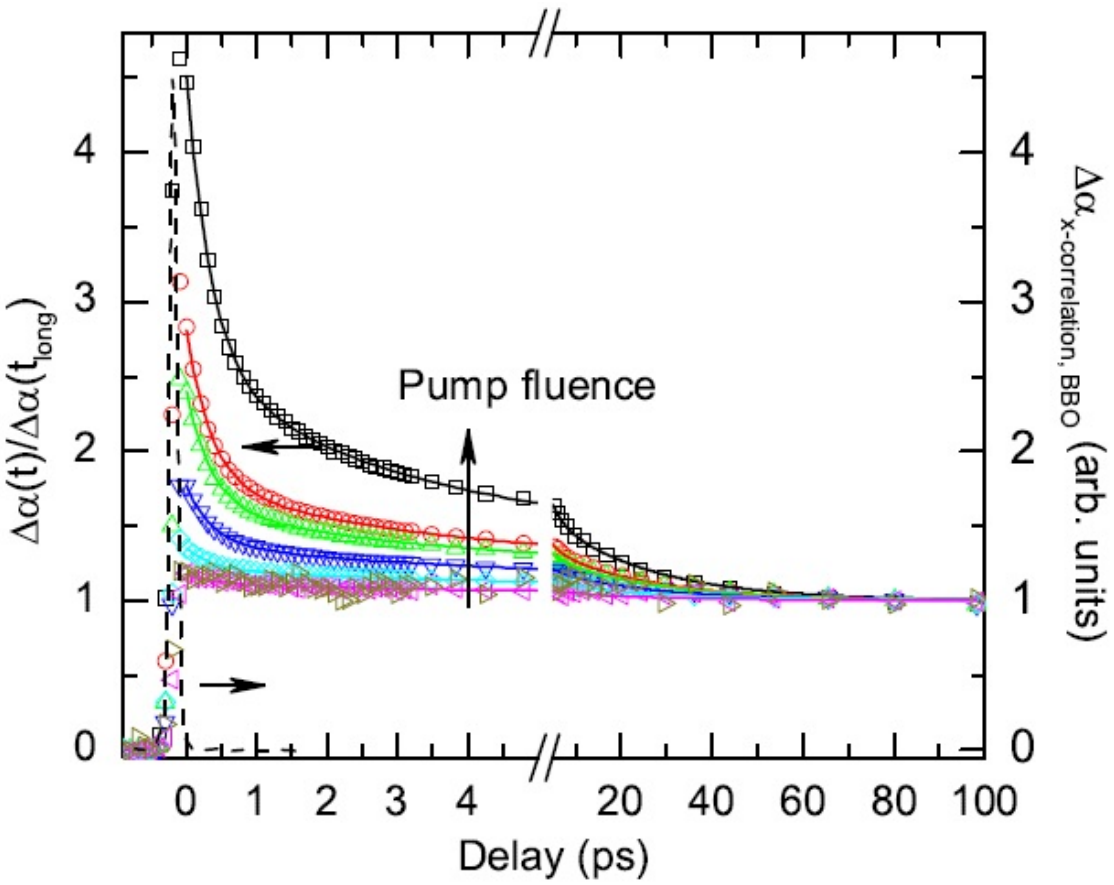

Figure 4.4: $\Delta\alpha(t)/\Delta\alpha(t_{\mathrm{long}})$ versus probe delay for C132 in toluene excited at $\hbar\omega_{\mathrm{pump}} = 1.94$ eV and probed at $\hbar\omega_{\mathrm{probe}} = 2.34\,\mathrm{eV}$.

As the excitation fluence Φ increases, new dynamics emerge. Specifically, the amplitude of the subpicosecond decay increases by more than 2 orders of magnitude while the long-delay signal increases by only a factor of 9. We analyzed the data presented in Figure 4.4 by a global fit with a triexponential form:

$$-\Delta\alpha(\Phi,t)L = A_f(\Phi)e^{-t/\tau f} + A_{s1}(\Phi)e^{-t/\tau s1} + A_{s2}(\Phi)e^{-t/\tau s2} + A_0(\Phi) \qquad (4.1)$$

The triexponential fit is executed in Origin with its built-in fitting function. To perform a

global fit on our data, we shared time constants (τ_f,τ_{s1} and τ_{s2}) across all traces of the fitting. This fit yields the time constants $\tau_f = 0.34 \pm 0.01$ ps, $\tau_{s1} = 2.5 \pm 0.1$ ps, $\tau_{s2} = 22 \pm 1$ ps and the amplitudes plotted in Figure 4.5 (all reported uncertainties are the standard errors of the fits). According to studies of other strongly confined nanoscale systems, at long delays, multi-excitons can recombine and only single excitons remain[75, 85, 124]. Hence, A_0 should be well fit by the Poisson probability for absorption of at least one pump photon:

$$A_0(\Phi) = A_{0,sat} \sum_{n=1,2,...}^{\infty} P_n(\sigma_0 \Phi) = A_{0,sat}[1 - P_{n=0}(\sigma_0 \Phi)] = A_{0,sat}(1 - e^{-\sigma_0 \Phi}) \qquad (4.2)$$

where $A_{0,sat}$ is the saturated single-exciton response at 100 ps, $P_n(\sigma_0\Phi)$ is the Poisson probability for absorbing n photons given an average number of absorbed photons per GQD per pulse of $\bar{n} = \sigma_0\Phi$, and σ_0 is the effective GQD absorption cross section at the pump wavelength. The fit of $A_0(\Phi)$ (solid black curve in Figure 4.5) implies an effective $\sigma_0(\hbar\omega =$ 1.94 eV) of 7.4×10^{-16} cm^2. This is different from the value reported by Xin et al. [8], which is 9.9×10^{-17} cm^2. We can estimate the cross section of GQDs from the area of the lattice. The longest length of C168 is 2.4 nm, according to which we calculated the area of the triangular-shape C168 is 2.49×10^{-14} cm^2. Since the area of C132 is 3/4 of C168, using the same formula, we get the result of 1.87×10^{-14} cm^2 for the area of C132. At 4.1 eV, where quantum confinement effects are less pronounced, the absorption of graphene is $\sim 7\%$ [125]. Considering our experiment uses a linearly polarized pump to excite the GQDs and our GQDs are oriented randomly in solution, 1/3 of our dots are oriented with their two-dimensional lattice perpendicular to the polarization of the pump and so are not excited in the TA measurement. So the effective σ_0 of C132 at 4.1 eV is expected to be 1.87×10^{-14} cm$^2 \times 0.07 \times \frac{2}{3} = 8.7 \times 10^{-16}$ cm^2. From the ground-state absorption spectrum in Figure

1.8, the ratio of the cross section of C132 at 1.94 eV to that at 4.1 eV is ~ 0.31 to 0.05, so σ_0 of C132 at 1.94 eV is expected to be 8.7×10^{-16} cm^2 $\times \frac{0.05}{0.31} = \times 10^{-16}$ cm^2, which is close to our fitting result.

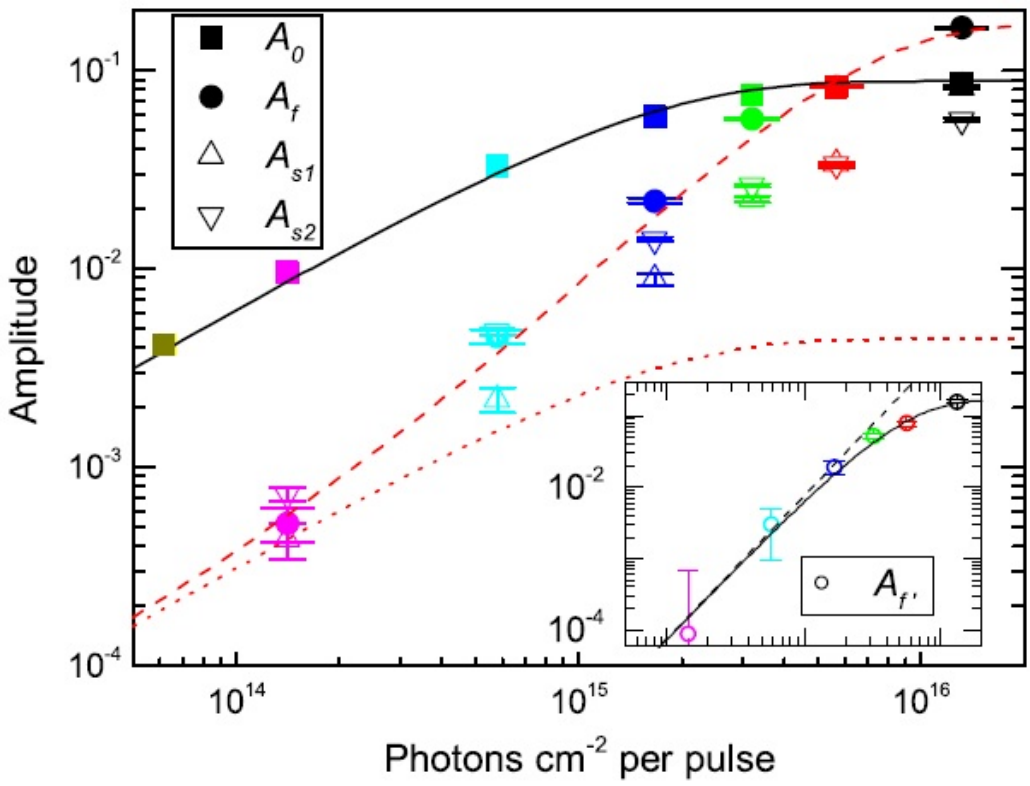

Figure 4.5: Amplitudes A_i from Eq. 4.1 describing the fits of $-\Delta\alpha(\Phi, t)L$ of C132 in Figure 4.3. The inset shows the quantity $A_{f'}$ defined in the text and associated with multiexcitons and uses the horizontal scale of the main figure. Curves show the fits described in the text.

$A_0\Phi$ is linear at low fluences in Figure 4.5, and at $\Phi \leq 3 \times 10^{15}$ photons cm^{-2} per pulse, the amplitude of the fastest decay term (A_f), is superlinear. This is a characteristic of multi-exciton AR. A_f will then have contributions from both single- and multi-excitons and can be characterized by the form:

$$A_f = A_{f,X}[1 - P_0(\sigma_0\Phi)] + A_{f,MX}P_{>1}(\sigma'\Phi) \tag{4.3}$$

where σ' is the absorption cross section of GQDs after absorption of one photon; $A_{f,X}$ is associated with the small-amplitude decay of single excitons seen most clearly at low fluences as described earlier; and $A_{f,MX}$ is associated with relaxation of multiexcitons. The dashed red curve in Figure 4.5 shows a fit of A_f by Eq. 4.3 with $A_{f,X}$, $A_{f,MX}$, and σ' as fitting parameters and σ_0 fixed by the earlier fit of A_0. The best fit yields $\sigma' = (0.41 \pm 0.07)\sigma_0$. Because of the two-fold degeneracy of the HOMO and LUMO, the strength of the transition should be reduced by half (in a single-particle picture) when an electron-hole pair is created at the band edge. Our fitting result matches the expected value of 0.5. The contribution of the $A_{f,X}$ term to A_f is illustrated by the red dotted curve and is seen to be much less than the multi-exciton contribution at $\Phi > 5 \times 10^{14}$ photons cm^{-2} per pulse. The multi-exciton contribution to the fast decay is highlighted by the inset of Figure 4.5, where we plot the points $A_{f'} = A_f - A_{f,X}[1 - P_0(\sigma_0\Phi)]$. The inset also shows the fitted term $A_{f,MX}P_{>1}(\sigma'\Phi)$ (solid curve). The multiphoton fit shows excellent agreement with the data, and as expected for a process associated with absorption of more than one photon, $A_{f'}$ is perfectly aligned with a quadratic scaling with pump fluence (dashed curve in the inset) in the lower fluence range.

To rule out non-Auger processes being responsible for the rapid decay observed at high fluences, we analyzed the data by alternative approaches. One approach is to use the same procedure as described above without normalizing the data. We subtracted $-\Delta\alpha(t = 100\,\text{ps})L$ from the data and performed a global fit of the resulting data to a triexponential form with shared time constants. This weights higher-fluence data more heavily than low-fluence data. For C132, we obtained $\tau_f = 0.34(0.01)\,\text{ps}$, $\tau_{s1} = 2.4(0.1)\,\text{ps}$, and $\tau_{s2} = 22(1)\,\text{ps}$. Another approach is to fit the lowest-fluence data independently, normalize that fit at long delay, and subtract the normalized fit from the normalized data at other fluences. The difference data

are then fit to a triexponential form decaying to zero with global time constants. For C132, this yields $\tau_f = 0.34(0.01)$ ps, $\tau_{s1} = 2.3(0.1)$ ps, and $\tau_{s2} = 18(1)$ ps. The different fitting procedures produce values of the primary timescale of interest, τ_f, differing by only 0.02 ps from the values obtained from the first analysis. In the case of C132, neither τ_{s1} nor τ_{s2} changes substantially.

Similar measurements were performed on C168. Figure 4.6 shows the TA data for C168 at $\hbar\omega_{\text{pump}} = 1.70$ eV (near the absorption edge) with pump fluences in the multiple- and single-photon absorption regimes respectively. Single-wavelength dynamics and fitting are

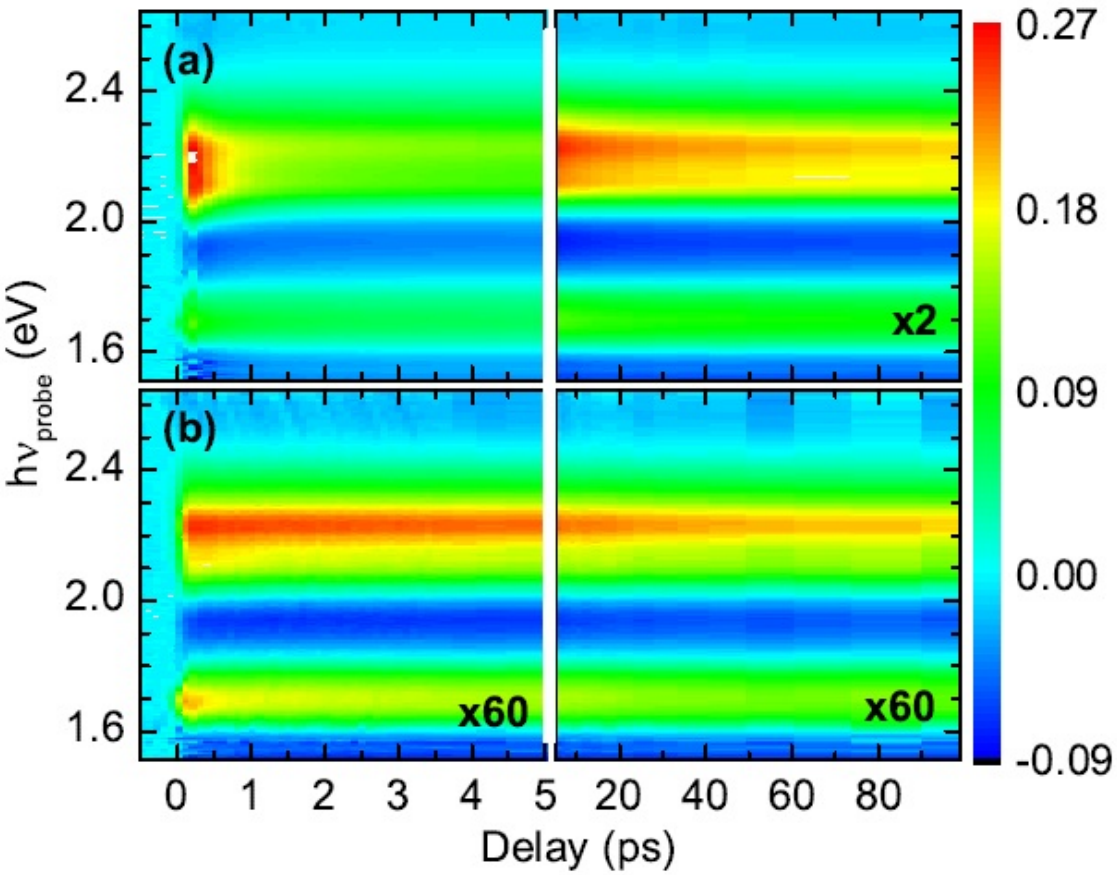

Figure 4.6: $-\Delta\alpha L$ as a function of probe energy and delay for C168 excited at 1.70 eV at fluences of 2.0×10^{15} photons cm^{-2} per pulse (a) and 2.4×10^{13} photons cm^{-2} per pulse (b). The color scale corresponds to the data for t $\leq$ 5.0 ps in panel (a). The data in the other three quadrants are multiplied by the factors shown to match the scales.

plotted in Figure 4.7. The data presented in the plot are analyzed with the same methods

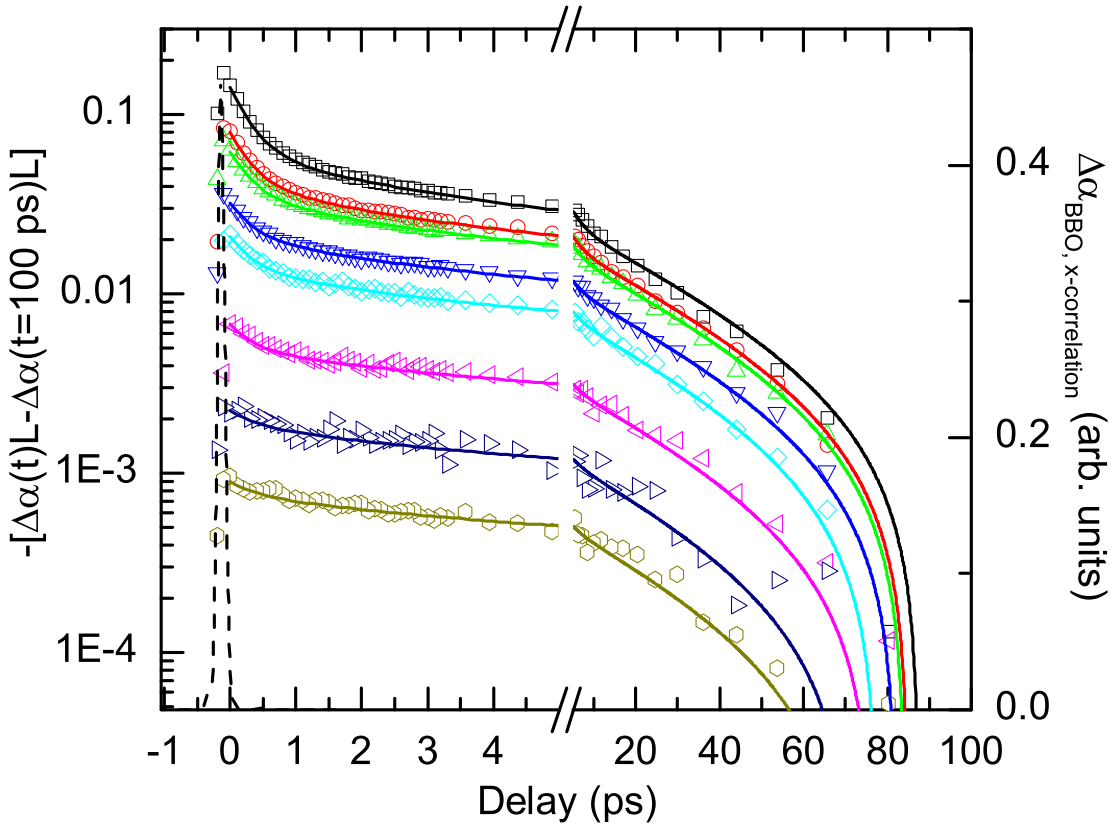

Figure 4.7: (a)$-\Delta\alpha L$ for C168 in toluene excited at $\hbar\omega_{\text{pump}} = 1.70$ eV and probed at $\hbar\omega_{\text{probe}} = 2.21$ eV at a series of excitation fluences from 2.4×10^{13} to 2.0×10^{15} photons cm^{-2} per pulse. Solid curves are triexponential fits described by Eq. 4.1, and the dashed curve is the instrument response function.

we use for C132. Dynamic data normalized by the signal at the longest delay are shown in Figure 4.8 to weigh low-and high-fluence data equally as well.

Using the same fitting process as described for C132, the fits to Eq. 4.1 yield $\tau_f = 0.33 \pm 0.01$ ps, $\tau_{s1} = 2.9 \pm 0.2$ ps, and $\tau_{s2} = 39 \pm 3$ ps. The fit amplitudes A_0, A_f, A_{s1}, and A_{s2} are plotted in Figure 4.9, and the A_f are found to be well described by the same model we used to described C132.

Similarly, we used the same three fitting approaches as we used for C132 to analyze the C168 data. The fitting procedure outlined above without normalization yields $\tau_f =$

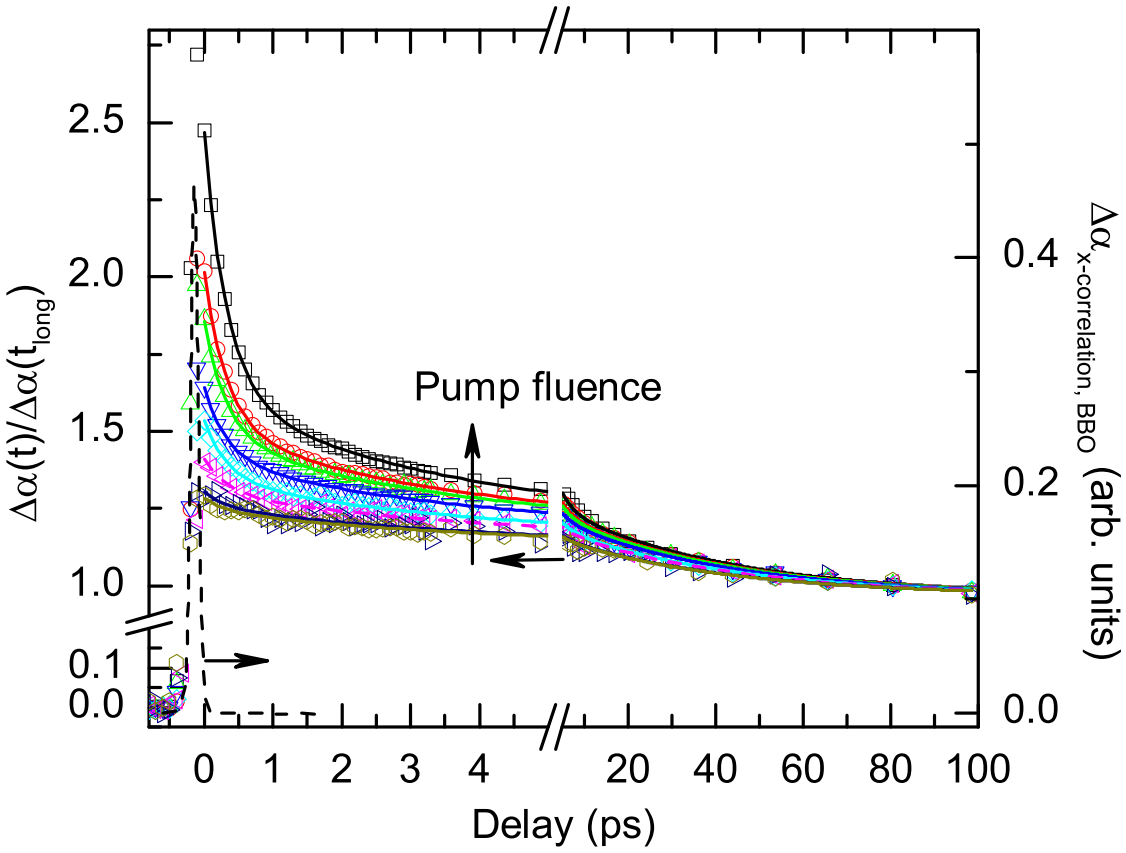

Figure 4.8: $\Delta\alpha(t)/\Delta\alpha(t_{\text{long}})$ versus probe delay for C168 in toluene excited at $\hbar\omega_{\text{pump}} = 1.70$ eV and probed at $\hbar\omega_{\text{probe}} = 2.21$ eV.

0.31(0.01) ps, τ_{s1} = 2.1(0.1) ps, and τ_{s2} = 24.9(0.3) ps. The third procedure yields τ_f = 0.32(0.01) ps, τ_{s1} = 2.3(0.1) ps, and τ_{s2} = 15.6(0.5) ps. In general, τ_{s1} and τ_{s2} from different fitting models do not match well. This difference is caused by the different weights to the high-fluence data in these different approaches. Different fitting procedures yield values of τ_{s1} ranging from 2.1 to 2.9 ps and values of τ_{s2} ranging from 16 to 39 ps. τ_f barely changes, though, because it is predominantly a consequence of the generation of multiple excitons, whereas the dynamics at τ_{s1} and τ_{s2} have contributions from both single- and multiple-photon absorption. The variations in the slow decays may result from the increased excess heat deposited in the GQD lattice following AR in the multiple-exciton regime.

Figure 4.9 shows the excitation-fluence dependence of the parameters A_0, A_f, A_{s1}, and

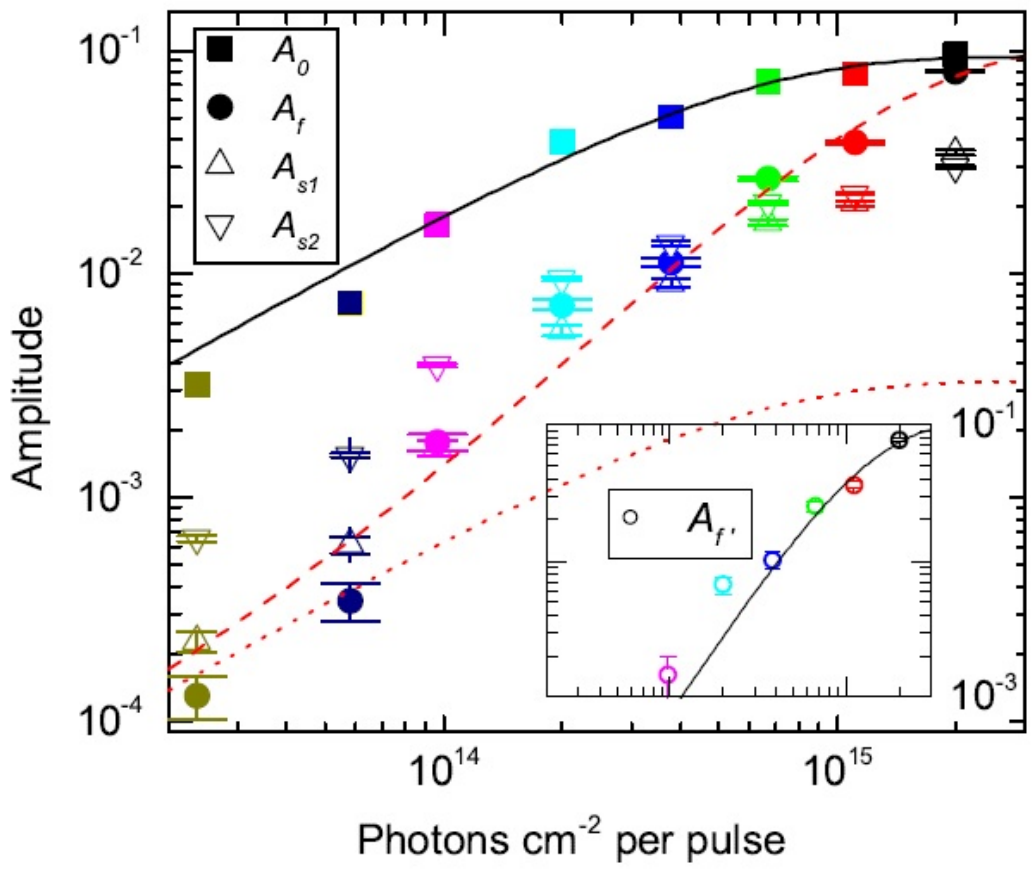

Figure 4.9: Amplitudes A_i from Eq. 4.1 describing the fits of $-\Delta\alpha(\Phi, t)L$ of C168 in Figure 4.7. The inset shows the quantity $A_{f'}$ defined in the text and associated with multiexcitons and uses the horizontal scale of the main figure. Curves show the fits described in the text.

A_{s2} derived from the triexponential fit from Eq. 4.1 to the data of Figure 4.7. The fluence-dependence of A_0 is fit (solid black curve) by the Poisson form described by Eq. 4.2 and corresponds to an effective absorption cross section of $\sigma_0(\hbar\omega = 1.70\,\text{eV}) = (2.1 \pm 0.3) \times 10^{-15}\,\text{cm}^2$. A fit of A_f to the form described by Eq. 4.3 is shown by the dashed red curve and corresponds to $\sigma' = (0.6 \pm 0.15)\sigma_0$. The ratio also matches the expected value of 0.5 as we discussed for C132. The contribution to A_f of the fitting term associated with the amplitude $A_{f,\text{X}}$ in Eq. 4.3 is shown by the red dotted curve, which illustrates that the multiexciton contribution is much greater than the single-exciton contribution at fluences $\Phi \geq 1 \times 10^{14}\,\text{cm}^{-2}$. The inset of Figure 4.9 explicitly shows the multiexciton contribution

to the amplitude of the fast decay by plotting the quantity $A_{f\prime} = A_f - A_{f,\mathrm{X}}\left[1 - P_0(\sigma_0\Phi)\right]$, i.e., subtracting the single-exciton contribution to the fast decay represented from A_f. The solid curve shown in the inset is the contribution of the multiexciton term in the fit of the A_f fluence-dependence.

Besides the TA measurements in the visible spectral range, we also probed the sample in the infrared range as discussed in Chapter 3. This probes the intraband transitions of the GQDs. We excited C168 at 3.1 eV and probed the sample at the induced absorption peak (0.75 eV). Figure 4.10 shows the excitation data of C168 at $\hbar\omega_{\mathrm{pump}} = 3.10$ eV with pump fluences in the multiple- and single-photon absorption regimes respectively. Comparing with the interband data we showed previously, we did not find much difference in the first few ps between multiple- and single-photon absorption. It is unclear why Auger recombination is less pronounced at this energy. Further study is needed to better understand the intraband transitions of the GQDs.

4.2.3 Discussion on Auger recombination of GQDs

The fluence-dependence of A_f (fast decay amplitude) supports the assignment of the superlinear fluence-dependent initial TA response to BXs decaying with an AR lifetime of $\tau_{AR,BX} = \tau_f = 0.3$ ps. In our GQDs, AR generates a hot exciton that rapidly (i.e., faster than τ_f) cools to the lowest-energy exciton state and deposits in the lattice about one band gap of energy. After this, the last stage of electronic and vibronic cooling or solvent orientation proceeds on similar time scales (τ_{s1} and τ_{s2}) as observed at low excitation fluences. The energy of the pump photons in the TA experiments is set to be slightly higher than the band gap of the sample. In the case of absorption of a single photon by a C132

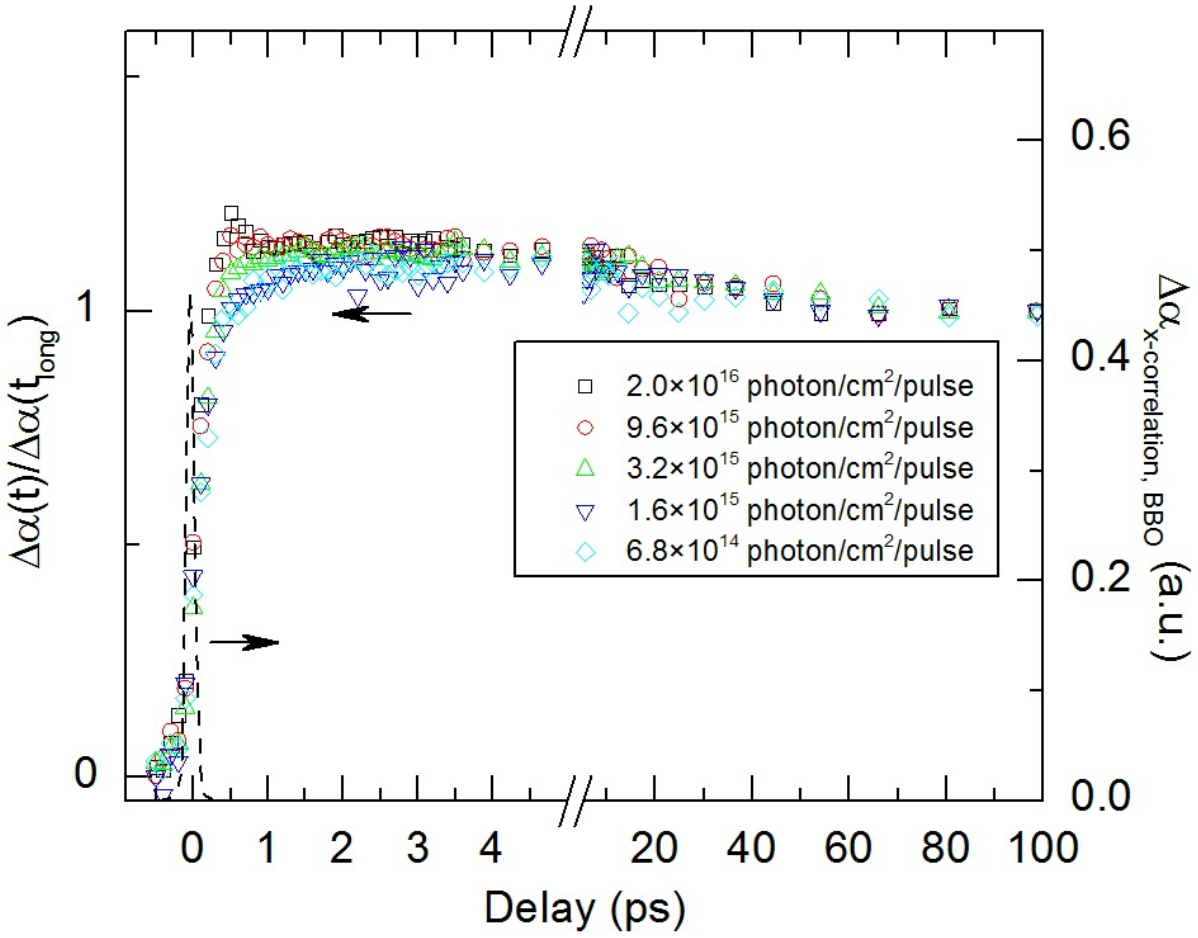

Figure 4.10: $\Delta\alpha(t)/\Delta\alpha(t_{\text{long}})$ versus probe delay for C168 in toluene excited at $\hbar\omega_{\text{pump}} = 3.10$ eV and probed at $\hbar\omega_{\text{probe}} = 0.76\,\text{eV}$.

GQD, only ~ 0.2 eV of excess energy is dissipated during relaxation to the lowest-energy exciton state. AR is an additional source of heating of the carriers, and consequently, the amplitudes A_{s1} and A_{s2} should depend superlinearly on Φ, as we observed from the TA experiment.

The fact that we observed fast decay amplitudes that have superlinear fluence-dependence is not sufficient to assign τ_f to BXs decay by AR. It is possible that two-photon absorption creates a high-energy single exciton instead of a biexciton. τ_f could be the time constant of the cooling process of this high-energy single exciton to the bright exciton peak (570 nm

for C132) or to the lower-energy exciton states. It is also possible that AR occurs on a time scale below the temporal resolution of our measurements and is followed by cooling of a hot single-exciton with the time scale of τ_f. Further analysis of the TA spectrum can rule out these alternatives. If τ_f corresponds to cooling to the bright singlet excitons, the bleach of the main peak should increase with time constant τ_f before decreasing on the time scale for cooling into the lower-energy states (X_1 and X_2 for C132 and C168, respectively). If τ_f was the time scale for cooling from the main peak to X_1 and X_2, then the bleach of the latter should build up on the time scale τ_f, which we did not observe.

Despite the commonly observed reduction of AR lifetimes with decreasing nanoparticle size, further considerations allow us to understand why GQD BX AR lifetimes can be similar to BX AR lifetimes in SWCNTs. AR of directly generated BXs in (9,7) SWCNTs occurs in 0.5 ps [109]. The "universality" of BX AR lifetimes in nanocrystal quantum dots is largely due to relaxation of momentum conservation [86]. A SWCNT retains long-range periodicity in one dimension, but in (6,5) SWCNTs the "diameter" of the single exciton along the axis of the SWCNT is only ~ 2.4 nm [72], which is similar to the spatial size (~ 2.4 nm) of the GQDs studied here. Moreover, the BX length in SWCNTs is predicted to be similar to the length of a single exciton [126]. The small size of the SWCNT biexciton means that substantial amplitude over a large range of momenta. From this perspective, momentum conservation should not be much more restrictive for BX decay in a SWCNT than in GQDs of 2-3 nm (the longest edge length for C132 and C168 is 2.4 nm). Other prominent factors determining the BX AR rate are the strength of the screened Coulomb interaction and the single-exciton density of states (DOS_X) at the energy of the BX. Coulombic interactions may be somewhat stronger in GQDs compared to SWCNTs because of the weaker screening associated with a lattice of more limited extent [127]. With respect to DOS_X, in SWCNTs, the E_{22} transition

is near twice the energy of the E_{11} resonance, but there is not such a general enhancement in the GQD DOS_X near the energy of the lowest-energy BX. More precise assessments of these factors will require detailed theoretical calculations. In particular, the similarity in BX AR times for C132 and C168 is contrary to the usual reduction in AR lifetime with reduction in quantum dot size. This may be because of the differences in the density of final states ($DOS_{X_{hot}}$) in C132 or C168 and/or the symmetries of initial (BX) and final (X_{hot}) states. The latter may be important given the distinct symmetries of C132 and C168 because it impacts the magnitude of the AR transition matrix element between a pair of states [128].

4.3 Conclusion

In summary, we measured BX AR lifetime of ~ 0.3 ps in graphene quantum dots with 132 and 168 carbon atoms, the results of which suggest that the GQDs have the potential to enhance photovoltaic efficiencies through carrier multiplication. Observation of moderately faster BX AR in GQDs suggests that GQDs may demonstrate CM efficiencies comparable to or greater than those of SWCNTs [129, 130]. Electron transfer from ruthenium dyes [131, 132] and PbSe nanocrystal quantum dots [76] to TiO_2 occurs on time scales less than 100 and ~ 10 fs, respectively, and hot-electron injection from C132 covalently linked to the $TiO_2(110)$ surface has been measured to occur with a time constant < 15 fs [133]. This implies that the 0.3 ps BX AR lifetimes measured here do not rule out the extraction of multiple carriers.

Chapter 5

Summary

5.1 General summary

The methods and results of this research establish a foundation for exploring electronic structure in GQDs and other low-dimensional materials. The study of electronic structure in this work has been restricted to GQDs of C132 and C168. Because of the more symmetric form of its lattice, C168 has a less-structured spectrum and transitions that are easier to interpret. In Chapter 3, biexciton binding of C168 is measured optically and calculated theoretically. The binding from our measurement is relatively strong and is comparable with single-wall carbon nanotubes. Chapter 4 reports on measured Auger recombination rates in C132 and C168. The model matches the experimental data quite well. As the Auger process is fast (0.3 ps) in the GQDs, this suggests that the inverse process, namely carrier multiplication, can be efficient. And electron injection from C132 covalently linked to the $TiO_2(110)$ surface has been measured to occur on a timescale of < 15 fs, which is much less than Auger time from our study, fast Auger recombination might not prevent the extraction of multiple carriers from a GQD. Combined with the fact that the absorption spectrum of the GQDs covering most of UV and visible range of solar spectrum, GQDs may be good candidates for sensitizers in solar cells.

5.2 Future work

The completion of this work opens the door to the next set of experiments exploring GQDs. There are still many issues worth further theoretical and experimental study. Based on our analysis, the electron-phonon interaction is important to fully understand the structure and behaviors of the GQDs. The intensity of photoluminescence features is strongly dependent on the excitation wavelength based on Riesen's experiment [11] and Mullen et al [67]. This behavior is strong evidence of the presence of impurity species. Further insights may be possible if we can separate impurities from the main species. Given the fact that the studied GQDs have low PL quantum yield, it is also important to understand the optically allowed and forbidden states in the system. In our study, we focus more on the symmetric GQD C168 as it has fewer distinct transitions which can be better distinguished. The less symmetric GQD, C132, requires more investigation to understand its complicated absorption spectrum and electronic structure. This can also help people better understand how structure and symmetry affect the exciton/biexciton behaviors in such a low-dimensional system.

BIBLIOGRAPHY

BIBLIOGRAPHY

[1] USB2000+ Fiber Optic Spectrometer Installation and Operation Manual, document number 270-00000-000-02-201107, Ocean Optics, http://oceanoptics.com/wp-content/uploads/USB2000-Operating-Instructions1.pdf.

[2] A. H. Castro Neto, N. M. R. Peres, K. S. Novoselov, and a. K. Geim. The electronic properties of graphene. *Reviews of Modern Physics*, 81(1):109–162, Jan 2009.

[3] G. Eda, Y. Lin, C. Mattevi, H. Yamaguchi, H. Chen, I. Chen, C. Chen, and M. Chhowalla. Blue photoluminescence from chemically derived graphene oxide. *Advanced materials*, 22(4):505–9, Jan 2010.

[4] Z. Z. Zhang, K. Chang, and F. M. Peeters. Tuning of energy levels and optical properties of graphene quantum dots. *Physical Review B*, 77(23):235411, Jun 2008.

[5] S. Fujii and T. Enoki. Nanographene and graphene edges: electronic structure and nanofabrication. *Accounts of Chemical Research*, 46(10):2202–2210, Oct 2013.

[6] W. Sheng, M. Korkusinski, A. D. Güçlü, M. Zielinski, P. Potasz, E. S. Kadantsev, O. Voznyy, and P. Hawrylak. Electronic and optical properties of semiconductor and graphene quantum dots. *Frontiers of Physics*, 7(3):328–352, Oct 2011.

[7] P. Gao, K. Ding, Y. Wang, K. Ruan, S. Diao, Q. Zhang, B. Sun, and J. Jie. Crystalline Si/graphene quantum dots heterojunction solar cells. *The Journal of Physical Chemistry C*, 118(10):5164–5171, Mar 2014.

[8] X. Yan, X. Cui, and L. Li. Synthesis of large, stable colloidal graphene quantum dots with tunable size. *Journal of the American Chemical Society*, 132(17):5944–5, May 2010.

[9] W. Shockley and H. J. Queisser. Detailed balance limit of efficiency of p-n junction solar cells. *Journal of Applied Physics*, 32(3):510, 1961.

[10] a. V. Rozhkov and F. Nori. Exact wave functions for an electron on a graphene triangular quantum dot. *Physical Review B*, 81(15):1–13, Apr 2010.

[11] H. Riesen, C. Wiebeler, and S. Schumacher. Optical spectroscopy of graphene quantum dots: the case of C132. *The journal of physical chemistry. A*, 118(28):5189–95, Jul 2014.

[12] M. Kuno. *Introductory Nanoscience: Physical and Chemical Concepts*. 1st edition, 2011.

[13] G. Nair, L. Chang, S. M. Geyer, and M. G. Bawendi. Perspective on the prospects of a carrier multiplication nanocrystal solar cell. *Nano letters*, 11(5):2145–51, May 2011.

[14] C. Sun, F. Figge, I. Ozfidan, M. Korkusinski, X. Yan, Li. Li, P. Hawrylak, and J. A. McGuire. Biexciton binding of dirac fermions confined in colloidal Graphene Quantum Dots. *Nano letters*, 15(8):5472–6, Aug 2015.

[15] I. Ozfidan, M. Korkusinski, a. D. Güçlü, J. a. McGuire, and P. Hawrylak. Microscopic theory of the optical properties of colloidal graphene quantum dots. *Physical Review B*, 89(8):085310, Feb 2014.

[16] P. A. George, J. Strait, J. Dawlaty, S. Shivaraman, M. Chandrashekhar, F. Rana, and M.G. Spencer. Ultrafast optical-pump terahertz-probe spectroscopy of the carrier relaxation and recombination dynamics in epitaxial graphene. *Nano letters*, 8(12):4248–51, Dec 2008.

[17] L. a. Ponomarenko, F. Schedin, M. I. Katsnelson, R. Yang, E. W. Hill, K. S. Novoselov, and a. K. Geim. Chaotic Dirac billiard in graphene quantum dots. *Science*, 320(5874):356–8, Apr 2008.

[18] P. R. Wallace. The band gheory of graphite. *Physical review*, 71(May):622–634, 1947.

[19] T.A. Land, T. Michely, R.J. Behm, J.C. Hemminger, and G. Comsa. STM investigation of single layer graphite structures produced on Pt(111) by hydrocarbon decomposition. *Surface Science*, 264(3):261–270, Mar 1992.

[20] M. Terai, N. Hasegawa, M. Okusawa, S. Otani, and C. Oshima. Electronic states of monolayer micrographite on TiC(111)-faceted and TiC(410) surfaces. *Applied Surface Science*, 130-132:876–882, Jun 1998.

[21] A.M Affoune, B.L.V Prasad, H. Sato, T. Enoki, Y. Kaburagi, and Y. Hishiyama. Experimental evidence of a single nano-graphene. *Chemical Physics Letters*, 348(1-2):17–20, Nov 2001.

[22] K. S. Novoselov, A. K. Geim, S. V. Morozov, D. Jiang, Y. Zhang, S. V. Dubonos, I. V. Grigorieva, and A. A. Firsov. Electric field effect in atomically thin carbon films. *Science*, 306(5696):666–9, Oct 2004.

[23] K. S. Novoselov, D. Jiang, F. Schedin, T. J. Booth, V. V. Khotkevich, S. V. Morozov, and A. K. Geim. Two-dimensional atomic crystals. *Proceedings of the National Academy of Sciences of the United States of America*, 102(30):10451–3, Jul 2005.

[24] J. Wu, H. A. Becerril, Z. Bao, Z. Liu, Y. Chen, and P. Peumans. Organic solar cells with solution-processed graphene transparent electrodes. *Applied Physics Letters*, 92(26):263302, Jul 2008.

[25] X. Wang, L. Zhi, and K. Müllen. Transparent, conductive graphene electrodes for dye-sensitized solar cells. *Nano letters*, 8(1):323–7, Jan 2008.

[26] J. D. Roy-Mayhew, D. J. Bozym, C. Punckt, and I. A. Aksay. Functionalized graphene as a catalytic counter electrode in dye-sensitized solar cells. *ACS nano*, 4(10):6203–11, Oct 2010.

[27] G. Eda, G. Fanchini, and M. Chhowalla. Large-area ultrathin films of reduced graphene oxide as a transparent and flexible electronic material. *Nature nanotechnology*, 3(5):270–4, May 2008.

[28] K. S. Kim, Y. Zhao, H. Jang, S. Y. Lee, J. M. Kim, K. S Kim, J. Ahn, P. Kim, J. Choi, and B. Hong. Large-scale pattern growth of graphene films for stretchable transparent electrodes. *Nature*, 457(7230):706–10, Feb 2009.

[29] X. Li, W. Cai, J. An, S. Kim, J. Nah, D. Yang, R. Piner, A. Velamakanni, I. Jung, E. Tutuc, S.K. Banerjee, L. Colombo, and R. S. Ruoff. Large-area synthesis of high-quality and uniform graphene films on copper foils. *Science*, 324(5932):1312–4, Jun 2009.

[30] K. S. Novoselov, A. K. Geim, S. V. Morozov, D. Jiang, M. I. Katsnelson, I. V. Grigorieva, S. V. Dubonos, and A. A. Firsov. Two-dimensional gas of massless Dirac fermions in graphene. *Nature*, 438(7065):197–200, Nov 2005.

[31] S. Iijima. Helical microtubules of graphitic carbon. *Nature*, 354(6348):56–58, Nov 1991.

[32] S. Iijima and T. Ichihashi. Single-shell carbon nanotubes of 1-nm diameter. *Nature*, 363(6430):603–605, Jun 1993.

[33] T. Guo, P. Nikolaev, A. Thess, D. T. Colbert, and R. E. Smalley. Catalytic growth of single-walled nanotubes by laser vaporization. *Chemical Physics Letters*, 243:49–54, Sep 1995.

[34] S. A. Steiner, T. F. Baumann, B. C. Bayer, R. Blume, M. A. Worsley, W. J. MoberlyChan, E. L. Shaw, R. Schlögl, A. J. Hart, S. Hofmann, and B. L. Wardle. Nanoscale zirconia as a nonmetallic catalyst for graphitization of carbon and growth of single- and multiwall carbon nanotubes. *Journal of the American Chemical Society*, 131(34):12144–54, Sep 2009.

[35] D. S. Bethune, C. H. Klang, M. S. de Vries, G. Gorman, R. Savoy, J. Vazquez, and R. Beyers. Cobalt-catalysed growth of carbon nanotubes with single-atomic-layer walls. *Nature*, 363(6430):605–607, Jun 1993.

[36] K. Nakada, M. Fujita, G. Dresselhaus, and M. S. Dresselhaus. Edge state in graphene ribbons: Nanometer size effect and edge shape dependence. *Physical Review B*, 54(24):17954–17961, Dec 1996.

[37] P. Avouris. Graphene: electronic and photonic properties and devices. *Nano letters*, 10(11):4285–4294, Sep 2010.

[38] V. Barone, O. Hod, and G. E. Scuseria. Electronic structure and stability of semiconducting graphene nanoribbons. *Nano letters*, 6(12):2748–54, Dec 2006.

[39] X. Li, X. Wang, L. Zhang, S. Lee, and H. Dai. Chemically derived, ultrasmooth graphene nanoribbon semiconductors. *Science*, 319(5867):1229–32, Feb 2008.

[40] S. S. Datta, D. R. Strachan, S.M. Khamis, and A. T. C. Johnson. Crystallographic etching of few-layer graphene. *Nano letters*, 8(7):1912–5, Jul 2008.

[41] L. Tapasztó, G. Dobrik, P. Lambin, and L.P. Biró. Tailoring the atomic structure of graphene nanoribbons by scanning tunnelling microscope lithography. *Nature nanotechnology*, 3(7):397–401, Jul 2008.

[42] L. Jiao, L. Zhang, X. Wang, G. Diankov, and H. Dai. Narrow graphene nanoribbons from carbon nanotubes. *Nature*, 458(7240):877–80, Apr 2009.

[43] J. Cai, P. Ruffieux, R. Jaafar, M. Bieri, T. Braun, S. Blankenburg, M. Muoth, A. P. Seitsonen, M. Saleh, Xinliang Feng, Klaus Müllen, and Roman Fasel. Atomically precise bottom-up fabrication of graphene nanoribbons. *Nature*, 466(7305):470–3, Jul 2010.

[44] H. Zhang, H. Lin, K. Sun, L. Chen, Y. Zagranyarski, N. Aghdassi, S. Duhm, Q. Li, D. Zhong, Y. Li, K. Müllen, H. Fuchs, and L. Chi. On-surface synthesis of rylene-type graphene nanoribbons. *Journal of the American Chemical Society*, 137(12):4022–5, Apr 2015.

[45] Y. Chen, D. G. de Oteyza, Z. Pedramrazi, C. Chen, F. R. Fischer, and M. F. Crommie. Tuning the band gap of graphene nanoribbons synthesized from molecular precursors. *ACS nano*, 7(7):6123–8, Jul 2013.

[46] A. Narita, X. Feng, Y. Hernandez, S. A. Jensen, M. Bonn, H. Yang, I. A. Verzhbitskiy, C. Casiraghi, M. Hansen, A. Koch, G. Fytas, O. Ivasenko, B. Li, K. Mali, T. Balandina, S. Mahesh, S. De Feyter, and K. Müllen. Synthesis of structurally well-defined and liquid-phase-processable graphene nanoribbons. *Nature Chemistry*, 6(2):126–132, Dec 2013.

[47] A. Narita, I. A. Verzhbitskiy, W. Frederickx, K.S. Mali, S. A. Jensen, M.R. Hansen, M. Bonn, S. De Feyter, C. Casiraghi, X. Feng, and K. Müllen. Bottom-up synthesis of liquid-phase-processable graphene nanoribbons with near-infrared absorption. *ACS nano*, 8(11):11622–30, Nov 2014.

[48] J. Shen, Y. Zhu, C. Chen, X. Yang, and C. Li. Facile preparation and upconversion luminescence of graphene quantum dots. *Chemical communications*, 47(9):2580–2, Mar 2011.

[49] J. Peng, W. Gao, B. K. Gupta, Z. Liu, R. Romero-Aburto, L. Ge, L. Song, L. B. Alemany, X. Zhan, G. Gao, S. A. Vithayathil, B. A. Kaipparettu, A.A. Marti, T. Hayashi, J. Zhu, and P.M Ajayan. Graphene quantum dots derived from carbon fibers. *Nano letters*, 12(2):844–9, Feb 2012.

[50] Y. Li, Y. Hu, Y. Zhao, G. Shi, L. Deng, Y. Hou, and L. Qu. An electrochemical avenue to green-luminescent graphene quantum dots as potential electron-acceptors for photovoltaics. *Advanced materials*, 23(6):776–80, Feb 2011.

[51] X. Yan, X. Cui, B. Li, and L. Li. Large, solution-processable graphene quantum dots as light absorbers for photovoltaics. *Nano letters*, 10(5):1869–73, May 2010.

[52] R. Liu, D. Wu, X. Feng, and K. Müllen. Bottom-up fabrication of photoluminescent graphene quantum dots with uniform morphology. *Journal of the American Chemical Society*, 133(39):15221–3, Oct 2011.

[53] X. Zhou, Y. Zhang, C. Wang, X. Wu, Y. Yang, B. Zheng, H. Wu, S. Guo, and J. Zhang. Photo-Fenton reaction of graphene oxide: a new strategy to prepare graphene quantum dots for DNA cleavage. *ACS nano*, 6(8):6592–9, Aug 2012.

[54] L. Przybilla, J. Brand, K. Yoshimura, H. J. Räder, and K. Müllen. MALDI-TOF mass spectrometry of insoluble giant polycyclic aromatic hydrocarbons by a new method of sample sreparation. *Analytical Chemistry*, 72(19):4591–4597, Oct 2000.

[55] A. M. Smith and S. Nie. Semiconductor nanocrystals: structure, properties, and band gap engineering. *Accounts of Chemical Research*, 43(2):190–200, Feb 2010.

[56] J. Robertson and E. P. OReilly. Electronic and atomic structure of amorphous carbon. *Physical Review B*, 35(6):2946–2957, Feb 1987.

[57] W. L. Wang, S. Meng, and E. Kaxiras. Graphene nanoFlakes with large spin. *Nano letters*, 8(1):241–5, Jan 2008.

[58] W. Wang, O. Yazyev, S. Meng, and E. Kaxiras. Topological frustration in graphene nanoflakes: magnetic order and spin logic devices. *Physical Review Letters*, 102(15):157201, Apr 2009.

[59] A. Güçlü, P. Potasz, and P. Hawrylak. Excitonic absorption in gate-controlled graphene quantum dots. *Physical Review B*, 82(15):155445, Oct 2010.

[60] S. Chen, J. Liu, M. Chen, X. Chen, and J. Wang. Unusual emission transformation of graphene quantum dots induced by self-assembled aggregation. *Chemical communications*, 48(61):7637–9, Aug 2012.

[61] M. Kastler, W. Pisula, D. Wasserfallen, T. Pakula, and K. Müllen. Influence of alkyl substituents on the solution- and surface-organization of hexa-peri-hexabenzocoronenes. *Journal of the American Chemical Society*, 127(12):4286–96, Mar 2005.

[62] G. Xing, N. Mathews, S. Sun, S. S. Lim, Y. M. Lam, M. Grätzel, S. Mhaisalkar, and T. C. Sum. Long-range balanced electron- and hole-transport lengths in organic-inorganic CH3NH3PbI3. *Science*, 342(6156):344–7, Oct 2013.

[63] Z. Zhu, J. Ma, Z. Wang, C. Mu, Z. Fan, L. Du, Y. Bai, L. Fan, H. Yan, D. L. Phillips, and S. Yang. Efficiency enhancement of perovskite solar cells through fast electron extraction: the role of graphene quantum dots. *Journal of the American Chemical Society*, 136(10):3760–3, Mar 2014.

[64] J. Wu, W. Pisula, and K. Müllen. Graphenes as potential material for electronics. *Chemical reviews*, 107(3):718–47, Mar 2007.

[65] S. Schumacher. Photophysics of graphene quantum dots: Insights from electronic structure calculations. *Physical Review B*, 83(8):1–4, Feb 2011.

[66] M. L. Mueller, X. Yan, J. a. McGuire, and L. Li. Triplet States and electronic relaxation in photoexcited graphene quantum dots. *Nano letters*, 10(7):2679–82, Jul 2010.

[67] M. L. Mueller, X. Yan, B. Dragnea, and L. Li. Slow hot-carrier relaxation in colloidal graphene quantum dots. *Nano letters*, 11(1):56–60, Jan 2011.

[68] J. Frenkel. On the transformation of light into heat in solids. I. *Physical Review*, 37(1):17–44, Jan 1931.

[69] A. D. Yoffe. Low-dimensional systems: Quantum size effects and electronic properties of semiconductor microcrystallites (zero-dimensional systems) and some quasi-two-dimensional systems. *Advances in Physics*, 51(2):799–890, Mar 2002.

[70] M. A. Mahmoud, M. Chamanzar, A. Adibi, and M. A. El-Sayed. Effect of the dielectric constant of the surrounding medium and the substrate on the surface plasmon resonance spectrum and sensitivity factors of highly symmetric systems: silver nanocubes. *Journal of the American Chemical Society*, 134(14):6434–42, Apr 2012.

[71] D. C. Elias, R. V. Gorbachev, A. S. Mayorov, S. V. Morozov, A. A. Zhukov, P. Blake, L. A. Ponomarenko, I. V. Grigorieva, K. S. Novoselov, F. Guinea, and A. K. Geim. Dirac cones reshaped by interaction effects in suspended graphene. *Nature Physics*, 7(9):701–704, Jul 2011.

[72] F. Wang, G. Dukovic, L. E. . Brus, and T. Heinz. The optical resonances in carbon nanotubes arise from excitons. *Science*, 787(May):838–842, May 2005.

[73] D. Sarkar, H. P. van der Meulen, J. M. Calleja, J. M. Becker, R. J. Haug, and K. Pierz. Exciton fine structure and biexciton binding energy in single self-assembled InAsAlAs quantum dots. *Journal of Applied Physics*, 100(2):023109, Jul 2006.

[74] M. S Dresselhaus, G. Dresselhaus, R. Saito, and A. Jorio. Exciton photophysics of carbon nanotubes. *Annual review of physical chemistry*, 58:719–47, Jan 2007.

[75] V. I. Klimov. Quantization of multiparticle Auger rates in semiconductor quantum dots. *Science*, 287(5455):1011–1013, Feb 2000.

[76] Y. Yang, W. Rodríguez-Córdoba, X. Xiang, and Ti. Lian. Strong electronic coupling and ultrafast electron transfer between PbS quantum dots and TiO2 nanocrystalline films. *Nano letters*, 12(1):303–9, Jan 2012.

[77] AndoTsuneya. Excitons in carbon nanotubes. *Journal of the Physical Society of Japan*, 66(4):1066–1073, Nov 1997.

[78] C.D. Spataru, S. Ismail-Beigi, L.X. Benedict, and S.G. Louie. Quasiparticle energies, excitonic effects and optical absorption spectra of small-diameter single-walled carbon nanotubes. *Applied Physics A: Materials Science & Processing*, 78(8):1129–1136, May 2004.

[79] C. Spataru, S. Ismail-Beigi, L. Benedict, and S. Louie. Excitonic effects and optical spectra of single-walled carbon nanotubes. *Physical Review Letters*, 92(7):077402, Feb 2004.

[80] J. Maultzsch, R. Pomraenke, S. Reich, E. Chang, D. Prezzi, a. Ruini, E. Molinari, M. Strano, C. Thomsen, and C. Lienau. Exciton binding energies in carbon nanotubes from two-photon photoluminescence. *Physical Review B*, 72(24):1–4, Dec 2005.

[81] M. E. Reimer, D. Dalacu, P. J. Poole, and R. L. Williams. Biexciton binding energy control in site-selected quantum dots. *Journal of Physics: Conference Series*, 210(1):012019, Feb 2010.

[82] D. Simeonov, A. Dussaigne, R. Butté, and N. Grandjean. Complex behavior of biexcitons in GaN quantum dots due to a giant built-in polarization field. *Physical Review B*, 77(7):075306, Feb 2008.

[83] R. Schaller and V. I. Klimov. High efficiency carrier multiplication in PbSe nanocrystals: implications for solar energy conversion. *Physical Review Letters*, 92(18):1–4, May 2004.

[84] V. I. Klimov. Detailed-balance power conversion limits of nanocrystal-quantum-dot solar cells in the presence of carrier multiplication. *Applied Physics Letters*, 89(12):123118, 2006.

[85] F. Wang, G. Dukovic, E. Knoesel, L. Brus, and T. Heinz. Observation of rapid Auger recombination in optically excited semiconducting carbon nanotubes. *Physical Review B*, 70(24):1–4, Dec 2004.

[86] I. Robel, R. Gresback, U. Kortshagen, R. Schaller, and V. I. Klimov. Universal size-dependent trend in Auger recombination in direct-gap and indirect-gap semiconductor nanocrystals. *Physical Review Letters*, 102(17):177404, May 2009.

[87] C. Sevik and C. Bulutay. Auger recombination and carrier multiplication in embedded silicon and germanium nanocrystals. *Physical Review B*, 77(12):125414, Mar 2008.

[88] L. A. Padilha, J.T. Stewart, R. L. Sandberg, W. Bae, W. Koh, J. M. Pietryga, and V. I. Klimov. Aspect ratio dependence of auger recombination and carrier multiplication in PbSe nanorods. *Nano letters*, 13(3):1092–9, Mar 2013.

[89] M. A. Ratner. Chemical applications of ultrafast spectroscopy. By Graham R. Fleming, Oxford, New york, 1986. *International Journal of Quantum Chemistry*, 31(6):989–989, Jun 1987.

[90] B. Valeur and M. N. Berberan-Santos. *Molecular fluorescence: principles and applications*. John Wiley & Sons, 2012.

[91] H. Staerk, A. Wiessner, and W. Kühnle. Spectro-streak picosecond studies of intramolecular charge-transfer fluorescence. *Journal of fluorescence*, 4(1):87–90, Mar 1994.

[92] B. Gobets, I. H. M. van Stokkum, F. van Mourik, J. P. Dekker, and R. van Grondelle. Excitation wavelength dependence of the fluorescence kinetics in photosystem I particles from synechocystis PCC 6803 and synechococcus elongatus. *Biophysical journal*, 85(6):3883–98, Dec 2003.

[93] C. V. Zint, W. Uhring, M. Torregrossa, B. Cunin, and P. Poulet. Streak camera: A multidetector for diffuse tptical tomography. *Applied Optics*, 42(16):3313, Jun 2003.

[94] A. Stolow, A. E. Bragg, and D.M. Neumark. Femtosecond time-resolved photoelectron spectroscopy. *Chemical reviews*, 104(4):1719–57, Apr 2004.

[95] R. A. Kaindl, M. Wurm, K. Reimann, P. Hamm, A. M. Weiner, and M. Woerner. Generation, shaping, and characterization of intense femtosecond pulses tunable from 3 to 20 μm. *Journal of the Optical Society of America B*, 17(12):2086, Dec 2000.

[96] New External Triggering Options Instructions for Spectrometers with Firmware Version 3.0 and Above, Ocean Optics, http://www.oceanoptics.com/technical/External-Triggering2.pdf.

[97] Labview project, http://goo.gl/e3NX5u.

[98] J. Shah. Ultrafast luminescence spectroscopy using sum frequency generation. *IEEE Journal of Quantum Electronics*, 24(2):276–288, 1988.

[99] A. Güçlü, P. Potasz, M. Korkusinski, and P. Hawrylak. Graphene quantum dots, 2014.

[100] Y. Z. Hu, M. Lindberg, and S. W. Koch. Theory of optically excited intrinsic semiconductor quantum dots. *Physical Review B*, 42(3):1713–1723, Jul 1990.

[101] K. I. Kang, A. D. Kepner, S. V. Gaponenko, S. W. Koch, Y. Z. Hu, and N. Peyghambarian. Confinement-enhanced biexciton binding energy in semiconductor quantum dots. *Physical Review B*, 48(20):15449–15452, Nov 1993.

[102] D. Kleinman. Binding energy of biexcitons and bound excitons in quantum wells. *Physical Review B*, 28(2):871–879, Jul 1983.

[103] D. Birkedal, J. Singh, V. Lyssenko, J. Erland, and J. Hvam. Binding of quasi-two-dimensional biexcitons. *Physical Review Letters*, 76(4):672–675, Jan 1996.

[104] R. Miller, D. Kleinman, W. Tsang, and A. Gossard. Observation of the excited level of excitons in GaAs quantum wells. *Physical Review B*, 24(2):1134–1136, Jul 1981.

[105] G. pt Hooft, W. van der Poel, L. Molenkamp, and C. Foxon. Giant oscillator strength of free excitons in GaAs. *Physical Review B*, 35(15):8281–8284, May 1987.

[106] Y. Hu, S. Koch, M. Lindberg, N. Peyghambarian, E. Pollock, and Farid Abraham. Biexcitons in semiconductor quantum dots. *Physical Review Letters*, 64(15):1805–1807, Apr 1990.

[107] K. Brunner, G. Abstreiter, G. Böhm, G. Tränkle, and G. Weimann. Sharp-line photoluminescence and two-photon absorption of zero-dimensional biexcitons in a GaAs/AlGaAs structure. *Physical Review Letters*, 73(8):1138–1141, Aug 1994.

[108] A. Jorio, R. Saito, J. Hafner, C. Lieber, M. Hunter, T. McClure, G. Dresselhaus, and M. Dresselhaus. Structural (n, m) determination of isolated single-wall carbon nanotubes by resonant raman scattering. *Physical Review Letters*, 86(6):1118–1121, Feb 2001.

[109] L. Colombier, J. Selles, E. Rousseau, J. S. Lauret, F. Vialla, C. Voisin, and G. Cassabois. Detection of a biexciton in semiconducting carbon nanotubes using nonlinear optical spectroscopy. *Physical Review Letters*, 109(19):197402, Nov 2012.

[110] A. E. MARTIN. Difference and derivative spectra. *Nature*, 180(4579):231–233, Aug 1957.

[111] C. Sun, F. Figge, J. A. McGuire, Q. Li, and L. Li. Biexciton Auger recombination in colloidal graphene quantum dots. *Physical Review Letters*, 113(10):107401, Sep 2014.

[112] R. D. Schaller, J. M. Pietryga, S. V. Goupalov, M. A. Petruska, S. A. Ivanov, and V. I. Klimov. Breaking the phonon bottleneck in semiconductor nanocrystals via multiphonon emission induced by intrinsic nonadiabatic interactions. *Physical Review Letters*, 95(19):196401, Oct 2005.

[113] J. M. Harbold, H. Du, T. D. Krauss, K. Cho, C. B. Murray, and F. W. Wise. Time-resolved intraband relaxation of strongly confined electrons and holes in colloidal PbSe nanocrystals. *Physical Review B*, 72(19):195312, Nov 2005.

[114] R. R. Cooney, S. L. Sewall, K. E. H. Anderson, E. A. Dias, and P. Kambhampati. Breaking the phonon bottleneck for holes in semiconductor quantum dots. *Physical Review Letters*, 98(17):177403, Apr 2007.

[115] D. S. Boudreaux, F. Williams, and A. J. Nozik. Hot carrier injection at semiconductor-electrolyte junctions. *Journal of Applied Physics*, 51(4):2158, Jul 1980.

[116] O. V. Prezhdo. Multiple excitons and the electronphonon bottleneck in semiconductor quantum dots: An ab initio perspective. *Chemical Physics Letters*, 460(1-3):1–9, Jul 2008.

[117] J. M. Dawlaty, S. Shivaraman, M. Chandrashekhar, F. Rana, and M. G. Spencer. Measurement of ultrafast carrier dynamics in epitaxial graphene. *Applied Physics Letters*, 92(4):042116, Jan 2008.

[118] T. Winzer, A. Knorr, and E. Malic. Carrier multiplication in graphene. *Nano letters*, 10(12):4839–43, Dec 2010.

[119] M. Breusing, S. Kuehn, T. Winzer, E. Malić, F. Milde, N. Severin, J. P. Rabe, C. Ropers, A. Knorr, and T. Elsaesser. Ultrafast nonequilibrium carrier dynamics in a single graphene layer. *Physical Review B*, 83(15):153410, Apr 2011.

[120] S. Winnerl, M. Orlita, P. Plochocka, P. Kossacki, M. Potemski, T. Winzer, E. Malic, A. Knorr, M. Sprinkle, C. Berger, W. A. de Heer, H. Schneider, and M. Helm. Carrier relaxation in epitaxial graphene photoexcited near the dirac point. *Physical Review Letters*, 107(23):237401, Nov 2011.

[121] M. Hybertsen. Absorption and emission of light in nanoscale silicon structures. *Physical Review Letters*, 72(10):1514–1517, Mar 1994.

[122] H. Htoon, J. Hollingsworth, R. Dickerson, and V. Klimov. Effect of zero- to one-dimensional transformation on multiparticle Auger recombination in semiconductor quantum rods. *Physical Review Letters*, 91(22):227401, Nov 2003.

[123] A. Haug. Band-to-band Auger recombination in semiconductors. *Journal of Physics and Chemistry of Solids*, 49(6):599–605, Jan 1988.

[124] L. Huang and T. Krauss. Quantized bimolecular auger recombination of excitons in single-walled carbon nanotubes. *Physical Review Letters*, 96(5):057407, Feb 2006.

[125] K. F. Mak, J. Shan, and T. F. Heinz. Seeing many-body effects in single- and few-layer graphene: observation of two-dimensional saddle-point excitons. *Physical Review Letters*, 106(4):046401, Jan 2011.

[126] I. V. Bondarev. Asymptotic exchange coupling of quasi-one-dimensional excitons in carbon nanotubes. *Physical Review B*, 83(15):153409, Apr 2011.

[127] L. Brus. Commentary: Carbon nanotubes, CdSe nanocrystals, and electron-electron interaction. *Nano letters*, 10(2):363–5, Feb 2010.

[128] G. Kavoulakis and G. Baym. Auger decay of degenerate and Bose-condensed excitons in Cu2O. *Physical Review B*, 54(23):16625–16636, Dec 1996.

[129] N. M. Gabor, Z. Zhong, K. Bosnick, J. Park, and P. L. McEuen. Extremely efficient multiple electron-hole pair generation in carbon nanotube photodiodes. *Science*, 325(5946):1367–71, Sep 2009.

[130] S. Wang, M. Khafizov, X. Tu, M. Zheng, and T. D. Krauss. Multiple exciton generation in single-walled carbon nanotubes. *Nano letters*, 10(7):2381–6, Jul 2010.

[131] Y. Tachibana, J. E. Moser, M. Grätzel, D. R. Klug, and J. R. Durrant. Subpicosecond interfacial charge separation in dye-sensitized nanocrystalline titanium dioxide films. *The Journal of Physical Chemistry*, 100(51):20056–20062, Jan 1996.

[132] J. B. Asbury, E. Hao, Y. Wang, H. N. Ghosh, and T. Lian. Ultrafast electron transfer dynamics from molecular adsorbates to semiconductor nanocrystalline thin films. *The Journal of Physical Chemistry B*, 105(20):4545–4557, May 2001.

[133] K. J. Williams, C. A. Nelson, X. Yan, L. Li, and X. Zhu. Hot electron injection from graphene quantum dots to TiO. *ACS nano*, 7(2):1388–94, Feb 2013.